School of Earth and Planetary Science

An Electron Backscatter Diffraction Study of Archean Impact Spherules from the Pilbara Craton, Western Australia

Ching Ee Lim
0000-0002-6951-4873

This thesis is presented for the Degree of
Master of Research (Earth and Planetary Sciences)
of
Curtin University

June 2022

Declaration

This postgraduate research project was conducted with materials provided by Rio Tinto Exploration staff members, to study impact spherule characteristics in order to provide new insight on the spherule formation processes and their respective origins from a vapor plume. The research materials were obtained from a section of drill core DD15TPSR0001 extracted from the Dales Gorge member at Mount Tom Price, and from a rock specimen from an exposed outcrop of the Bee Gorge member at Munjina Gorge.

The SEM analyses on the impact spherules were directed and conducted with the assistance of the principal supervisor, Dr. Aaron Cavosie. The investigations were largely conducted in the Microscopy and Microanalysis Facility, John de Laeter Centre, Curtin University, with the selected instruments including the Tescan Mira3 and Tescan Clara scanning electron microscopes. All EBSD overnight maps were conducted under the guidance of Dr. Aaron Cavosie.

I declare that this thesis has been composed solely by myself under the supervision of Dr. Aaron Cavosie and Associate Professor Nick Timms, and that it has not been submitted, in whole or in part, in any previous application for professional qualifications. This thesis contains no material which has been accepted for the award of any other degree or diploma in any university. Except where mentioned otherwise by reference or acknowledgment, this thesis contains no material that has been previously published by any other person to the best of my knowledge and belief.

Acknowledgements

I would like to take the opportunity to express my deepest gratitude to my principal supervisor, Dr. Aaron Cavosie, not only for the decisive role in EBSD mapping operations and interpretations, but also his critical advice and patience throughout the duration in this postgraduate research project. I would like to also thank my co-supervisor, Associate Professor Nick Timms, for his scientific perspectives about the research project, which provided me with numerous constructive suggestions. The completion of my dissertation would not have been possible without their guidance and unparalleled support, with the depth of knowledge to enhance the entire research experience.

I would like to acknowledge Dr. Mehrooz Aspandiar, my supervisor in my Honours research project, and also the Rio Tinto Exploration Belmont (RTX) staff members, especially Andrew Faragher, Hilke Dalstra, and Catherine Breheny. I would like to thank RTX for providing us the research materials, including the two impact spherule suites from the Dales Gorge and Bee Gorge members. They also gave us permission to view the core, and the use of sample coordinates for research purposes. This postgraduate research would not been possible without their professional assistance, as this is an expanded study based on my Honours project on Southern Ridge mineralisation.

It was a great experience to be involved with the impact spherule analysis using the various SEM instruments in the Microscopy and Microanalysis Facility at the John de Laeter Centre (MMF-JDLC) of Curtin University. Both the Tescan Mira3 and Tescan Clara instruments provided invaluable data on the mineralogy and microstructure of the selected feldspathic spherules. I would also like to acknowledge the Space Science and Technology Centre (SSTC) members that kindly approached and provided suggestions during the milestone review process for ways to improve my research. I would like to also give a special thanks to my caring family members throughout the research timeframe.

Acknowledgement of Country

We acknowledge that Curtin University works across hundreds of traditional lands and custodial groups in Australia, and with First Nations people around the globe. We wish to pay our deepest respects to their ancestors and members of their communities, past, present, and to their emerging leaders. Our passion and commitment to work with all Australians and peoples from across the world, including our First Nations peoples are at the core of the work we do, reflective of our institutions' values and commitment to our role as leaders in the Reconciliation space in Australia.

Abstract

This thesis describes a systematic study of minerals in feldspathic impact spherules from the Dales Gorge and Bee Gorge spherule layers in the Hamersley Basin of the Pilbara Craton in Western Australia. The overarching goals are to advance interpretations on Archean impact spherule formation processes. The research involves the characterisation of feldspathic spherules from the two impact horizons to propose a vapor plume model to identify where various types of feldspathic spherules may have formed. This includes comparison of representative optical photomicrographs with respective electron backscatter diffraction (EBSD) maps of the same spherules.

Both spherule deposits occur near the Archean-Proterozoic boundary. The 2490 Ma Dales Gorge spherule sample is from a depth of 611 m within a recent (2015) Rio Tinto diamond core (DD15TPSR0001) near Mount Tom Price that has not previously been described. The Dales Gorge spherule layer is hosted by stilpnomelane and siderite-dominated shale associated with banded iron deposits of the Brockman Iron Formation. The 2540 Ma Bee Gorge spherule sample is from a surface outcrop near Munjina Gorge, Karijini. It occurs in a reworked turbidite in the Bee Gorge member within the Wittenoom Formation, and is dominated by dolomite and quartz. EBSD mapping of feldspathic spherules from both layers reveals that alkali feldspar is the dominant mineral. Accessory minerals (ilmenite, apatite) and diagenetic minerals (stilpnomelane, carbonates, alkali feldspar, quartz) are variably present in the layers.

The spherules now only contain alkali feldspar, which is interpreted to be a pseudomorphic replacement phase after plagioclase, because they preserve a range of delicate primary textures interpreted to have formed during spherule formation. Growth textures of feldspar within the feldspathic spherules include both radial and random patterns; these differences provide a means to classify the spherules into different categories according to feldspar crystal characteristics. Radial-type spherules typically feature fan-like radial feldspar crystallites that nucleated on spherule margins and grew inward. Nucleation of radial fans along spherule margins is, in some cases, attributed to impinging dust in the vapor plume, which forms a thin coating around some spherule margins. Radial-type spherules also preserve a range of spherulitic textures indicative of rapid growth and/or variable cooling rates, including spherical, bowtie, and fan-like microstructures. Some radial-type spherules preserve cores of altered glass that are interpreted to have quenched rapidly, and so did not fully crystallise. Random-type spherules lack radial fans and typically feature feldspars with prismatic to tabular

crystal habits, which are interpreted to result from slower cooling rates in a relatively hotter environment, as compared to radial-type spherules.

Dales Gorge spherules contain ilmenite inclusions/intergrowths with three different occurrences: linear ilmenite arrays within spherule interiors, ilmenite grains lining spherule margins, and disseminated ilmenite grains in spherule interiors. The linear ilmenite arrays are here interpreted as a potential primary texture, possibly resulting from exsolution from a host mineral that is no longer present. The other ilmenite occurrences (disseminated, marginal linings) are also interpreted as primary features, rather than a result of post-depositional/diagenetic processes. Bee Gorge feldspathic spherules do not contain ilmenite, but do have sub-micrometre sized apatite inclusions within alkali feldspar, which may have formed during pseudomorphic replacement of plagioclase during diagenesis.

The EBSD results allowed the construction of a simple vapor plume model. The model is based on assumptions for formation of each proposed feldspathic spherule type within a hypothetical thermal gradient, that varies according to the proximity from the impact zone. Quench features and relative degree of supercooling of the feldspathic spherules are also considered in the vapor plume model. A total of five spherule types are represented in the proposed model, each with distinctive alkali feldspar textures: type A, random-type prismatic; type B, random-type with equant to prismatic crystallites; type C, mixture of random and radial-types; type D, radial-type with dust rims; type E, radial-type with quenched glass cores.

Table of Contents

Chapter 1 Introduction of Research Project

1.1 Background of the Study

There is increased interest in interpretations and revision of impact structure formation, as the preservation of impact evidence represents the key to reconstruct Earth's evolutionary history associated with meteoroid impact events (e.g., Glass and Simonson, 2013). Evidence of impact processes ranges from large-scale craters, such as the Chicxulub crater in Mexico (Riller et al., 2018), to impact spherules which are usually millimetre-sized, and preserved within strata across continents and ocean basins.

The focus of this research project is impact spherules, which are also known as distal impact ejecta. Glass and Simonson (2013) note that discriminating impact spherules as either microtektites or microkrystites, according to their respective characteristics, may benefit in determining their origin, although both can occur and form in a single impact event. Distal impact ejecta is produced by the collision of large meteoroid bodies with Earth's surface, resulting in formation of either (1) microtektites, which are crystal-free glass spherules formed in flight via ballistic ejection of impact melt from the impacted region (Glass, 1990), or (2) microkrystites, which form as condensates of ejected silica vapor in clouds/plumes, which contain primary crystallites formed within the melt droplet (Glikson and Vickers, 2010; Glass and Simonson, 2013). Distal ejecta are formed as products of shock metamorphism-deformation via hypervelocity impact, and the resulting vaporisation and melting of Earth's crust (Glikson, 2005; Sweeney and Simonson, 2008). Impact spherules are generally grouped into three categories according to their shapes: splash forms (e.g., spheres, dumbbells, teardrops), ablated forms (associated with secondary melting of splash forms), and Muong-Nong forms (large and blocky-layered textured) (Glass, 1990; Sweeney and Simonson, 2008; Glass and Simonson, 2013). Spherules can aggregate together, crystallise, and even break apart during flight (Sweeney and Simonson, 2008). Reviews of ejecta spherule occurrences within the Hamersley Basin have emphasised the textural and mineralogical properties of spherules, and have suggested possible models of their deposition history and respective age constraints for the associated impact events (e.g., Sweeney and Simonson, 2008; Glass and Simonson, 2013; Krull-Davatzes et al., 2015).

1.2 Geological Context

The two investigated impact spherule horizons, Dales Gorge and Bee Gorge spherule layers (DGSL and BGSL), occur in the Hamersley Group, which is part of the Pilbara Craton (Fig. 1.1, 1.2). The Pilbara Craton is located in the northwestern part of Western Australia, and is one of the oldest cratons on Earth (Fig. 1.1A). It is composed of several components: Archean granitoid-greenstone terranes, volcano-sedimentary successions which include the Pilbara Supergroup, De Grey Supergroup, Mount Bruce Supergroup; and other intrusive supersuites (Fig. 1.3, 1.4) (Petersson et al., 2020). A total of five distal impact spherule layers have been identified near the Archean-Proterozoic boundary in the Pilbara Craton, including the two studied spherule layers, DGSL and BGSL (Fig. 1.3). The other recognised spherule units include the Jeerinah spherule layer (JSL), Carawine spherule layer (CSL), Paraburdoo spherule layer (PSL) (Fig. 1.3). They are principally preserved in a basin, within the upper Fortescue Group and Hamersley Group of Mount Bruce Supergroup (Angerer and Hagemann, 2010). Note that both CSL and JSL likely formed in the same impact event (Simonson et al., 2009; Glass and Simonson, 2013), given the similar lithostratigraphic positions and age constraints (Fig 1.3).

The DGSL occurs in the Dales Gorge member of the Brockman Iron Formation. The BGSL occurs in the Bee Gorge member of the Wittenoom Formation. The early Precambrian Hamersley Group is about 2.5 km thick and predominantly consists of siliciclastic successions such as shale, chert, siltstone, and dolomite units, followed by felsic to mafic intrusions associated with stratabound banded iron deposits (Trendall and Blockley, 1970; Simonson et al., 1993; Thorne et al., 2008) (Fig. 1.4). The base of this group is the Marra Mamba Formation, which overlies the uppermost Fortescue Group member of the Jeerinah Formation, with an unconformity that indicates a hiatus in deposition (Webb et al., 2003; Clout, 2005). The main strata that comprise the Hamersley Group are listed in ascending order: Marra Mamba-Wittenoom Formation, Mount Sylvia Formation, Mount McRae Shale, Brockman Iron Formation, Weeli Formation, Woongarra Rhyolite and Boolgeeda Iron Formation (Thorne, 2015). The Brockman Iron Formation is formed of interbedded BIF and shale units with other siliceous sediments such as chert, mudstone and siltstone (Taylor et al., 2001; Lascelles, 2006). The members in this formation are the Dales Gorge Member, Whaleback Shale Member, the Joffre Member and the Yandicoogina Shale Member (Thorne, 2015).

1.3 Aims and Objectives

This project is an expanded continuation of a BSc Honours research investigation completed in 2020. The Honours project included: (1) a study of the stratigraphic significance of the occurrence of reddening features within banded iron formations (BIF) in the Hamersley Province; and (2) an investigation of the Dales Gorge spherule layer (DGSL) (Lim, 2020). Samples for the Honours project were provided by Rio Tinto, and are from diamond drill exploration core DD15TPSR0001 at Mount Tom Price (Lim, 2020). The studied DGSL intersection occurs at a core depth of 611 m, stratigraphically within the DGS4 sub-member of the Brockman Iron Formation, or as referred to as DG1 in Lim (2020) according to the lithostratigraphic records provided by Rio Tinto Exploration (Fig. 1.5A).

This project further expanded the spherule sample suite investigated beyond the Dales Gorge spherule layer, to include a surface outcrop sample of the Bee Gorge spherule layer, also from the Pilbara (Fig. 1.5B). The Bee Gorge sample was also provided by Rio Tinto Exploration. This project focuses on samples from the Dales Gorge spherule layer (DGSL) and the Bee Gorge spherule layer (BGSL). The aim of the project is to better understand impact processes through formation of Archean impact spherules, based on their respective mineral assemblages, crystal habits, and microstructures. The main objectives of this investigation are to: (1) analyse feldspathic microkrystites in order to compare Archean impact spherule textures with transmitted light microscopy, backscattered electron (BSE) imaging, and electron backscatter diffraction (EBSD) mapping; (2) re-evaluate existing spherule classification schemes based principally on transmitted light microscopy, with new insights and methods from the BSE-EBSD results of this study; and (3) propose a vapor plume model based on the studied impact spherule characteristics in order to visualise where different feldspathic spherule microstructures may form in impact vapor plumes based on crystallisation features. The model only attempts to explain the crystallographic and morphological characteristics of the mineralogical constituents of feldspathic spherules or microkrystites, and does not discuss the origin of other impact particles present in these deposits. The classification scheme for spherule types presented here is largely adapted from those proposed by Sweeney and Simonson (2008) based on DGSL, and Krull-Davatzes et al. (2015), which is based on DGSL, the Paraburdoo spherule layer (not studied here), and a spherule layer in South Africa (also not studied here). The textural descriptions of Neoarchean spherules studied by Scally and Simonson (2005) is also used to refine the textural classification of Bee Gorge spherules.

Chapter 2 Materials and Methodology

2.1 Sample Preparation

2.1.1 Core Log and Polished Slabs

The DGSL sample is from diamond core DD15TPSR0001 (Fig. 2.1A). The Diamond core DD15TPSR0001 was viewed at the Rio Tinto Exploration compound in Belmont, WA. The core was drilled at Mount Tom Price in 2015 (GDA94; UTM Zone 50; 575021 mE, 7483441 mN). The core starts at 50 m depth below surface, immediately below a reverse circulation pre-collar, and ends at 744 m below surface (Fig. 1.5). The core was viewed in natural light with observations done for physical properties concentrating on stratigraphic units, bedding, banding, veining and reddening features, including structures and the spherule-bearing DGSL unit. The research material, the spherule-bearing DGSL unit, is a 6 cm thick ejecta horizon in shale (Fig. 1.2A), with thin (< 1 mm) stilpnomelane-quartz veins along fractures. The DGSL sample is dark grey, and signifies a relatively unaltered (un-oxidised) example of the spherule layer with a high density of spherules.

The BGSL sample is a polished slab from Munjina Gorge (Fig. 2.2A). The BGSL sample was collected from a surface outcrop located approximately 3.5 km south of Auski Roadhouse near Munjina Gorge, Karijini (GDA94; UTM Zone 50; 673670 mE, 7520950 mN) (Fig. 1.5B). The BGSL is generally orange-brown in appearance, and less dense in terms of spherule abundance (Fig. 2.2A), as compared to the DGSL sample. The density of spherules varies throughout the unit; spherules are abundant at the base, on top of a brown-reddish clay where they accumulated into a 3 cm spherule-rich section; spherules appear to be less abundant above the base of the 3 cm horizon (Fig. 2.2A). The horizon otherwise represents a normal graded sequence, which is typically observed in turbidites sequences in general, whereas the Bee Gorge member is known to contain volcaniclastic turbidites (Simonson, 1992; Hassler 1993; Simonson and Hassler, 1997; Simonson, 2003; Glikson, 2004, 2005). No fractures or veins were observed in the BGSL sample. The thin white line visible in the thin section image (Fig. 2.2C) was produced during the sample preparation stage due to breakage, and is filled with epoxy resin.

2.1.2 Thin Sections

Rio Tinto thin section 10335093 is a representative interval of the DGSL in core DD15TPSR0001 (Fig. 2.1C). A thin section was also prepared from the BGSL polished slab (Fig. 2.2C).

2.1.3 Epoxy Mounts

A total of five 2.54 cm-diameter epoxy mounts of chips of the samples were made at Curtin University. Three epoxy mounts were created for the DGSL (DGS4-1, DGS4-2, DGS4-3) (Fig. 2.1B), and two epoxy mounts were created for the BGSL (BGSL-3, and BGSL-4) (Fig. 2.2B). The epoxy mounts were ground and polished by hand, and given a final chemical-mechanical polish for EBSD using colloidal silica in NaOH (pH 10) with a Buehler Vibromet II polishing lap.

2.2 Optical Microscopy

The thin sections DGSL and BGSL-1 (Figs. 2.1C and 2.2C) were imaged in plane polarised light, cross-polarised light, and reflected light with a Zeiss Axio Imager m2m for full panorama navigation maps. The sections were further inspected with a Nikon LV100 Pol optical microscope imaging system for higher magnification images of selected features for microstructural studies of the ejecta spherules. A suite of 80 microphotographs of both thin sections were acquired in plane (PPL) and crossed (XPL) polarised light, and also using the gypsum accessory plate (GAP). The criteria of the sub-selection for optical microscopy records on both spherule layers are based on the best possible spherule that fits accordingly in both existing and modified classification schemes (see Section 3.3.1 and 4.3.1), which are further investigated in the electron microscopy (refer Section 2.3) to resolve and represent the diversity of internal textures of the spherules.

2.3 Electron Microscopy

SEM-EBSD analyses

Spherules with features of interest based on transmitted light images from each sample suite were analysed using scanning electron microscopy (SEM). The electron microscopy techniques include electron backscatter diffraction (EBSD) and energy dispersive spectroscopy (EDS). These investigations were conducted in the Microscopy and

Microanalysis Facility (MMF) at the John de Laeter Centre (JDLC) of Curtin University. The instruments used include a Tescan Mira3 field emission (FE-)SEM, and a Tescan Clara FE-SEM.

Backscattered electron imaging (BSE) was conducted on the five epoxy mounts to generate montage maps for each sample and also to take images of individual spherules. Selected spherules were examined and EBSD data were collected with Oxford Instruments AZtec EBSD/EDS acquisition systems and a Symmetry EBSD camera. Secondary electron (SE) and forescattered electron (FSE) images were collected to resolve contrasts among the minerals present. The EBSD analysis of spherules used an accelerating voltage (HT) of 20 kV, working distance (WD+Z) of 20 mm, stage tilt of 70°, dwell times per spot from 5 to 10 ms, refined accuracy indexing mode, and scan speed 2. Other EBSD mapping parameters based on spherule size are listed in Tables 2 and 7 for individual spherules from each horizon.

The EBSD study used match units for orthoclase-siderite-ilmenite for analysis of DGSL spherules, and orthoclase-dolomite-quartz-apatite for analysis of BGSL spherules. Different alkali feldspar match units were initially tested, and orthoclase was found to yield the lowest mean angular deviation values. Match units used include orthoclase from the American Mineralogist database, based on crystal structure data from Prince et al. (1973); ilmenite from the Inorganic Crystal Structure Database (ICSD [79278]; DB Family 27367), based on crystal structure data from Leinenweber et al. (1995); siderite from the American Mineralogist database, based on crystal structure data from Graf (1961); apatite from the American Mineralogist database, based on crystal structure data from Hughes et al. (1991); and dolomite and quartz match units from the Oxford HKL database. Other accessory minerals observed include zircon, rutile, titanite, monazite, and various sulphides (see Section 3.2.5). No attempts were made to index stilpnomelane during EBSD analysis, as clay minerals are difficult to index because (a) they can be difficult to polish and (b) some clays do not yield EBSD patterns due to nano-scale complexities in crystal structure. The EBSD results and spherule internal textures and microstructures are described in Section 3.2 and Section 4.2.

EBSD Post-Acquisition Data Processing

The Oxford software program AZtecCrystal was used to process EBSD data for individual spherules. The EBSD data provide both crystallographic orientation and spatial microstructural information that can be presented as various maps. Such maps include: band contrast (BC) maps that show the quality of electron backscatter diffraction patterns as a function of contrast of the diffraction bands from a background value; phase maps that show selected mineral phases with user-defined solid colours; inverse pole figure (IPF) maps show crystallographic orientation using a colour scheme in IPF space as a function of crystallographic orientation in the sample reference frame.

Two data filtering routines in AZtecCrystal were applied to improve presentation of the data. The first is the ‘wildspike’ algorithm, which removes errant pixels if their phase and/or orientation value is significantly different from the surrounding eight nearest neighbours. The wild spike is used to remove mis-indexed pixels. The second data filter routine is the ‘zero solution’ algorithm, which progressively (iteratively) fills non-indexed pixels according to user-defined parameters. A zero solution was applied to all spherule maps here, which featured eight nearest neighbours (max of 10 iterations allowed, but more often only 2 occurred), followed by seven nearest neighbours (max of 10 iterations allowed).

An automated grain size detection of alkali feldspar crystals using the AZtecCrystal software was also attempted, however, difficulties were encountered due to the presence of cross-cutting stilpnomelane crystals on the 2D polished surface, which broke individual feldspar crystals into multiple segments. Due to the stilpnomelane overprints, feldspar grain lengths detected yielded smaller values than that expected from the actual crystal sizes visible in the EBSD maps. This resulted in one or multiple divisions of a single feldspar grain, which produces artificially and erroneously smaller alkali feldspar grain lengths than are inferred to exist in 3D (see Section 3.3.2, and Fig. 3.4). Representative grain length measurements were instead made manually on various feldspar occurrences. Hence, only a few feldspar crystals with unique features from representative DGSL spherules were selected to record crystal sizes using a measuring tool in AZtecCrystal. Note also that some crystals might not be polished parallel to the original elongation direction.

Similar issues were encountered for alkali feldspar in BGSL spherules. However, it was not due to cross-cutting minerals. In the case of BGSL feldspars, the creation of apparent porosity and or a polycrystalline microstructure for alkali feldspar during pseudomorphism of plagioclase again resulted in the segmentation of alkali feldspar grains (refer Section 4.2.1.1 and Fig. 4.3). The elongated feldspars grains that have been assigned with similar orientations are observed to consist of many smaller grains with adjacent grain boundaries, which prevents the automated software from recognising them as a single grain.

Chapter 3 Dales Gorge Spherule Layer

3.1 Geological Background

3.1.1 General Description of the Dales Gorge Member

The Dales Gorge Member is the most ferric-concentrated stratigraphic member within the Hamersley Basin, with intense reddening features associated with burial metamorphism and veining processes. The DGSL spherule layer is principally hosted within the ~4 m thick, stilpnomelane-rich, DGS4 macroband (fourth shale band of Dales Gorge Member), and is one of the most well-studied spherule occurrences on Earth due to the economic significance of the Dales Gorge Member in iron mineralisation exploration (Simonson, 1992, Pickard et al., 2004; Thorne, 2015). The DGSL was initially interpreted to be of volcanic origin, with spherules considered to be unusual volcaniclastic grains (Simonson, 1992; Glikson and Allen, 2004), but later they were confirmed as distal impact ejecta spherules, hosted by the shale-dominant DGS4 unit associated with reworked volcaniclastic detritus, and containing relatively high iridium anomalies (Glikson and Allen, 2004; Glass and Simonson, 2013). The radiometric age constraint of DGSL is 2495 ± 16 Ma, based on U-Pb SHRIMP results from neighbouring tuff units (Table 1) (Glikson and Allen, 2004; Trendall et al., 2004; Sweeney and Simonson, 2008).

Previous studies have documented the DGSL in both surface outcrops and within diamond drill cores across the Hamersley Basin. Surface samples and descriptions of the spherule-bearing DGS4 unit were established from several localities: Wittenoom Gorge (Simonson, 1992; Glass and Simonson, 2013), Dales Gorge (Hassler and Simonson, 2001); Sweeney and Simonson, 2008), Yampire Gorge (Sweeney and Simonson, 2008), and a recently discovered site in Munjina Gorge (Hassler et al., 2019). In contrast, less-weathered drill core occurrences include the DDH4 core from Paraburdoo mine (Pickard et al., 2004), the A00-811 and DDHS96-0 cores from Mount Tom Price (Pickard et al., 2004), and the DD15TPSR0001 core from Mount Tom Price, which is described here for the first time.

Spherules were deposited at the base of the lower DGS4 sub-member, where the variation in spherule shape, density of packing (spherule accumulation) and size are interpreted to represent depositional processes in a Precambrian ocean (Simonson, 1992). This unit is comparable to the description of Division 1 in Hassler et al. (2019), the unstratified spherule-bearing stilpnomelane-dominant shale unit of the lower fourth DG shale band, with an overlying sequence of finely laminated chert-shale units (Division 2). The DGSL occurs as a spherule lens in DGS4 that ranges between 14 and 110 cm thick, with an average of 25 to 75 cm (Glass and Simonson, 2013). However, this was recognised as a microkrystite spherule unit (MKR) in Yampire Gorge asbestos mine, with an aggregate thickness range from 10 to 30 cm (average of 20 cm) across the Hamersley Province (Glikson, 2004).

There are at least two distinctive internal stratigraphic patterns observed in the DGSL sequence in different locations, which provide information on the paleoslope and depositional environment. For instance, most of the DGSL (referred to as DS4 impact layer in Hassler et al., 2019) from Munjina Gorge mine are debritic, poorly sorted and matrix-supported with an abundance of reworked-brecciated intraclasts. Similarly, the DGSL in the Wittenoom Gorge section also comprises from angular boulder-cobble sized ferruginous chert and fragmented BIF, up to pebbled sized shale and chert intraclasts in the spherule-bearing shale domain (Hassler and Simonson, 2001; Pickard et al., 2004; Hassler et al., 2019). The Paraburdoo site samples (referred as PA section in Hassler et al., 2019) show a similar sequence, but are overall finer in grain size, with spherules dominant at a slightly higher position from the DGS4 base (Pickard et al., 2004). These debritic shale occurrences comprise a lower spherule concentration overall, as compared to the following stratigraphic sections.

In comparison, the Dales Gorge, Yampire Gorge, Mount Tom Price sites of the DGSL are classified as deeper depositional environments, without a significant presence of intraclasts (Hassler et al., 2019). The base of DGS4 in this category is almost fully constituted by coarse to very coarse-sand sized spherules and fragmented spherule particles that are associated with symmetrical dune-like wave-dominated symmetric bedforms with varied dune wavelengths and heights (Hassler and Simonson, 2001; Hassler et al., 2019). These components are relatively rounded and finer as compared to the Munjina-Wittenoom occurrences, with a denser spherule accumulation and wave-generated structures as well. This is often expected as low-energy and calmer deep marine deposition (Glass and Simonson, 2013). However, a new Yampire Gorge specimen investigated in Hassler et al. (2019) may contradict this finding. Unlike the other sections that shows dune-like wave structures, the new results of a spherule-rich unit (Division 1) from Yampire Gorge section comprise an inconsistently spaced hummocky bedform, which varied in thickness laterally in the studied cross section, where the overlying upper unit that lacks visible spherules (Division 2) was deposited with consistent thickness across the horizontal scale (Hassler et al., 2019).

It has been proposed in some studies that DG spherules originated as basaltic melt droplets (microtektites), rather than as vapor condensates (microkrystites), suggesting they are relatively proximal (microtektite) to their source, rather than representing distal ejecta (microkrystite) (Sweeney and Simonson, 2008; Hassler et al., 2019). However, Glass and Simonson (2013) described the DGSL as an undisturbed distal product of a direct fallout over 200 km. Glikson and Allen (2004) estimated the projectile diameter responsible for the DG impact spherules using equations from O'Keefe and Ahrens (1982) and Melosh and Vickery (1991), which yielded bolide diameters of 15–25 km and 16–30 km, respectively. Johnson and Melosh (2012) further calculated the Dales Gorge impactor diameter ranged from 31- 40 km.

In summary, prior studies suggest a rather complex depositional history of the spherule-bearing DGS4 shale laterally, and it may be variable between locations (Hassler et al., 2019; Hassler and Simonson, 2019). The north-directed paleocurrent of the Wittenoom-Munjina Gorge occurrences suggest a possible higher paleoslope or a relatively shallower water paleoenvironment in the northern margin of Hamersley Basin, related to one or multiple poorly cohesive debris flows (Hassler et al., 2019). The origin of the Paraburdoo debrite was proposed either as a distal Wittenoom-Munjina equivalent in the southern Hamersley Basin margin, or that it was deposited by a north-travelling debris flow along with the slope reversal associated with the deposition of Dales Gorge member. Given the unusual development of the hummock structures in the new tsunamigenic Yampire samples, this may suggest a complex reworking history either associated with standing waves within the turbidity current, or by bottom return flow of the spherule-related impact tsunami (Hassler et al., 2019; Mulder et al., 2009).

3.1.2 Previous Studies on Dales Gorge Impact Spherules

Spherule shapes in the DGSL range from equant-circular-oblate shapes to various splash forms, including dumbbell and teardrop shapes (Fig. 3.1B-D, G-H). Most spherules shapes are well preserved, as early stilpnomelane cementation is interpreted to have contributed to shielding the spherules from later compaction (Sweeney and Simonson, 2008; Glass and Simonson, 2013). The truncations and/or agglutination of splash form spherules are proposed to have taken place during rapid spinning of impact droplets. Both fragmentation or collision of particles may take place in flight, which resulted in various spherule shapes (circular to splash forms) (Glass and Simonson, 2013).

The Dales Gorge spherules are principally composed of two main minerals: alkali feldspar, that is interpreted to have pseudomorphically replaced plagioclase, and stilpnomelane, which is interpreted to have replaced original impact glass (Glikson and Allen, 2004; Trendall et al., 2004; Glass and Simonson, 2013). The mineralogy of Dales Gorge impact spherules differs between surface outcrop samples and drill core samples, principally due to weathering. Outcrop samples are more profoundly weathered, and contain oxidised stilpnomelane, with decreased abundances of alkali feldspar, carbonates and opaque minerals; the weathering also imparts a distinctive reddish colour (Fig. 3.1H) (Sweeney and Simonson, 2008; Glass and Simonson, 2013). In contrast, core samples are typically darker grey, because they are less weathered and oxidised (Fig. 2.1A-B) (Pickard et al. 2004; Glass and Simonson, 2013).

Alkali feldspar microlites in DGSL have previously been interpreted to have replaced original plagioclase feldspar (Sweeney and Simonson, 2008; Glass and Simonson, 2013). This interpretation is based on the similarity of crystal habits of alkali feldspar grains within spherules, as viewed in transmitted light, to those produced in plagioclase during experimental quenching of basalt (Lofgren, 1971, 1974). Such habits include laths and skeletal shapes with dark central stripes, and also 'bow-tie' or rosette-type clusters, with fibrous-acicular-needles radiating inwards to the core. Botryoidal textures have been reported in both the basaltic plagioclase experiments, and in multiple impact spherule layers from the Hamersley basin (Simonson, 1992; Glass and Simonson, 2013).

Stilpnomelane is abundant across the entire DGSL. It occurs as the matrix groundmass, and also replaced the initially glassy cores and filled vesicles within impact spherules. Stilpnomelane is suggested to have precipitated during diagenetic-low grade metamorphism, possibly via spherule fractures or latter formed thin veins. Sweeney and Simonson (2008) suggested that stilpnomelane might be part of the extra-terrestrial impact component. They have suggested that some of the high Ni and Ir in local stilpnomelane tuffs present in DGS4 might represent a mixture of igneous and impact projectile components, with iron-rich pore fluid alteration (Glikson and Allen, 2004). Other stilpnomelane-rich shale macrobands studied in the DGS4 spherule layer do not appear to correspond to existing igneous compositions. Hence, it is thought that stilpnomelane likely originated as volcanic ash (Glikson and Allen, 2004), although extra-terrestrial origins cannot be completely ruled-out (Glikson and Allen, 2004; Sweeney and Simonson, 2008).

3.2 Results: Description of Investigated Dales Gorge Spherules

Selected Dales Gorge spherules were examined with scanning electron microscopy and electron backscatter diffraction mapping (SEM-EBSD), and compared with corresponding transmitted light micrographs in order to better characterise the spherules. This analysis includes a description of the minerals identified and their respective crystal habits, and the classification of spherules into different categories according to existing classification schemes (Table 2, 3, 4). The thin section investigated is 10335093 (Fig. 2.1C), which is also referred to as DGTS for brevity. A total of 80 feldspathic spherules were documented with transmitted light microscopy (Table 4). A subset of 25 of the 80 spherules were subsequently mapped by EBSD (Table 2). The DGTS investigation prioritised resolving the mineralogy and microtextural features of the selected feldspathic spherules. Most spherules were also observed using backscattered electron imaging (BSE) and secondary electron images (SE). Detailed energy dispersive spectroscopy maps (EDS) were made of 5 Dales Gorge spherules, including DGTS-S6, -S8, -S24, -S46, and -S70.

3.2.1 Orthoclase

Feldspathic spherules are optically bright in plane polarised light (PPL) (Fig. 3.2A) and display low first-order-grey interference colours under crossed polarised light (XPL) that are readily distinguishable from the brown stilpnomelane-rich matrix. Orthoclase is the most dominant mineral in the Dales Gorge feldspathic impact spherules (Fig. 3.2), as it comprised up to 60.4% of a given spherule (Table 5). EBSD mapping showed that occurrences of orthoclase were spatially variable in different spherules (see below, and Section 3.2.2.4).

3.2.1.1 Textural comparisons between spherule and matrix

In addition to feldspathic spherules, orthoclase also occurs as a matrix phase in the sedimentary groundmass of the DGSL. Matrix orthoclase grains coexist with the dark stilpnomelane matrix in transmitted light images. However, orthoclase in spherules and matrix differs significantly, and are readily distinguished based on grain length and crystal habit, as defined in EBSD maps. The two occurrences of orthoclase thus have different origins. For example, in the vicinity of spherule DGTS-S1, matrix orthoclase occurs as polycrystalline or blocky grains with irregular, non-acicular, subhedral to anhedral shapes that range from 1.1 μm to 37.4 μm (e.g., Fig. 3.3C). In contrast, the grain length of the fibrous fans to acicular laths of orthoclase microlites within the feldspathic spherules varied from 45 μm to 150 μm across both fan and bowtie structured domains (Fig. 3.3F) (see Section 3.2.1.2).

3.2.1.2 Feldspathic Spherule Internal Textures: Radial-type and Random-type

Two main morphologies of orthoclase crystal growth habits/patterns were observed in the studied spherules: (1) radial textures, and (2) random textures. The differences between these two types are described in the following sections.

Spherules with Radial Microlites

Spherules with radial-type textures share a similar microstructure consisting of well-developed acicular orthoclase microlites that occur in clusters, most of which radiate inwards from nucleation points on or near the outer margin of the spherule. A total of 42 of 80 (53%) Dales Gorge spherules examined in transmitted light have radial-type textures (Table 4). Of the 25 spherules mapped by EBSD, 14 of 25 (56%) are radial-types (Tables 5, 6).

Within the radial-type spherule group, several conspicuous orthoclase crystal habit variants were observed, including spherules with (1) inwards-radiating acicular fans that form a botryoidal boundary with a former glassy core; (2) bowtie spherulite clusters, consisting of two opposing fan-shaped spherulites radiating from a common nucleation point, and (3) fasciculate microstructures, consisting of an oval shaped spherulite cluster with acicular crystals radiating from an elongate prismatic crystal (Lofgren, 1974). We acknowledge the possibility that some of the acicular fans may be part of an original bowtie structure in the 2D polish section obtained in this study.

Both fan-shaped and bowtie structured orthoclase spherulites are common in all radial-type Dales Gorge spherules (Fig. 3.4). For instance, in one spherule a bowtie-structured orthoclase was measured with a crystal length of 135 µm (Fig. 3.4A(ii)); whereas the fan-like microlites range in length, from a shorter fan of 45 µm (Fig. 3.4B(ii)), to a longer variant of 200 µm (Fig. 3.4 C(iii)), with average length around 100 µm. The internally developed orthoclase spherulites morphologies (fans, bowties, fasciculate) have previously been reported in transmitted light images of Dales Gorge spherules (Sweeney, 2002; Sweeney and Simonson, 2008). They have been compared to classic spherulite quench textures displayed by plagioclase crystallising in experiments on basalt (e.g., Lofgren, 1974; Zheng et al., 2018); such experiments have shown a relation exists between plagioclase crystal growth habits and differences in (super)cooling rates.

Some feldspathic radial-type spherules in DGTS preserve a conspicuous core-rim structure visible in transmitted light images (16 of 80, or 20%, Table 4). Of these, 3 were mapped by EBSD (3 of 25, or 12%, Tables 5, 6), including S28, S32 and S70. The rim structures have variably developed botryoidal textures. Spherule DGTS-S70 contains a rim of inward-radiating orthoclase fans that define a well-formed botryoidal boundary with the altered glass core (Fig. 3.5). The core consists of fibrous stilpnomelane that is interpreted to have replaced quenched impact glass during diagenesis. A conspicuously circular vesicle is also present, which has been filled with fibrous stilpnomelane in a radiating pattern that is distinguishable from the formerly glassy core (Fig. 3.5A, E). Spherule S70 exhibits alkali feldspar microlites with weaker band contrast (Fig. 3.5C, D, F) as compared to other radial-type Dales Gorge spherules (e.g., Figs. 3.2 to 3.4). The weaker microlite band contrast in spherule S70 is attributed to the apparent partial crystallisation/quenching history that prohibited further growth of the radial microlites. The original glass core and vesicle were both subsequently diagenetically altered to stilpnomelane after deposition.

Spherules with Random Microlites

Spherules with random-type textures have a microstructure consisting of orthoclase crystallites with prismatic and/or tabular habits that occur in seemingly random growth patterns (see Fig. 3.6). A total of 19 of 80 (24%) of Dales Gorge spherules examined in transmitted light contain random-type textures (Table 4). Of the 25 spherules mapped by EBSD, 11 of 25 (44%) preserve orthoclase grains with random-type textures (Tables 5, 6). The length of orthoclase grains in random-type spherules is generally smaller than those in radial-type spherules. For example, random-type spherules DGTS-S24 (Fig. 3.7) and S43 (Fig. 3.8) contain grains with an average length of 3 μm to 3.5 μm, whereas random-type spherule DGTS-S29 contains grains with a slightly longer average crystal length of 6.4 μm (Fig. 3.6B(b)).

Dust Rims around Spherules

Rims of fine-grained ‘feldspar dust’ were observed in 2 of 25 (8%) of the Dales Gorge spherules mapped by EBSD. Spherules DGTS-S1 (Fig. 3.3D) and DGTS-S9 (Fig. 3.9D, E) provide good examples of dust rims, as EBSD analysis resolved the ultrafine-grained rims that were otherwise not visible in transmitted light images. The sub-micrometre dust-sized particles form a rim, or film, of variable thickness around the exterior of spherules. The irregular dust rims in S1 and S9 are measured by their thickest width (Fig 3.17 C, F), which are 34 μm and 50 μm, respectively. The EBSD maps identified the main mineralogical component of the dust as orthoclase, which has a significantly smaller grain size as compared with other orthoclase within the spherules (e.g., fan microlites, laths, equant-tabular textures), and well as orthoclase in the matrix. The presence of dust rims was only observed on radial-type spherules; they were not observed on random-type spherules. Dust rims thus were identified on 2 of 14 (14%) of the EBSD mapped radial-type spherules. The dust rims are discussed further in Section 3.3, and also in the context of radial-type spherule formation (Section 5.3).

Spherules with Blocky Orthoclase

A blocky form of orthoclase grains occurs both (a) in the matrix, (b) along the edges of vesicles within spherules, and (c) along spherule margins. For example, in DGTS-S9 (Fig. 3.9), the spherule mainly exhibits fan-radiating to bowtie microstructures. However, orthoclase with granular to blocky crystal shapes is seen lining the vesicle boundary (Fig. 3.9D, E). Blocky feldspar grains also occur in the matrix adjacent to the spherule S9 (Fig. 3.9D). Similar blocky orthoclase grains also occur in DGTS-S43, both as grains lining the vesicle wall, and along the margin of spherule S43 (Fig. 3.8D, F). The similarity of crystal shapes suggests that both occurrences of blocky feldspar grains are likely a result of post-deposition diagenetic fluids as a cement, triggering crystallisation into an initially empty vesicle, coeval with precipitation of the blocky-granular orthoclase grains around spherule exterior surfaces (Fig. 3.8F).

3.2.2 Ilmenite

Ilmenite is nearly a ubiquitous phase in Dales Gorge spherules. However, like orthoclase, ilmenite displays a variety of habits and occurrences. Observations of ilmenite in Dales Gorge spherules in transmitted light images are difficult due to the obscuring stilpnomelane overprint. However, some spherules preserve large elongate ilmenite crystals that are readily visible as an opaque phase in transmitted light images (e.g., Fig. 3.12A, D). The following sections describe the three main occurrences of ilmenite resolved by EBSD analyses: (a) linear ilmenite arrays consisting of discontinuous grains (Fig. 3.10A, B); (b) ilmenite lining spherule margins (Fig. 3.10C, D); and (c) disseminated ilmenite grains intergrown with orthoclase within spherules (Fig. 3.10E, F).

3.2.2.1 Ilmenite Arrays

The term ‘ilmenite arrays’ in the context of this study refers to ilmenite grains that are visible in transmitted light as a nearly continuous elongate opaque mineral (Fig. 3.12A, D). In EBSD maps, ilmenite arrays are identified as consisting of a linear group of adjacent grains with a close spatial association that share a common (or nearly so) crystallographic orientation

(Fig. 3.11, 3.12). A total of 18 of 25 (72%) of Dales Gorge spherules analysed by EBSD contain ilmenite arrays. They have a strong shape preferred orientation (SPO) that is typically aligned with the observed trace of the opaque phase in plane polarised light images. EBSD analysis shows that individual arrays also have a strong crystallographic preferred orientation (CPO). A given array consists of aligned but discontinuous ilmenite grains (adjacent, but not always touching) that define a systematic twinning relationship (Figs. 3.11 and 3.12). Analysis of the disorientation angle (minimum misorientation) produced by the twinning was accomplished using the AZtecCrystal software (Fig. 3.13). Histograms of disorientation relations consistently identify the twin relationship as 60°/<0001>. The presence of systematic twins indicates that the ilmenite arrays did not form randomly (see Section 3.4.2 and Fig. 3.14).

3.2.2.2 Ilmenite Lining Surfaces

Ilmenite also occurs as individual grains along various surfaces of spherules; in all cases, ilmenite grains can form a conspicuous circular ring pattern on polished samples. The equant to tabular ilmenite crystals with these features are mostly sub-micrometre in size. A total of 10 of 25 (40%) of the Dales Gorge spherules analysed by EBSD have marginal ilmenite lining spherule surfaces. Three different occurrences of ilmenite lining surfaces are distinguished (Table 6): (1) ilmenite lining the exterior spherule surface (Figs. 3.15 and 3.16), (2) ilmenite lining dust rims deposited on the exterior spherule surface (Figs. 3.17 and 3.18), and (3) ilmenite lining vesicle walls (Fig. 3.19).

3.2.2.3 Disseminated ilmenite

A total of 5 of 25 (20%) of Dales Gorge spherules analysed by EBSD preserve disseminated ilmenite grains intergrown with orthoclase (Fig. 3.20) (Table 6). Disseminated ilmenite often occurs within the random-type population of feldspathic spherules. This occurrence of ilmenite is distinguished from occurrences of ilmenite in the matrix groundmass of the DGSL, as the latter is assumed to be either unrelated to the spherules, or possibly originated from ilmenite in broken spherule fragments that are highly altered.

3.2.2.4 Crystallographic Orientation Relationships Between Orthoclase and Ilmenite

In most DGSL spherules analysed by EBSD, the crystallographic orientations of orthoclase and co-existing ilmenite do not appear to influence one another (e.g., Fig. 3.21). No obvious crystallographic-preferred orientations (CPO) shared by the two phases were observed in EBSD orientation maps and pole figures, in either radial or random-type Dales Gorge spherules, regardless of the ilmenite habits. However, ilmenite in DGSL-S31 is conspicuously spatially related to the orthoclase distribution (Fig. 3.22). In all areas where orthoclase was indexed by EBSD, it is intergrown with ilmenite; whereas in areas without ilmenite the orthoclase indexed poorly (Fig. 3.22D). The co-existence relationship implies that there is some type of phase equilibrium between orthoclase and ilmenite (see Fig. 3.22D-F). In the same spherule, both phases are intergrown in a conspicuous fasciculate habit, which suggests a shared SPO between the two phases (Fig. 3.22A, E, F). However, crystallographic orientation maps and pole figures do not reveal a convincing CPO between orthoclase and ilmenite (Fig. 3.23B, C). Orthoclase in the fasciculate structure forms one dominant cluster with a highly dispersed orientation, as shown in {100} and {001} pole figures (Fig. 3.23B, C). Each of the orientation plots/cluster defines consistently high angular dispersion arrays of range about > 90°, where other orthoclase data plots are scattered in various orientations. Moreover, the various clusters of ilmenite {0001} poles with low dispersion do not coincide with any low-index poles in orthoclase. The reason for the lack of a CPO between these two phases is unclear. Fasciculate growth structures are most commonly reported from nucleation of plagioclase-pyroxene intergrowths prior to quenching of mafic melts (Walker et al., 1978; Boyd et al., 1984; Francis et al., 1986) . Furthermore, the random textured orthoclase crystals in random-type Dales Gorge spherules often occur in the presence of disseminated ilmenite (Fig. 3.7 and 3.8).

3.2.3 Stilpnomelane

Stilpnomelane is the dominant mineral in the Dales Gorge spherule layer, and is entirely attributed to post-deposition diagenesis. It is assumed to have formed under sub-greenschist facies conditions, related to burial (Miyano and Miyano, 1982; Miyano, 1982). Haugaard et al. (2016) proposed that the very fine-grained greenish brown stilpnomelane might also originate from reworked volcanic ash. The matrix groundmass of the DGSL is almost entirely composed of stilpnomelane (e.g., Figs. 3.5A, 3.8A, 3.12A and D). Stilpnomelane in cores of Dales Gorge spherules (e.g., Fig. 3.5) has previously been interpreted to have replaced original impact glass during post-depositional diagenesis (e.g., Glikson and Allen, 2004).

3.2.4 Siderite

Siderite is a common matrix phase in the DGSL, as well as the shale host and other BIF in the Hamersley Group (Taylor et al., 2001; Morris and Kneeshaw, 2011; Tosca et al, 2016). It is an iron carbonate that forms large euhedral rhombs and other blocky textures in the DGSL (e.g., Fig. 3.3D, 3.9D) The occurrence of siderite in the DGSL is interpreted as a diagenetic phase that locally overprinted some Dales Gorge impact spherules (e.g., Fig. 3.7D). The post-depositional origin of siderite in the DGSL has previously been noted (Jiang and Tosca, 2019; Muhling and Rasmussen, 2020).

3.2.5 Other Accessory Phases

Other accessory phase observed in the DGSL samples analysed here include zircon, various sulphides, rutile, titanite, apatite, monazite. Besides sulphides, some of these accessory phases have been recognised elsewhere as possible impact indicators, because they are capable of preserving microstructural shock evidence (e.g., planar deformation features) associated with impact-related hypervelocity processes (Timms et al., 2017, 2019). However, due to the low abundance of these phases in the DGSL, with most only present in the matrix groundmass, it is likely that they are unrelated to the impact history in DGSL. Hence, only limited analyses were done on these phases.

For example, clusters of zircon grains identified in DGTS are extremely irregular and scattered within the stilpnomelane matrix (Fig. 3.24A). The zircons lack crystallinity, and did not yield diffraction patterns (Fig. 3.24B). Furthermore, SEM-EDS analysis of several sulphide phases showed arsenic, nickel, and cobalt peaks (Fig. 3.25A, B), indicating they are likely one of the gersdorffite-cobaltite sulfarsenides (NiAsS-CoAsS-FeAsS end members) identified by Fanlo et al. (2004) (Fig. 3.25C). Some TiO_2 crystals were observed within spherules. Both rutile (Fig. 3.24C) and anatase (Fig. 3.24D) with polycrystalline textures. A complex twining relationship within one rutile is expressed by minimum misorientations between host and twin of 65°/<100> and 65°/<010>, whereas anatase is twinned with a host-twin minimum misorientation of 55°/<001>.

3.3 Discussion

3.3.1 Classification of Dales Gorge Spherules

Existing classification schemes for Dales Gorge spherules are based primarily on transmitted light observations (Sweeney and Simonson, 2008; Krull-Davatzes et al., 2015). Emphasis has been placed on categorisation of Dales Gorge spherules based on texture and mineralogy. Sweeney and Simonson (2008) recognised six spherule populations in the DGSL, including radial-type, random-type, rimmed, massive, miscellaneous, and indeterminate (Table 3). Krull-Davatzes et al. (2015) expanded the classification scheme by considering spherules from the Dales Gorge spherule layer, the Paraburdoo spherule layer, and an impact spherule horizon from South Africa, and proposed eight petrologic populations of spherules (Table 3). There are many similarities in the two spherule classifications schemes; a combined table listing for both classification schemes is provided for a comparison (Table 3).

This study focused exclusively on feldspathic microkrystites in the DGSL, and so not all of the previously identified spherule types were analysed. Four different spherule types from both the Sweeney and Simonson (2008) and Krull-Davatzes et al. (2015) classification schemes were analysed here, including radial-type, random-type, rimmed-type, and miscellaneous-type. Modifications to the existing spherule categories made in this study are summarised below:

(1) Radial-type spherules. The defining characteristic of feldspathic radial-type spherules are the presence of inwards-radiating acicular alkali feldspar crystals, recording nucleation and growth of feldspar initiated from the spherule edge or near boundaries. The radial-type category also includes spherules with spherulitic textures, such as fan-like spherulites, bowtie spherulites, and fasciculate spherulites. Some radial-type spherules contain filled vesicles, which are often centrally located.

(2) Random-type spherules. The defining characteristic of feldspathic random-type spherules is that they do not preserve evidence of radial alkali feldspar growth (i.e., they do not contain orthoclase spherulites). Random-type spherules largely consist of randomly oriented to weakly aligned alkali feldspar laths that are tabular to prismatic in shape. Some random-type spherules contain filled vesicles, but they generally do not contain large centrally located vesicles.

(3) Glass core-type spherules. The previously identified ‘rimmed’ category of feldspathic spherules is here replaced with a new category termed glass core-type spherule. The defining characteristic of glass core-type spherules is the presence of a concentric core or an irregular interior region of the spherule that did not crystallise feldspar. The so-called glass cores are interpreted to have once existed as poorly crystalline quenched feldspathic glass that has been altered during post-depositional diagenesis. Glass core-type spherules can contain centrally-located vesicles, and the boundary between the radial growth and glass core can have a botryoidal morphology in some spherules. This category is not included in the final classification, as glass core type spherules are effectively a sub-set of radial-type spherules. Most glass core type spherules preserve some evidence of partial radial inward crystallisation.

(4) Feldspathic spherules that do not fit in any of the above categories were identified simply as miscellaneous-type spherules. Miscellaneous-type spherules were categorised, but largely neglected during this study.

The 80 Dales Gorge spherules in the DGTS thin section were first classified based on characteristics observable in transmitted light microscopy, including plane polarised light (PPL), cross-polarised light (XPL) and images with the gypsum accessory plate (GAP) (Table 4). After EBSD analysis of a sub-set of 25 spherules, the spherules were further classified (Table 5, 6). The final classification includes (1) observation of ilmenite textural occurrences, (2) the crystallinity of spherules; (3) subdivision into spherulitic textures: fan, bowtie, fasciculate, and spherical (Table 5).

3.3.2 Orthoclase as a Pseudomorph After Plagioclase

Orthoclase in Dales Gorge spherules preserves what appear to be primary crystal growth habits and textures (e.g., acicular crystals, Carlsbad twins, various spherulite morphologies) representative of those that initially formed as high-temperature crystallites (Fig. 3.6B). However, most studies interpret the orthoclase occurrences in DG spherules as having a post-depositional origin. In this context, orthoclase pseudomorphed original plagioclase that crystallised from melt droplets of broadly basaltic composition during diagenesis (Sweeney and Simonson, 2008; Glass and Simonson, 2013; Krull-Davatzes et al., 2015). Diagenetic orthoclase would thus have formed, perhaps in equilibrium with, diagenetic stilpnomelane and siderite (e.g., Fig. 3.2). The habit and occurrence of orthoclase in the matrix outside of spherules (e. g., Fig. 3.3C, D) is remarkably different from orthoclase crystals within spherules (Fig. 3.3C, F). Irrespective of the timing of orthoclase formation, the pronounced division of acicular orthoclase crystals by cross-cutting stilpnomelane crystals (e.g., Figs. 3.15B and E, 3.3F) indicates that diagenetic stilpnomelane mostly likely formed after orthoclase.

3.3.3 Ilmenite Intergrown with Alkali Feldspar

Ilmenite in this study is not necessarily in textural equilibrium with orthoclase; most pole figures do not show any coincidence of growth directions between the two phases. Ilmenite arrays within spherules might instead result from exsolution. Ilmenite has previously been reported to form by exsolution at about 600°C from magnetite inclusions in plagioclase (Bian et al., 2021). Because plagioclase is twinned, it tends to form a titanomagnetite inclusion within the Carlsbad-twinned lattice, and exsolved into ilmenite lamellae at the end stage (Bian et al., 2021), leaving lamellae of ilmenite tracing the original elongated shape as magnetite dissolved with other exsolved minerals (e.g., orthopyroxene, mica). Similar descriptions of ilmenite exsolution in olivine have been suggested to occur at ultra-high-pressure metamorphic conditions (UHP) (Moseley, 1981; Massonne and Neuser, 2005). Another potentially relevant reports of the internally discontinuous texture were recorded by Hassler et al. (2011), as they described the presence of chain-like pseudomorphs of ferromagnesian crystals in both Paraburdoo (Western Australia) and Reivilo (South Africa) spherule layers.

In DGTS_S31, the intergrowth of ilmenite inclusions in fasciculate orthoclase domains may suggest a different development history. As mentioned in Section 3.2.2, the fasciculate structures may be related to the nucleation of plagioclase-pyroxene (Walker et al., 1978; Boyd et al., 1984; Francis et al., 1986). According to Lofgren (1971), the sheaf-like structure or fasciculate structures in rhyolite glass are experimentally formed by devitrification at 500°C.

3.3.4 Formation of Dales Gorge Spherules as Silica-Rich Melt Droplets

Two different types of feldspathic microkrystite spherules were documented in the Dales Gorge spherule layer: radial-type spherules (some with formerly glass cores), and random-type spherules. Radial-type spherules are characterised by acicular orthoclase (formerly plagioclase) crystals that appear to have mostly nucleated from the spherule surface (e.g., Figs. 3.3, 3.9). The presence of conspicuous dust rims on some spherules provides direct evidence that impinging dust may have triggered nucleation of the original feldspar crystals. In contrast, random-type spherules contain fine-grained alkali feldspar crystals, without evidence of externally triggered growth (e.g., Fig. 3.6). The population of random-type spherules are interpreted to have formed from higher nucleation rates and lower growth rates as compared to radial-type spherules. The crystal length variation between equant (shorter laths) and prismatic (longer laths) may reflect longer crystallisation time in a relatively hotter environment, and/or a lower degree of supercooling (quenching) of the initial melt. Dust rims were not observed around random-type spherules.

Chapter 4 Bee Gorge Spherule Layer

4.1 Geological Background

4.1.1 General Description of the Bee Gorge Member

The BGSL was originally referred to as both the Wittenoom spherule layer (Simonson et al., 2009) and the Spherule Marker Bed (SMB) (Simonson, 1992). It was later renamed as the Bee Gorge spherule layer (BGSL) by Glass and Simonson (2013), as subsequent studies distinguished the BGSL from an older impact spherule layer in the lower Wittenoom Formation, now known as the Paraburdoo spherule layer (PSL). The BGSL is stratigraphically deposited in the Bee Gorge member as the top-most unit of the Wittenoom Formation, and directly overlies the Paraburdoo member (Simonson, 1992; Glass and Simonson, 2013).

The Bee Gorge member contains a heterolithic sequence which includes interbeds of argillite, dolomite, limestone, BIF, chert and volcaniclastics. According to Glass and Simonson (2013), the BGSL is exposed in the main outcrop area of the Hamersley Basin, characterised by weathered coarse groundmass, and shows a grading pattern with sharp thinning and finer components from the northeast towards the southwestern area of the basin. Similarly, Simonson (1992) recognised three distinctive paleogeographic zones with downslope sedimentary characteristics. Zone A represents the coarsest and thickest in the northeast area, Zone C represents the thinnest and finest sediments indicating a deep paleoslope in the south to southwestern area, and Zone B represents an intermediate region without significant differences in spherule depositional features (Simonson, 1992; Hassler and Simonson, 2001; Glass and Simonson, 2013). The above observations indicate a reserved paleoslope or deep shelf environment along the basin margin (Hassler et al., 2019). The presence of quartzo-feldspathic detritus and fine quartzose epiclastic detritus suggests a reworking history, possibly derived from older basement, whereas turbidite lenses indicate an impact-generated tsunami origin (Simonson, 1992; Hassler and Simonson, 2001; Glass and Simonson, 2013).

However, the consistency of the BGSL aggregate thicknesses of around 1-centimetre across all exposure sites with similar spherule morphologies provides evidence for directly dispersed ejecta, deposited below wase base (Simonson et al., 1993; Glass and Simonson, 2013). Evidence suggests that the BGSL was either generated by a more complex impact history, or there was a significant time gap between the meteorite impact event and spherule deposition (Glass and Simonson, 2013). The latter assumption is supported by calculations from Hassler et al. (2000), who proposed that the distance between Hamersley Basin and the impact site was about 1650 to 2000 km. Also, Hassler et al. (2000) estimated a 4.9 km projectile diameter for the BGSL impactor using a corrected version of the Melosh and Vickery (1991) equation. However, Glikson and Allen (2004) estimated a projectile diameter of 16 km based on Bee Gorge spherule sizes, which is about three-times larger than the estimation of Hassler et al. (2000). Johnson and Melosh (2012) estimated an impactor size ranging from 6.3 to 21 km based on spherule sizes and bed thickness, which effectively encompasses both prior estimates. The BGSL deposition age is constrained to 2541 +18/-15 Ma by Pb-Pb dating of a carbonate within the Bee Gorge member up to 70 m vertically away from the spherule unit itself (Woodhead et al.,1998), which agrees with other estimates (Table 1). This includes the age approximation between two closest dates from the tuff zircon U-Pb SHRIMP results (Simonson et al., 1993; Trendall et al., 2004; Rasmussen et al., 2005; Glass and Simonson, 2013).

4.1.2 Previous Studies of Bee Gorge Impact Spherules

The average size of impact spherules in the BGSL is 0.6 mm, with the largest at 1.7 mm in diameter (Johnson and Melosh, 2012), and carbonate cement is prevalent. According to Glass and Simonson (2013), Bee Gorge spherules exhibit similar internal textures to Dales Gorge spherules, with the notable exception of stilpnomelane, which only occurs in the Dales Gorge spherule layer. The textures of alkali feldspar crystals in Bee Gorge spherules have similarly been interpreted as representing pseudomorphs of plagioclase microlites originally crystallised in basaltic melt (Scally and Simonson; 2005; Deutsch et al., 2013; Glass and Simonson, 2013).

Alkali feldspar occupies most of the entire internal spherule structure in many BGSL feldspathic spherules (Scally and Simonson, 2005; Glass and Simonson, 2013). Randomly oriented laths and blocky alkali feldspar grains are the main habits within spherule interiors, however fibrous alkali feldspar crystals radiating internally inside spherules are also present (Scally and Simonson, 2005; Glass and Simonson, 2013). Likewise, laths-fans to fibrous shaped alkali feldspar crystals generally developed along the spherule margin and form botryoidal rims, in most cases radiating from rims inwards into the core (Scally and Simonson, 2005) (Figure 4.1) (Table 7). Former vesicles located in the central cores of spherules are often filled by grains of blocky alkali feldspar grains, quartz grains, or dolomite grains during diagenesis, and some spherules contain altered glass cores (Scally and Simonson, 2005). Fine dark inclusions in alkali feldspar laths are proposed to be titanium-bearing oxides (Scally and Simonson, 2005; Glass and Simonson, 2013;).

The Bee Gorge spherule shapes are suggested to have been largely influenced by both physical and chemical compaction, as they often exhibit long and sutured grain contacts associated with pressure solution. Some Bee Gorge spherules show compaction-related eggshell diagenesis, as proposed by Wilkinson and Landing (1978), which involves the fragmentation of spherules and partially dissolved carbonate ooids occurred during compaction. There are also other non-spherical spherules present in BGSL, such as splash forms, agglutinated particles, and truncated spherule fragments, indicating that they probably formed from collision within the ejecta cloud in flight (Glass and Simonson, 2013). Despite the lack of stilpnomelane in the BGSL, the strong similarity of both BGSL and DGSL spherule characteristics led Glass and Simonson (2013) to suggest that interpretations of DGSL origins might be extended to the BGSL.

4.2 Results: Description of Investigated Bee Gorge Spherules

Bee Gorge feldspathic microkrystite spherules were examined with both transmitted light and SEM-EBSD methods. Images collected were both used to describe the spherule and matrix mineralogy and crystal habits, and used to classify the spherule types (Table 7). Spherules analysed by EBSD are contained in epoxy mount BGSL-3, and thin section BGSL-1 (also referred as BGTS) (Table 6).

A total of 80 spherules from BGTS were documented in transmitted light. A subset of 18 were further analysed by EBSD, including 10 from BGSL-3, and 8 from BGTS (Table 7). The Bee Gorge spherule investigation prioritised textural characteristics of feldspar in the selected feldspathic spherules, including fan-like, bowtie, spherical and polygonal structures (Table 11). Orthoclase is the main mineral found in Bee Gorge feldspathic spherules. Other minerals include dolomite and quartz. The matrix groundmass of the BGSL matrix is composed of carbonates (primarily dolomite) and quartz, which is consistent with descriptions from previous studies of the Bee Gorge member as a high energy turbidite. Accessory minerals in the matrix include apatite, rutile, zircon and monazite.

4.2.1 Orthoclase

Orthoclase in Bee Gorge spherules is often light brown in PPL, in contrast with the altered glass cores, which are optically brighter. Orthoclase comprises up to 56.2% of a given spherule, as mapped by EBSD (Table 9). Orthoclase was also identified in the matrix by EBSD analysis (e.g., Figs. 4.2, 4.3A, 4.4F). The habit of matrix orthoclase contrasts texturally with the radial orthoclase crystallites within Bee Gorge spherules (Figure 4.1). Orthoclase is assumed to have pseudomorphically replaced original plagioclase during diagenesis (Simonson et al., 1993; Scally and Simonson, 2005; Glass and Simonson, 2013). Orthoclase also occurs as a diagenetic phase in the matrix, as well as blocky crystals lining filled vesicles within spherules (Figs., 4.2F, 4.5F, 4.10D).

4.2.1.1 Feldspathic Spherule Internal Textures: Radial-type and Random-type

Two main types of orthoclase crystal growth habits/patterns were observed: (1) radial-type morphologies, and (2) random-type morphologies. The two types are described in the following sections.

Spherules with Radial Microlites

Similar to Dales Gorge spherules, Bee Gorge spherules contain inwards radiating spherulitic alkali feldspar crystals that have been classified as radial-type spherules (Figure 4.2). A total of 22 of 80 (28%) Bee Gorge spherules examined in transmitted light have radial-type textures (Table 9). Of the 18 spherules mapped by EBSD, 12 of 18 (67%) are radial-types (Tables 10, 11). The average length of orthoclase spherulites in the examined BG spherules ranges from 80 to 91 µm (Fig. 4.3), with maximum length up to 140 µm (Fig 4.3A(a)).

The spherulitic microstructures involved are mainly (a) fan-like structures, forming inwards-radiating botryoidal-to-acicular fans from spherule surfaces; and (b) spherical structures. The latter indicates a relatively higher degree of supercooling (Lofgren 1971, 1974). A spherical spherulitic texture is observed in the top right corner of spherule BGTS-S73 (Fig. 4.2B). Bowtie spherulites and polygonal structures are also observed in EBSD images of Bee Gorge spherules. A conspicuous polygonal structure is visible in transmitted light that is clearly not isotropic, yet it did not yield diffraction patterns during EBSD analysis (Fig. 4.2D-F).

Some Bee Gorge radial-type spherules preserved an apparent ‘double rim’ feature. For instance, Bee Gorge spherule S1 appears to consist of two concentric bands of feldspar microlites (Figure 4.5A, B), both surrounding a central vesicle filled with quartz. The double rim microstructure is easily distinguished optically, as the two concentric bands of radial microlites are divided by a conspicuous dark brown ring (Fig. 4.5A). EBSD analysis resolved each of the radial feldspar rings, and also documented a non-crystalline region separating them (Fig. 4.5D-F).

Spherules with Random Microlites

Random-type spherules principally contain orthoclase grains of various lengths, forming prismatic to equant or tabular crystallites. A total of 12 of 80 (15%) Bee Gorge spherules examined in transmitted light have random-type textures (Table 9). Of the 18 spherules mapped by EBSD, 6 of 18 (33%) are random-type (Table 10, 11). The average length of orthoclase grains ranges from 9.8 to 12.9 μm (shorter grains) (Fig. 4.5, 4.6), with maximum length up to 200 μm (longer grains) (Fig 4.6B(b)). In Bee Gorge spherule S14 (Fig. 4.7B), nucleation of a seemingly spherical spherulitic microstructure is unique amongst the random-type spherule population. This might indicate an unusual growth condition of BGSL-3_S14, perhaps suggesting a mixture origin in a vapor plume (see Section 5.4).

4.2.2 Apatite

Apatite is the main accessory mineral found within Bee Gorge spherules. It appears as a bright phase in BSE images (Fig. 4.2C, 4.4C, 4.5C). In EBSD maps, apatite comprises up to 1.8% of the spherule (Table 10). Apatite grains are typically small and equant, and occur along the boundaries of segmented alkali feldspar grains (Figs. 4.5D, 4.8D, 4.9D).

4.2.3 Dolomite and Quartz

Quartz and dolomite are the main matrix phases in the Bee Gorge spherule layer. Fine-grained and rounded quartz grains originated as high-energy chert-turbidite materials. Phase maps of quartz allow the circular (or near circular) outlines of spherules to be readily visualised and distinguished from the matrix (Figs. 4.8B, 4.9B, 4.10D). In some maps, quartz in the matrix appears to define layering that is deflected around spherules (Fig. 4.9B). Quartz also occurs as a vesicle filling in some radial-type spherules (Figs. 4.2D, 4.5D). Dolomite appears to have precipitated after quartz, because dolomite rhombs occur throughout the matrix, and, unlike quartz, they protrude into spherule margins (Fig. 4.10D). In some spherules dolomite also defines layers that are interbedded with quartz (Fig. 4.9C), and it can also occur as a vesicle filling in radial-type spherules with vesicles (Fig. 4.9C).

4.3 Discussion

4.3.1 Classification of Bee Gorge Spherules

Scally and Simonson (2005) described six categories of Wittenoom spherules (later redefined with Bee Gorge and Paraburdoo spherules) based on features observed in transmitted light images (Table 8). In general, Bee Gorge spherules share many textural and mineralogical similarities with Dales Gorge spherules (e.g., Krull-Davatzes et al., 2015) (Tables 9, 10). The dominant mineral is orthoclase with acicular crystal morphologies, and also with spherulitic cooling textures such as fans, bowties, and polygonal structures. Many radial-type spherules contain former glass cores and vesicles. As previous studies on Bee Gorge spherules were also focused on transmitted light microscopy, a more refined classification of Bee Gorge spherules is provided in this study based on a combination of transmitted light images, BSE and FSE images, and EBSD mapping (Table 11). In summary, Bee Gorge feldspathic microkrystite spherules were classified accordingly into the same two categories as Dales Gorge feldspathic microkrystites, namely, radial-types and random-types.

4.3.2 Orthoclase as a Pseudomorph After Plagioclase, and Associated Apatite Inclusions

The Bee Gorge spherules are described as having been heavily reworked during deposition, and they have also been diagenetically altered by fluids (Simonson et al., 1993; Hassler and Simonson, 2001; Glass and Simonson, 2013). Although apatite grains were found in the BGSL matrix groundmass, the presence of apatite within spherules is restricted to areas of segmented or porous polycrystalline alkali feldspar grains. Apatite is a minor component within Bee Gorge spherules, yet, it may be potentially significant in relation to the pseudomorphic replacement of plagioclase. The crystallisation of apatite, one of the only Ca-bearing phases within Bee Gorge spherules, may have been facilitated by alteration of original Ca-bearing igneous minerals, such as calcic plagioclase or calcic-clinopyroxene (Lofgren, 1974; Putnis et al., 2007; Plümper and Putnis, 2009). According to Putnis et al. (2007) and Plümper and Putnis (2009), segmentation or porosity of orthoclase pseudomorphs after plagioclase can be explained by sub-solidus mineral–rock-fluid replacement processes, such as dissolution-reprecipitation. It is therefore possible that apatite may have formed and intergrown within segmented orthoclase grains during replacement of plagioclase, as it would have provided an opportunity to scavenge Ca necessary for apatite stability. We note that it is also possible that the source of Ca for the apatite inclusions might have been diagenetic fluids and/or been related to precipitation of diagenetic carbonates.

4.3.3 Formation of Bee Gorge Spherules as Silica-Rich Melt Droplets

Two different types of feldspathic microkrystites were documented in Bee Gorge spherule layer: radial-type spherules, and random-type spherules. The two types are similar to those found in the Dales Gorge spherules (Section 3.3). The presence of spherulitic textures in radial-type spherules indicates rapid crystal growth (e.g., fans, bowties), and they were likely formed during rapid quenching related to various degree of supercooling (quench rates) of the vapor-condensed impact melts (Lofgren, 1974; Zheng et al., 2018). The feldspar crystallites are assumed to have initially nucleated from the external spherule margins. Dust rims, which may have triggered nucleation of crystallites, were not observed on Bee Gorge spherules, perhaps due to their reworking history. Alternatively, the absence of dust rims might also indicate that impinging dust was not the main trigger for feldspar nucleation.

The polygonal structures observed in the cores of some Bee Gorge spherules with formerly glassy cores is attributed to the partial crystallisation and incomplete quench history of the spherule. For example, Bee Gorge spherule S18 crystallised feldspar microlites at the spherule margin prior to quenching (Fig. 4.4A, F). Quenching prevented the radial feldspar fans from growing further inward, which led to development of polygonal structure in the bright core (Fig. 4.4A, B). The core region is thus interpreted to represent former glass that partially devitrified (altered). The origin of the ‘double rim’ structure preserved in Bee Gorge spherule S1 is unknown (Fig. 4.5). However, it may record the initial formation of a microkrystite, which was then enveloped by a second melt coating. Alternatively, an existing microkrystite may have developed a dust rim that was subsequently re-melted, forming the outer-most radial rim.

Chapter 5 Origin of Precambrian Impact Spherules from the Pilbara

The EBSD investigation of impact spherules from Dales Gorge and Bee Gorge in this study enables the crystallisation and diagenetic histories of the feldspathic microkrystites to be revealed in more detail than prior studies. As EBSD analysis provides quantitative information and the ability to resolve crystal morphologies and various microstructures of alkali feldspar and other phases in the spherules, new insights on the primary formation mechanisms of the feldspathic microkrystites is available. It is important to acknowledge inherent limitations of the study, as it is difficult to fully explain spherule occurrences based on observations from thin sections of diagenetically altered samples. One of the limitations of this study and the simplified model is that this investigation is purely based on internal crystallisation textures. Any potential variation in the initial impact melt composition is a factor that could have influenced the initial crystallisation of microlites, and this factor could not be evaluated in this study, given the heavily altered state of the spherules. There are also other aspects that could be considered, such as any potential re-heating/re-melting events associated with atmospheric re-entry, and the potential for thermal devitrification of spherules within the vapor cloud, before atmospheric re-entry. Both of these latter two processes could potentially influence microlite formation.

5.1 Similarities and Differences Between Dales Gorge and Bee Gorge Spherules

5.1.1 Similarities Among the Spherule Suites

Similar textural characteristics were observed between the Dales Gorge and Bee Gorge feldspathic microkrystites (e.g., quench textures), which indicates that they may share a similar origin or formation processes. Spherulitic textures were observed in both spherule suites, which indicates rapid crystallisation and/or cooling of the impact spherules occurred after they condensed. Similar textures were reported by Lofgren (1974) and Zheng et al. (2018) (Fig. 5.1 and 5.2). Both of the studied spherule suites have been classified into two categories based on their alkali feldspar (orthoclase) crystal habits, with or without the presence of vesicles. The radial-type spherule population contains spherulitic textures such as spherical, bowtie, and fan-like microstructures, which experimentally form as a consequence of a higher degree of supercooling. The random-type spherule population is proposed to have crystallised more slowly, in a relatively hotter region, with a lower degree of supercooling compared to radial-type spherules.

The investigated feldspathic spherules are assumed to have formed as primary microkrystites, as they contain microlites/crystallites (see Section 1.1). However, this remains an interpretation, as they also may have initially formed by ejection of ballistic glass (silica-rich melt without crystals). In this alternative scenario, microlite growth is hypothesised to have been initiated during the atmosphere re-entry, rather than as a vapor condensate. Yet, the only confirmed example of distal impact ejecta glass that has experienced heating from atmosphere re-entry are the flange-type Australasian tektites (Pillans et al., 2012), which do not contain microlites. Therefore, we view a ballistically emplaced melt origin as unlikely for the Archean spherules, and will continue to classify them as microkrystites.

5.1.2 Differences in the Studied Spherules

The lithological host or matrix composition of the Dales Gorge (BIF-shale) and Bee Gorge (turbidite) spherule suites are quite different, as the former contains stilpnomelane and siderite, and the latter contains dolomite and quartz. The mineralogical differences signify the different depositional environments of these spherule layers, which led to formation of different diagenetic phases. For instance, the mineral assemblage for the DGSL consists of stilpnomelane-alkali feldspar-ilmenite-siderite, which is characteristic of ferruginous shale formed in a deep marine paleoenvironment. In contrast, the mineral assemblage for the BGSL consists of dolomite-quartz-alkali feldspar-apatite, an argillite-siliciclastic assemblage reflecting a relatively high energy deposit.

5.2 Evidence for Igneous (Primary) and Diagenetic (Secondary) Minerals

The investigated impact spherules have both been profoundly affected by diagenetic processes post-deposition, associated with various fluid compositions. Diagenesis likely triggered the pseudomorphic replacement of primary crystallites within the spherules. Such origins are suggested for orthoclase, and perhaps other minerals found within spherules.

5.2.1 Plagioclase Replacement History Related to Alkali Feldspar

Orthoclase is considered to have formed as a result of interaction with potassic-fluids sourced from deep marine sediments (i.e., shale) and detrital alkali feldspar. A similar origin is attributed to other authigenic phases (e.g., stilpnomelane, sulphides, carbonates) (Sweeney and Simonson, 2008; Glass and Simonson, 2013). The effects of potassic fluids are prevalent in Bee Gorge spherules BGTS-S73 (Fig. 4.2) and BGTS-S29 (Fig. 4.10). The vesicle walls of these spherules contain blocky alkali feldspar grains, which differ in shape from the spherulitic and quenched textures that form exclusively within spherules. Furthermore, Belza et al. (2017) also proposed that orthoclase may be a primary crystallising phase in Chicxulub impact spherules.

The suggestion that orthoclase is a pseudomorph after primary plagioclase is based principally on the primary microstructures of orthoclase within spherules, as they have strong textural similarities with experimental plagioclase quench textures in basalt (Lofgren, 1974). According to Lofgren (1974) and Zheng et al. (2018), quench textures are both temperature and composition-dependant, both of which control the grain size and complexity of the quench crystal shapes. Coarser quench products are usually subjected to longer durations of crystal growth and/or lower degrees of supercooling. Equant to tabular crystals experimentally form at the lowest degree of supercooling, followed by prismatic crystals (Lofgren, 1974).

A progression of spherulite types form during crystallisation as the degree of supercooling increases: from fan-like, to spherical, to bowtie microstructures (depending on open or fine spherulitic growth), to axiolitic fibres (not studied) (Lofgren, 1974). According to the experimental results of Lofgren (1971, 1974), quench spherulites, including bowties, fans, and spherical textures, can form at supercooling temperatures (ΔT) ranging from 70 °C up to 430 °C, depending on the initial melt composition. In contrast, the simpler quench textures such as tabular to prismatic structures form at lower degrees of supercooling, with ΔT ~0-30 °C and ΔT ~20-70 °C, respectively. However, there are always complications in reality to clarify all the quench textural growth conditions (e.g., composition of vapor plume).

5.2.2 Origin of Ilmenite

The occurrence of ilmenite in Dales Gorge microkrystites has been previously considered as a secondary phase formed during diagenesis, based on transmitted light and SEM observations (Glikson and Allen, 2004; Sweeney and Simonson, 2008; Glass and Simonson, 2013). However, based on this EBSD investigation of ilmenite, the occurrences of ilmenite within impact spherules are here interpreted as a primary occurrence (e.g., vapor plume product), rather than as a product of diagenesis. Perhaps the best evidence for a primary origin of ilmenite is the external ring of ilmenite found in Dales Gorge spherule S32 (Fig. 3.16). Spherule 32 (DGTS-S32) is a merged spherule, whereby one spherule agglutinated with another, partially encapsulating it, presumably in a molten state (Fig. 3.16A, D, F). Ilmenite lines the exterior surface of the encapsulated spherule, and is thus found preserved inside the merged spherule. Such ilmenite textural occurrences do not form on the exterior surface of broken spherules or other objects elsewhere in the same layer, and uniquely identify a primary origin for ilmenite.

As for the occurrence of elongate ilmenite arrays (e.g., Figs. 3.11, 3.12), one explanation is that they may represent exsolution products, and that their conspicuous SPO was controlled by a hosting mineral, as ilmenite exsolution is common in clinopyroxene, magnetite, and olivine (Section 3.3.3). These mafic minerals are consistent with a primary basaltic composition of the original Dales Gorge melt droplets. An exsolution origin for ilmenite was described by Bian et al. (2021), who inferred that nanometre-scale ilmenite formed by exsolution from magnetite inclusions in plagioclase (Fig. 3.14). Even though an exsolution origin of ilmenite in Dales Gorge spherules is possible, there is a significant difference in scale between the exsolved ilmenite arrays observed by Bian et al. (2021) (nanometre) and the ilmenite arrays reported in this study (micrometre). It is also the case that there is no morphological evidence in the DGSL for the presence of mafic phases that may have originally exsolved the ilmenite arrays.

5.2.3 Secondary Phases

Other secondary minerals found in this study include stilpnomelane (DGSL), carbonates (siderite in DGSL; dolomite in BGSL), quartz and apatite. Stilpnomelane occurs as a matrix component, where its origin is believed to be diagenetic cement, with attributions from volcanic ash, which may or may not be associated with the impact event. The presence of carbonates, including siderite and dolomite, in Dales Gorge and Bee Gorge spherule layers respectively, are also diagenetic cements, and occur in the matrix accordingly with their sedimentary origins. They form anhedral to euhedral carbonate rhombs that overprint and protrude into spherule margins, and they also have filled in some vesicles (Fig. 4.9). Similarly, quartz occurs as both a detrital phase and as diagenetic cement in the BGSL, either as fine-grained and rounded quartz in the matrix groundmass, or as a vesicle filling (Fig. 4.5). The latter often occur after the influence of carbonate fluids. Also, the presence of apatite inclusions within Bee Gorge spherules may record the diagenetic replacement of plagioclase.

5.3 Significance of Dust Rims on Dales Gorge Spherules

The recognition of dust rims along spherule margins in this study by EBSD analysis (Fig. 3.9) is a crucial discovery that provides new insight into spherule formation mechanisms. Prior investigations have alluded to the presence of dust coatings as the trigger of crystallite nucleation from spherule margins, but they have not previously been resolved in natural samples. Connolly and Hewins (1995) conducted experiments to characterise chondrule crystallisation textures caused by impinging mineral dust at the contact of molten droplets. Their experiments showed that with a cooling rate at 500 °C/hour and quenched from 1000 °C (Connolly and Hewins, 1995), the effects of introducing dust produced a large variety of spherulitic crystals with similar textures to those described in Lofgren (1974). Dust rims on chondrules have been referred to as fine-grained dust rims (FGRs) (Cuzzi, 2004; Xiang et al., 2019, 2021). The role of dust in the crystallisation of impact spherules was also mentioned by Belza et al. (2017) to explain crystal habits and shapes documented in Chicxulub impact spherules. While these authors did not document the presence of dust particles on spherules, in their model, the spherules formed from the Chicxulub vapor plume encountered clouds of dust-sized particles as they condensed. The dust is inferred to have triggered nucleation of the initially glassy spherules during flight. In the case of dust rims on DG spherules, the mechanism by which dust triggers spherule crystallisation are not well known. We propose that there are thermal conditions where molten spherules could be too hot for dust to adhere to, whereby dust particles would melt directly into the impact melt, and not produce a dust coating at the spherule margin. It is also possible that some spherules may cool rapidly, and thus be too cold for dust to adhere to the surface, which also would not produce a dust rim. We envision that there exists a semi-molten condition of the spherule in an optimal thermal state (a so-called goldilocks temperature), whereby dust particles adhere to the warm spherule margins, thus forming the dust rims documented in this study. Further characterizing the details of the hypothesised goldilocks temperature are beyond the scope of this study.

5.4 A Vapor Plume Model for the Origin of Pilbara Impact Spherules

The microstructural results of this study, which cover a wide variety of feldspathic impact spherules, or microkrystites, were used to refine a simplified vapor plume model. We note the presence of other impact particles in the studied spherule deposits, which were not described here, as they are not relevant to the main purpose of this study on feldspathic microkrystites. The vapor cloud (plume) dynamics are adapted from previously proposed models (Figs. 5.3 and 5.4). The comparison of two recent vapor plume models is essential, which include (1) Johnson and Melosh (2012) (Fig. 5.4) numerical modelling of spherule nucleation-growth in an expanding vapor plume model with the ANEOS equation of state for silica, and (2) a conceptual vapor plume model for Chicxulub spherules by Belza et al. (2017), that features crystal nucleation within spherules as a function of temperature, supercooling, and dust concentration (Fig. 5.3).

The vapor plume model presented here (Fig. 5.5) attempts to take into account all of the main observations made by transmitted light microscopy and SEM-EBSD analysis of feldspathic microkrystite spherules from this study. The description for spherule types below is similar to the discussions in Krull-Davatzes et al. (2006), which relate to the the South African S3 spherule bed, and further reflects the compositional evolution of the vapor plume. Examples of spherules from both the DGSL and the BGSL were selected to best illustrate key textures interpreted to form as a function of differences in temperature due to a thermal gradient as the vapor plume expands. The model features regions in the vapor plume where dust-sized particles are interpreted to have been present, and that are attributed to the nucleation of some radial-type spherules. The presence of vesicles in many spherules records the former presence of volatiles. The source of the volatiles may be from either the target rocks, seawater, or a mixture of both.

Type A feldspathic microkrystites consist only of random-type spherules, and are considered to have condensed in the central area of vapor plume (Fig. 5.5). The random-type spherules are interpreted to form under conditions of relatively slow cooling rates (low crystal growth rate), high nucleation rate, and without impinging dust. They are thought to form in a relatively hot region and hence have had more time to crystallise internally; crystal lengths in a given random-type spherule vary as a function of duration of crystallisation and formation temperature. Principally, the hottest zone in a vapor plume will be above the centre of the impact, which is where random-type microkrystites with prismatic crystals (Type A in Fig. 5.5) are here proposed to originate.

Type B feldspathic microkrystites consist only of random-type spherules, and are proposed to form in the adjacent intermediate (or warm) region of the vapor plume, where shorter feldspar crystal sizes reflect less time to crystallise, resulting in more tabular to equant primary crystallites, with similar or slightly lower nucleation rates than Type A spherules.

Type C feldspathic microkrystites contain a mixture of both radial-type and random-type characteristics. They are interpreted to form at the boundary of the inner (warm) and outer (cool) regions of the vapor plume (Fig. 5.5).

Type D feldspathic microkrystites consist only of radial-type spherules. They are interpreted to form in the outermost regions of the vapor plume where dust particles are present (Fig. 5.5). The impingement of dust on the margin of some Type D feldspathic microkrystites is interpreted to be the primary trigger for nucleation of inward-radiating acicular feldspar crystals. Spherulitic textures subsequently formed during quenching or supercooling, as the spherules were transported further outward from the vapor plume. Direct evidence for the presence of dust rims on impact spherules was documented for the first time in this study (Figs. 3.9, 3.17, 3.18). It is proposed that dust rims are likely to be more common on impact spherules (e.g., Belza et al., 2017), but have yet to be recognised due the difficulty of resolving dust rims in transmitted light images (Fig. 3.9A). The results of this study show that EBSD is a particularly effective means of resolving dust rims. While speculative, it is also possible that some radial-type microkrystites may not preserve dust rims due to either (a) subsequent re-heating/melting events in the vapor plume (Fig. 3.16), or due to either sedimentary reworking or diagenetic processes. It is also possible that the absence of dust rims may imply that crystallisation of some radial-type spherules did not involve impinging dust.

Type E feldspathic microkrystites consist only of radial-type spherules. They are similar to Type D microkrystites, but these only partially crystallised due to quenching triggered by the largest degree of supercooling. As a consequence, Type E microkrystites have rims of inward radiating acicular feldspars surrounding cores that were formerly quenched impact glass that is now altered. Type E microkrystites are interpreted to represent formation at the outermost margin of the vapor plume, where dust triggered nucleation of radial feldspar on spherule margins prior to quenching (Fig. 5.5). An alternative model for type E spherules is they may have quenched more rapidly that other spherules due to having a different initial melt composition (e.g., one higher in silica). In this scenario, they need not necessarily have formed at the outermost margin of the vapor plume. However, all of the studied spherules have been completely diagenetic altered, so detection of differences in primary melt composition is effectively impossible.

References

Angerer, T., & Hagemann, S. G. (2010). The BIF-Hosted High-Grade Iron Ore Deposits in the Archean Koolyanobbing Greenstone Belt, Western Australia: Structural Control on Synorogenic- and Weathering-Related Magnetite-, Hematite-, and Goethite-rich Iron Ore. *Economic Geology*, *105*(5), 917–945. https://doi.org/10.2113/gsecongeo.105.5.917.

Belza, J., Goderis, S., Montanari, A., Vanhaecke, F., & Claeys, P. (2017). Petrography and geochemistry of distal spherules from the K–Pg boundary in the Umbria–Marche region (Italy) and their origin as fractional condensates and melts in the Chicxulub impact plume. *Geochimica et Cosmochimica Acta*, *202*, 231–263. https://doi.org/10.1016/j.gca.2016.12.018.

Bian, G., Ageeva, O., Rečnik, A., Habler, G., & Abart, R. (2021). Formation pathways of oriented magnetite micro - inclusions in plagioclase from oceanic gabbro. *Contributions to Mineralogy and Petrology*, 1–21. https://doi.org/10.1007/s00410-021-01864-8.

Boyd, F. R., Nixon, P. H., & Boctor, N. Z. (1984). Rapidly crystallised garnet pyroxenite xenoliths possibly related to discrete nodules. *Contributions to Mineralogy and Petrology*, *86*(2), 119–130. https://doi.org/10.1007/BF00381839.

Clout, J. M. F. (2005). Iron formation-hosted iron ores in the Hamersley Province of Western Australia. *Australasian Institute of Mining and Metallurgy Publication Series*, *September*, 9–19.

Connolly, H. C., & Hewins, R. H. (1995). Chondrules as products of dust collisions with totally molten droplets within a dust-rich nebular environment: An experimental investigation. *Geochimica et Cosmochimica Acta*, *59*(15), 3231–3246. https://doi.org/10.1016/0016-7037(95)00207-G.

Cuzzi, J. N. (2004). Blowing in the wind: III. Accretion of dust rims by chondrule-sized particles in a turbulent protoplanetary nebula. *Icarus*, *168*(2), 484–497. https://doi.org/10.1016/j.icarus.2003.12.008.

Deutsch, A., Metzler, K., Berndt, J., & Langenhorst, F. (2013). LA-ICP-MS and textural analyses of impact spherules from the 2.54Ga Bee Gorge spherule layer, Western Australia. *Large Meteorite Impacts and Planetary Evolution V*, 3053.

Fanlo, I., Subías, I., Gervilla, F., Paniagua, A., & García, B. (2004). The composition of Co-Ni-Fe sulfarsenides, diarsenides and triarsenides from the San Juan de Plan deposit, central Pyrenees, Spain. *Canadian Mineralogist*, *42*(4), 1221–1240. https://doi.org/10.2113/gscanmin.42.4.1221.

Francis, P. E., Lyle, P., & Preston, J. (1986). A tholeiitic andesite flow unit among the Causeway Basalts of North Antrim in Northern Ireland. *Geological Magazine*, *123*(2), 105–112. https://doi.org/10.1017/S0016756800029769.

Glass, B. P. (1990). Tektites and microtektites: key facts and inferences. *Tectonophysics*, *171*(1–4), 393–404. https://doi.org/10.1016/0040-1951(90)90112-L.

Glass, Billy P., & Simonson, B. M. (2013). Distal impact ejecta layers: Spherules and more. *Elements*, *8*(1), 43–48. https://doi.org/10.2113/gselements.8.1.43.

Glikson, A., & Allen, C. (2004). Iridium anomalies and fractionated siderophile element patterns in impact ejecta, Brockman Iron Formation, Hamersley Basin, Western Australia: Evidence for a major asteroid impact in simatic crustal regions of the early Proterozoic earth. *Earth and Planetary Science Letters*, *220*(3–4), 247–264. https://doi.org/10.1016/S0012-821X(04)00062-7.

Glikson, A. Y., & Vickers, J. (2010). Asteroid impact connections of crustal evolution. *Australian Journal of Earth Sciences*, *57*(1), 79–95. https://doi.org/10.1080/08120090903416211.

Glikson, Andrew Y. (2005). Geochemical and isotopic signatures of Archaean to Palaeoproterozoic extraterrestrial impact ejecta/fallout units. *Australian Journal of Earth Sciences*, *52*(4–5), 785–798. https://doi.org/10.1080/08120090500170328.

Glikson, Andrew Y. (2004). Early Precambrian Asteroid Impact-Triggered Tsunami: Excavated Seabed, Debris Flows, Exotic Boulders, and Turbulence Features Associated with 3.47–2.47 Ga-Old Asteroid Impact Fallout Units, Pilbara Craton, Western Australia. *Astrobiology*, *4*(1), 1-32.

Graf, D. L. (1961). Crystallographic tables for the rhombohedral carbonates. *American Mineralogist*, *46*, 1283–1316.

Hassler S. W. 1993. Depositional history of the Main Tuff Interval of the Wittenoom Formation, late Archean-early Proterozoic Hamersley Group, Western Australia. *Precambrian Research, 60,* 337–359.

Hassler, S. W., Robey, H. F., Simonson, B. M. (2000). Bedforms produced by impact-generated tsunami, ~2.6 Ga Hamersley basin, Western Australia. *Sedimentary Geology, 135,* 283–294.

Hassler, S. W., & Simonson, B. M. (2001). The Sedimentary Record of Extraterrestrial Impacts in Deep - Shelf Environments : Evidence from the Early Precambrian. *The Journal of Geology*, *109*(1), 1–19.

Hassler, S. W., Simonson, B. M., & Sumner. D. (2011). Paraburdoo spherule layer (Hamersley Basin, Western Australia): Distal ejecta from a fourth large impact near the Archean-Proterozoic boundary. *Geology, 39*(4), 307-310. doi: 10.1130/G31526.1.

Hassler, S. W., Biller, S., & Simonson, B. M. (2019). Petrography and sedimentology of the ~2490 Ma DS4 impact spherule layer revisited, Brockman Iron Formation (Hamersley Group, Western Australia). *Meteoritics and Planetary Science*, *54*(10), 2241–2253. https://doi.org/10.1111/maps.13223.

Haugaard, R., Pecoits, E., Lalonde, S., Rouxel, O., & Konhauser, K. (2016). The Joffre banded iron formation, Hamersley Group, Western Australia: Assessing the palaeoenvironment through detailed petrology and chemostratigraphy. *Precambrian Research, 273,* 12–37. https://doi.org/10.1016/j.precamres.2015.10.024

Hughes, J. M., Cameron, M., & Mariano, A. N. (1991). The therapeutic effect of interventional heated - Lipiodol perfusion combined with heated - Lipiodol injection into tumor for the treatment of VX2 liver cancer in experimental rabbits. *American Mineralogist*, *76*, 1165–1173. https://doi.org/0003{04xl9 r /0708-l l 65$02.0.

Jiang, C. Z. & Tosca, N. J. (2019). Fe (II)-carbonate precipitation kinetics and the chemistry of anoxic ferruginous seawater. *Earth and Planetary Science Letters, 506,* 231-242. https://doi.org/10.1016/j.epsl.2018.11.010.

Johnson, B. C., & Melosh, H. J. (2012). Formation of spherules in impact produced vapor plumes. *Icarus*, *217*(1), 416–430. https://doi.org/10.1016/j.icarus.2011.11.020.

Krull-Davatzes, A., Lowe, D., & Byerly, G. (2006). Compositional grading in an ∼3.24 Ga impact-produced spherule bed, Barberton greenstone belt, South Africa: A key to impact plume evolution. *South African Journal of Geology, 109*(1-2), 233-244. https://doi.org/10.2113/gssajg.109.1-2.233

Krull-Davatzes, A., Swartz, N., & Enos, M. (2015). Petrologic and impact size controls on Precambrian spherule diameters. *The Geological Society of America Special Paper 518* (07), 115–125. https://doi.org/10.1130/2015.2518(07).

Lascelles, D. F. (2006). The genesis of the hope downs iron ore deposit, Hamersley Province, Western Australia. *Economic Geology, 101*(7), 1359–1376. https://doi.org/10.2113/gsecongeo.101.7.1359.

Leinenweber, K., Navrotsky, A., & Parisc, J. B. (1995). *PhysChemMinerals-22(1995)251-High-pressure perovskites on the join CaTiO3-FeTiO3.pdf*. 251–258. https://link.springer.com/article/10.1007/BF00202258#citeas.

Lim, C. E. (2020). *Significance of Reddening in BIF Towards Genesis of Bedded Iron Ore Mineralisation in Hamersley Province, WA* (Unpublished Honours Dissertation, Curtin University).

Lofgren, G. (1974). An experimental study of plagioclase crystal morphology; isothermal crystallisation. *American Journal of Science, 274*(3), 243–273. https://doi.org/10.2475/ajs.274.3.243.

Lofgren, Gary. (1971). Spherulitic textures in glassy and crystalline rocks. *Journal of Geophysical Research*, *76*(23), 5635–5648. https://doi.org/10.1029/jb076i023p05635.

Massonne, H.-J., & Neuser, R. D. (2005). Ilmenite exsolution in olivine from the serpentinite body at Zöblitz, Saxonian Erzgebirge – microstructural evidence using EBSD. *Mineralogical Magazine*, *69*(2), 119–124. https://doi.org/10.1180/0026461056920239.

Melosh, H., Vickery, A. (1991). Melt droplet formation in energetic impact events. *Nature, 350*, 494–497. https://doi.org/10.1038/350494a0.

Miyano, T., & Miyano, S. (1982). Ferri-annite from the Dales Gorge member iron-formations, Wittenoom area, Western Australia. *American Mineralogist*, *67*(11–12), 1179–1194.

Miyano, Takashi. (1982). Canadian Mineralogist Vol. 20, w. 189-202 (1982). *Canadian Mineralogist*, *20*, 189–202.

Morris, R. C., & Kneeshaw, M. (2011). Genesis modelling for the hamersley BIF-hosted iron ores of Western Australia: A critical review. *Australian Journal of Earth Sciences, 58*(5), 417–451. https://doi.org/10.1080/08120099.2011.566937.

Moseley, D. (1981). Ilmenite exsolution in olivine. *American Mineralogist*, *66*(9–10), 976–979.

Mulder T., Razin P., & Faugeres J-C. 2009. Hummocky cross-stratification-like structures in deep-sea turbidites: Upper Cretaceous Basque basins (Western Pyrenees, France). *Sedimentology*, *56*, 997–1015.

Muhling, J. R., & Rasmussen, B. (2020). Widespread deposition of greenalite to form Banded Iron Formations before the Great Oxidation Event. *Precambrian Research, 339*(September 2019), 105619. https://doi.org/10.1016/j.precamres.2020.105619.

O'Keefe, J., Ahrens, T. (1982). Impact mechanics of the Cretaceous–Tertiary extinction bolide. *Nature, 298*, 123–127. https://doi.org/10.1038/298123a0.

Petersson, A., Kemp, A. I. S., Gray, C. M., & Whitehouse, M. J. (2020). Formation of early Archean Granite-Greenstone Terranes from a globally chondritic mantle : Insights from igneous rocks of the Pilbara Craton , Western Australia. *Chemical Geology*, *551*(May), 119757. https://doi.org/10.1016/j.chemgeo.2020.119757.

Pickard, A. L., Barley, M. E., & Krapež, B. (2004). Deep-marine depositional setting of banded iron formation: Sedimentological evidence from interbedded clastic sedimentary rocks in the early Palaeoproterozoic Dales Gorge Member of Western Australia. *Sedimentary Geology, 170*(1–2), 37–62. https://doi.org/10.1016/j.sedgeo.2004.06.007.

Pillans, B., Simmonds, P., Hitchcock, W., & Alloway, B. (2012). Tektites , minitektites and microtektites from the Kalgoorlie region , Western Australia. *Australian Regolith and Clays Conference Mildura, February*, 95–98.

Plümper, O., & Putnis, A. (2009). The complex hydrothermal history of granitic rocks: Multiple feldspar replacement reactions under subsolidus conditions. *Journal of Petrology*, *50*(5), 967–987. https://doi.org/10.1093/petrology/egp028.

Prince, E., Gabrielle, D., & Martin, R. (1973). Neutron Diffraction Refinement of an ordered orthoclase Structure. *American Mineralogist*, *58*, 500–507.

Putnis, A., Hinrichs, R., Putnis, C. V., Golla-Schindler, U., & Collins, L. G. (2007). Hematite in porous red-clouded feldspars: Evidence of large-scale crustal fluid-rock interaction. *Lithos*, *95*(1–2), 10–18. https://doi.org/10.1016/j.lithos.2006.07.004.

Rasmussen, B., Blake, T. S., & Fletcher, I. R. (2005). U-Pb zircon age constraints on the Hamersley spherule beds: Evidence for a single 2.63 Ga Jeerinah-Carawine impact ejecta layer. *Geology*, *33*(9), 725–728. https://doi.org/10.1130/G21616.1.

Riller, U., Poelchau, M. H., Rae, A. S. P., Schulte, F. M., Collins, G. S., Melosh, H. J., Grieve, R. A. F., Morgan, J. V., Gulick, S. P. S., Lofi, J., Diaw, A., McCall, N., Kring, D. A., Morgan, J. V., Gulick, S. P. S., Green, S. L., Lofi, J., Chenot, E., Christeson, G. L., Fucugauchi, J. U. (2018). Rock fluidization during peak-ring formation of large impact structures. *Nature*, *562*(7728), 511–518. https://doi.org/10.1038/s41586-018-0607-z.

Scally, A., & Simonson, B. M. (2005). Spherule textures in the Neoarchaean Wittenoom impact layer, Western Australia: Consistency in diversity. *Australian Journal of Earth Sciences*, *52*(4–5), 773–783. https://doi.org/10.1080/08120090500170484.

Simonson, B. M., & Hassler, S. W. (1997). Revised correlations in the early precambrian hamersley basin based on a horizon of resedimented impact spherules. *Australian Journal of Earth Sciences*, *44*(1), 37–48. https://doi.org/10.1080/08120099708728292.

Simonson, Bruce M. (2003). Petrographic criteria for recognizing certain types of impact spherules in well-preserved precambrian successions. *Astrobiology*, *3*(1), 49–65. https://doi.org/10.1089/153110703321632417.

Simonson, Bruce M., Beukes, N. J., & Biller, S. (2018). Extending the paleogeographic range and our understanding of the Neoarchean Monteville impact spherule layer (Transvaal Supergroup, South Africa). *Meteoritics and Planetary Science*, *54*(10), 2217–2240. https://doi.org/10.1111/maps.13228.

Simonson, Bruce M., Schubel, K. A., & Hassler, S. W. (1993). Carbonate sedimentology of the early Precambrian Hamersley Group of Western Australia. *Precambrian Research*, *60*(1–4), 287–335. https://doi.org/10.1016/0301-9268(93)90052-4.

Simonson, Bruce M., Sumner, D. Y., Beukes, N. J., Johnson, S., & Gutzmer, J. (2009). Correlating multiple Neoarchean-Paleoproterozoic impact spherule layers between South Africa and Western Australia. *Precambrian Research*, *169*(1–4), 100–111. https://doi.org/10.1016/j.precamres.2008.10.016.

Simonson, Bruce M. (1992). Geological evidence for a strewn field of impact spherules in the early Precambrian Hamersley Basin of Western Australia. *Geological Society of America Bulletin,104,* 829–839.

Sweeney, D. (2002). *Impact Spherules From Western Australia : A Textural Analysis of Really Old Tiny Rocks.* (Honours Paper, Oberlin College). https://digitalcommons.oberlin.edu/honors/504

Sweeney, D., & Simonson, B. M. (2008). Textural constraints on the formation of impact spherules: A case study from the dales gorge bif, paleoproterozoic hamersley group of western Australia. *Meteoritics and Planetary Science*, *43*(12), 2073–2087. https://doi.org/10.1111/j.1945-5100.2008.tb00662.x

Taylor, D., Dalstra, H. J., Harding, A. E., Broadbent, G. C., & Barley, M. E. (2001). Genesis of high-grade hematite orebodies of the Hamersley Province, Western Australia. *Economic Geology, 96*(4), 837–873. https://doi.org/10.2113/gsecongeo.96.4.837

Thorne, W., Hagemann, S., A., W., & Clout, J. M. F. (2008). Banded Iron Formation-Related Iron Ore Deposits of the Hamersley Province, Western Australia. *Society of Economic Geologists*, 197–221.

Thorne, W. (2015). The Structural Setting and Hydrothermal Alteration of BIF-hosted High-Grade Iron Ore Deposits , the Hamersley Province , Western Australia. *The University of Western Australia.*

Thorne, A. M. & Trendall, A. F. (2001) Geology of the Fortescue Group, Pilbara Craton, Western Australia. *Geological Survey of Western Australia, Bulletin 144,* p. 249.

Timms, N. E., Pearce, M. A., Erickson, T. M., Cavosie, A. J., Rae, A. S. P., Wheeler, J., Wittmann, A., Ferrière, L., Poelchau, M. H., Tomioka, N., Collins, G. S., Gulick, S. P. S., Rasmussen, C., Morgan, J. V., Gulick, S. P. S., Morgan, J. V., Chenot, E., Christeson, G. L., Claeys, P., Yamaguchi, K. E. (2019). New shock microstructures in titanite (CaTiSiO5) from the peak ring of the Chicxulub impact structure, Mexico. *Contributions to Mineralogy and Petrology*, *174*(5). https://doi.org/10.1007/s00410-019-1565-7.

Tosca, N. J., Guggenheim, S., & Pufahl, P. K. (2016). An authigenic origin for Precambrian greenalite: Implications for iron formation and the chemistry of ancient seawater. *Bulletin of the Geological Society of America*, *128*(3–4), 511–530. https://doi.org/10.1130/B31339.1.

Trendall, A. F., & and Blockley, J. G. (1970). The iron formations of the Precambrian Hamersley Group Western Australia. *Geological Survey of Western Australia Bulletin, 119*, 391.

Trendall, A. F., Nelson, D. R., De Laeter, J. R., Hassler, S. W. (1998). Precise zircon U-Pb ages from the Marra Mamba Iron Formation and Wittenoom Formation, Hamersley Group, Western Australia. *Australian journal of earth sciences*, *45* (1), 137-142.

Trendall, A. F., Compston, W., Nelson, D. R., De Laeter, J. R., & Bennett, V. C. (2004). SHRIMP zircon ages constraining the depositional chronology of the Hamersley Group, Western Australia. *Australian Journal of Earth Sciences*, *51*(5), 621–644. https://doi.org/10.1111/j.1400-0952.2004.01082.x.

Walker, D., Powell, M. A., Lofgren, G. E., & Hays, J. F. (1978). Dynamic crystallisation of a eucrite basalt There has been a recent rebirth of interest in the production of igneous rock. *Proceedings of Lunar Science Conference, 9th*, 1369–1391.

Webb, A. D., Dickens, G. R., & Oliver, N. H. S. (2003). From banded iron-formation to iron ore: Geochemical and mineralogical constraints from across the Hamersley Province, Western Australia. *Elsevier and Chemical Geology*, *197*(1–4), 215–251. https://doi.org/10.1016/S0009-2541(02)00352-2.

Xiang, C., Carballido, A., Hanna, R. D., Matthews, L. S., & Hyde, T. W. (2019). The initial structure of chondrule dust rims I: Electrically neutral grains. *Icarus*, *321*(September 2018), 99–111. https://doi.org/10.1016/j.icarus.2018.10.014.

Xiang, C., Carballido, A., Matthews, L. S., & Hyde, T. W. (2021). The initial structure of chondrule dust rims II: Charged grains. *Icarus*, *354*(August 2020), 114053. https://doi.org/10.1016/j.icarus.2020.114053.

Zheng, H., Sun, X., Wang, J., Zhu, D., & Zhang, X. (2018). Devitrification pores and their contribution to volcanic reservoirs: A case study in the Hailar Basin, NE China. *Marine and Petroleum Geology*, *98*(2199), 718–732. https://doi.org/10.1016/j.marpetgeo.2018.09.016.

Figures and Tables

List of Figures

List of Tables

List of Figures

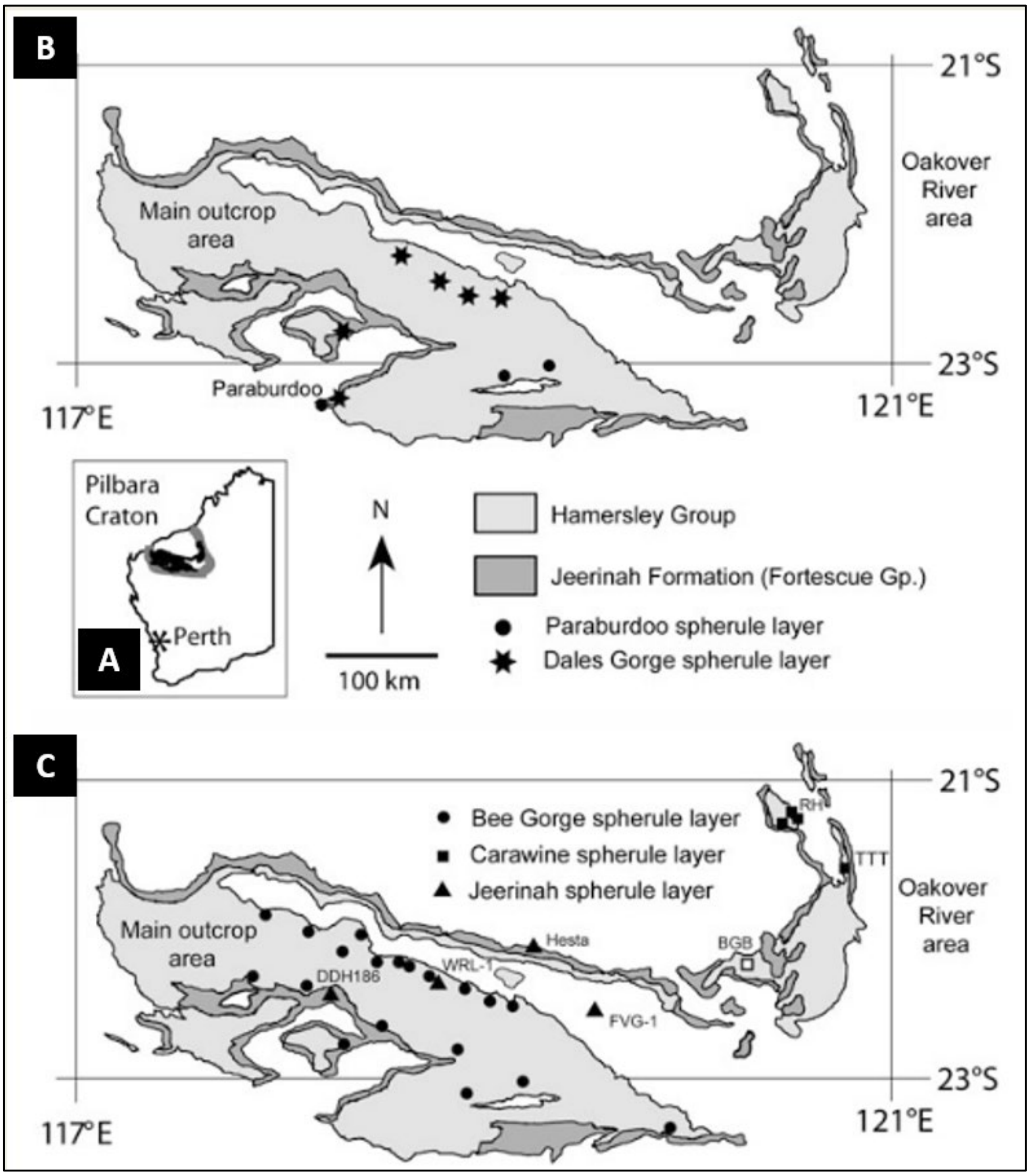

Figure 1.1: Simplified geological maps of the Hamersley Basin in Western Australia showing locations of drill cores that intersected spherule layers. (A) Index map showing the location of the Pilbara Craton in Western Australia. (B) and (C) Simplified geological maps that show the locations of sites drilled and main outcrop areas of spherule layers. Labelled sites in (C) include Ripon Hills (RH), Tarra Tarra turnoff (TTT), Hesta, FVG-1, WRL-1, DDH186, and Billygoat bore (BGB) (after Glass and Simonson, 2013).

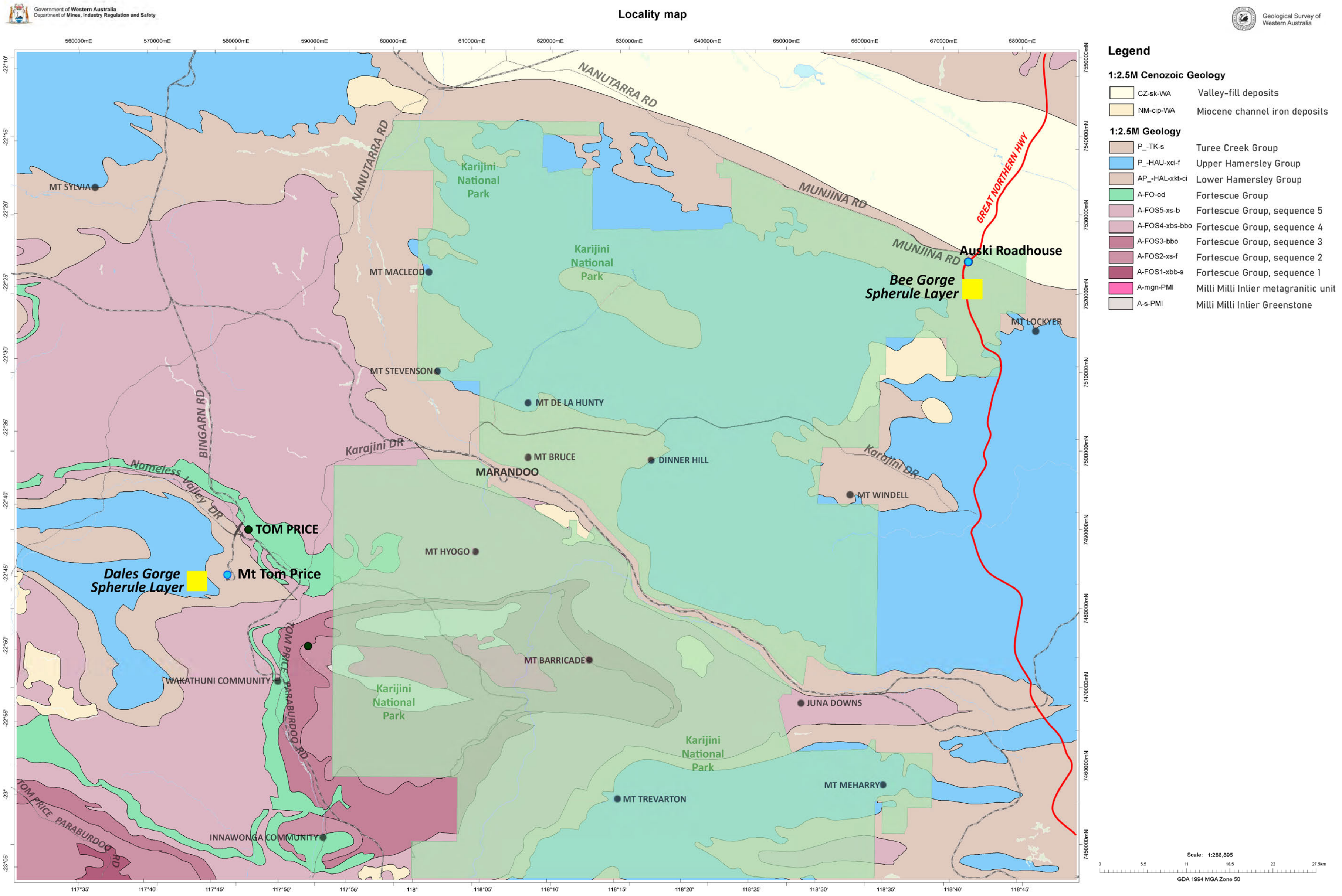

Figure 1.2: Simplified geological map showing the location of the Dales Gorge spherule layer and Bee Gorge spherule layer samples analysed in this study. The green box is marked to represent the area of Karijini National Park. The geological data were extracted from the Geological Survey of Western Australia (2022), Department of Mines, Industry Regulation and Safety. (https://geoview.dmp.wa.gov.au/geoview/?Viewer=GeoView). CC BY. The Dales Gorge spherule layer sample was identified within a core near Mount Tom Price (coordinates: GDA94, UTM Zone 50K; 575021mE, 7483441mN). The Bee Gorge spherule layer samples are from outcrop near Munjina Gorge (coordinates: GDA94, UTM Zone 50K; 673670mE, 7520950mN).

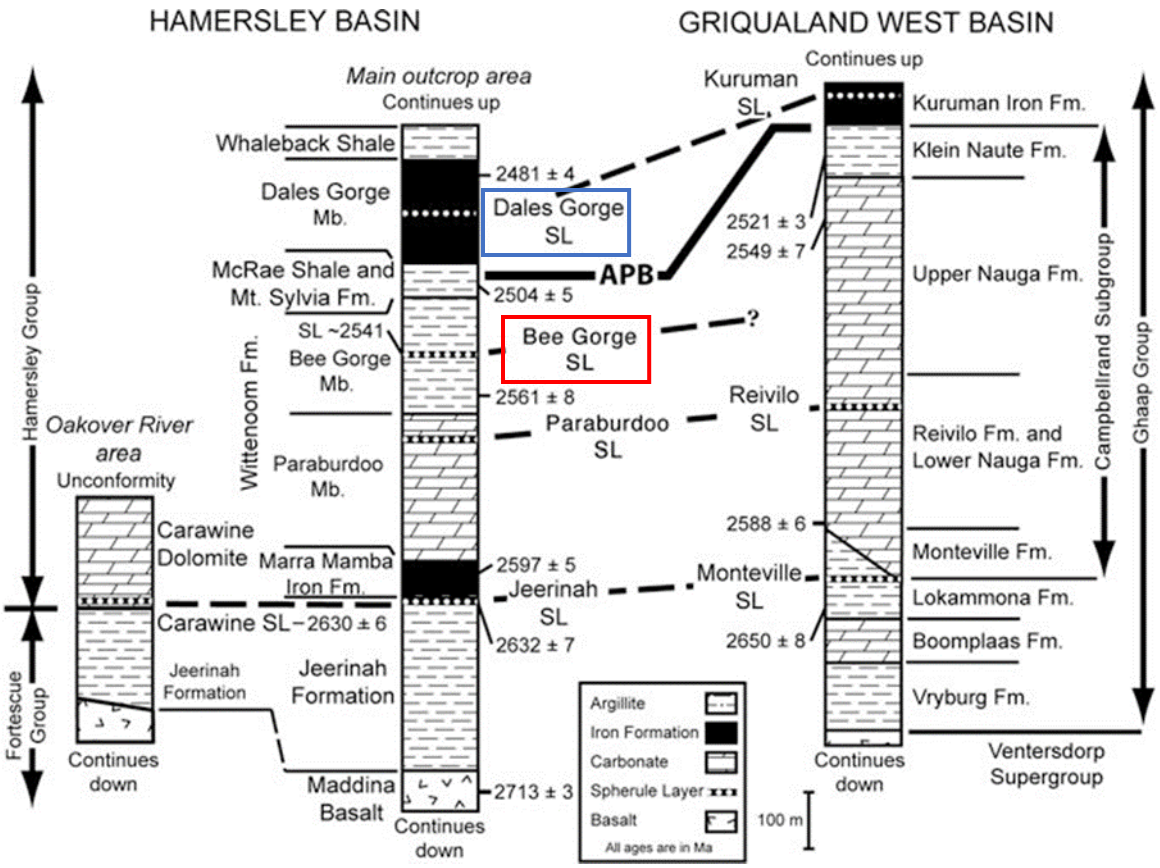

Figure 1.1 Schematic stratigraphic columns showing the Archean-Proterozoic boundary spherule layers in Western Australia. The figure shows schematic stratigraphic columns with correlative spherule layers from both the Hamersley basin (Pilbara, Western Australia) and the Griqualand West Basin (Kaapvaal, South Africa). The inferred thick black line indicates the Archean-Proterozoic Boundary (APB). The Dales Gorge spherule layer is indicated with a blue box; the Bee Gorge spherule layer is indicated with a red box. Other spherule layers are also shown (after Glass and Simonson, 2013).

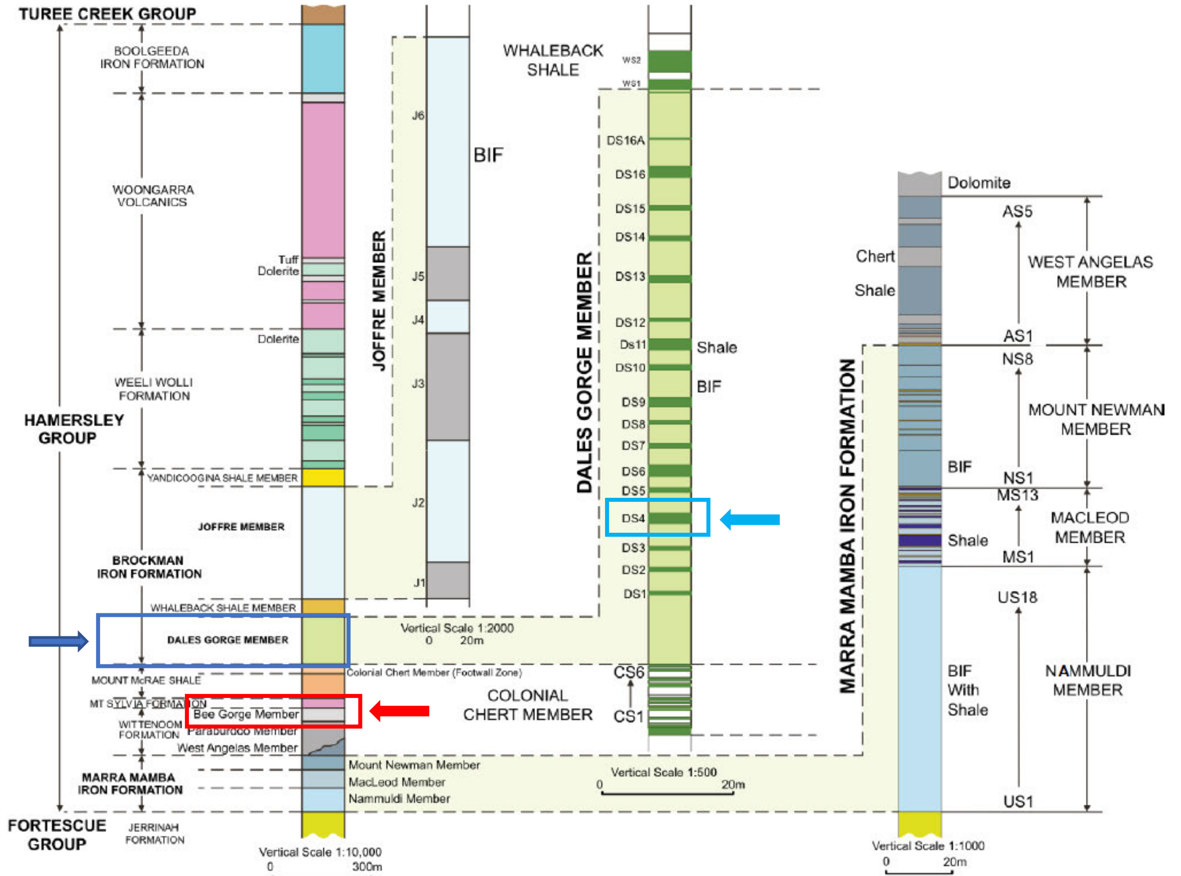

Figure 1.4: Stratigraphy of the Hamersley Group. The Dales Gorge member (dark blue box, left) hosts the Dales Gorge spherule layer in the DG4 unit (light blue box, centre) within shale-banded iron formation. The Bee Gorge member of the Wittenoom Formation (red box, left) hosts the Bee Gorge spherule layer within a dolomitic chert member (after Thorne et al., 2008).

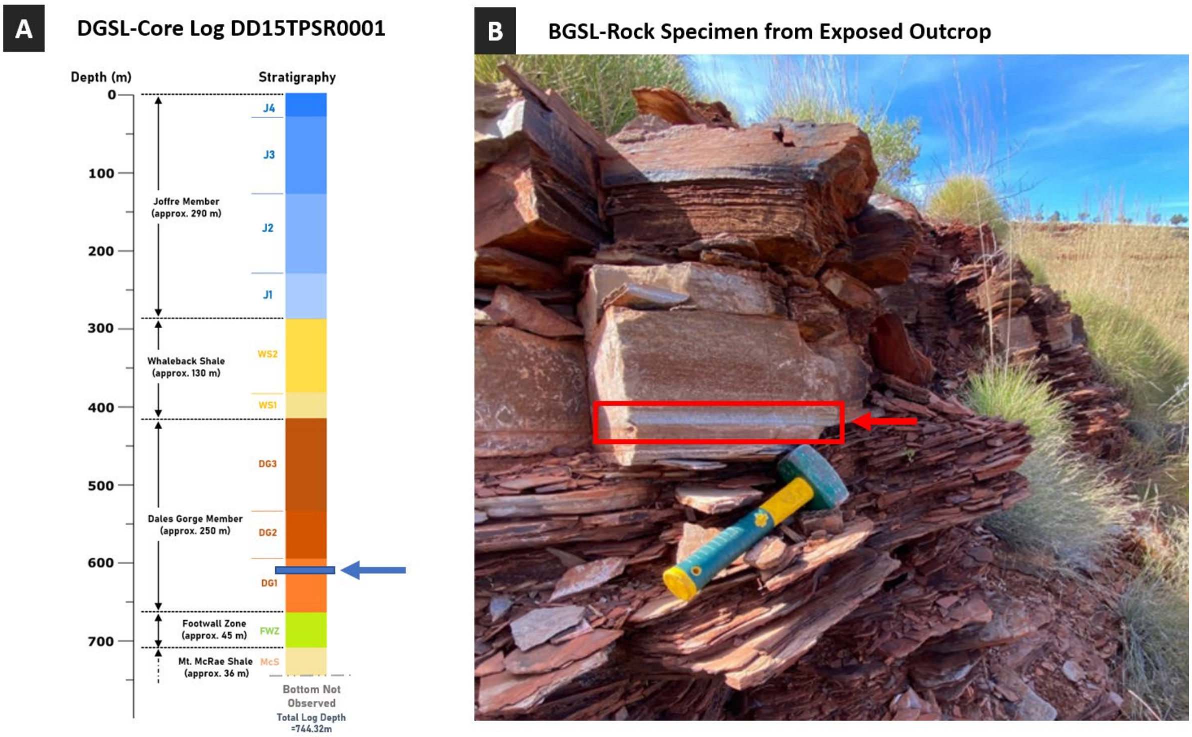

Figure 1.5: Information on samples analysed in this study. (A) Schematic log for core DD15TPSR0001, drilled at Mount Tom Price. The depth of the studied Dales Gorge spherule layer is indicated by a blue arrow. It occurs at 611 m in the DG1 unit (equivalent to DGS4 or DG4 unit in other publications). (B) Sample location of the Bee Gorge spherule layer in outcrop (white layer in red box), located approximately 3.5 km south of Auski Roadhouse, near Munjina Gorge, Karijini National Park (image credit: Raiza Quintero). Both samples were provided by Rio Tinto Exploration.

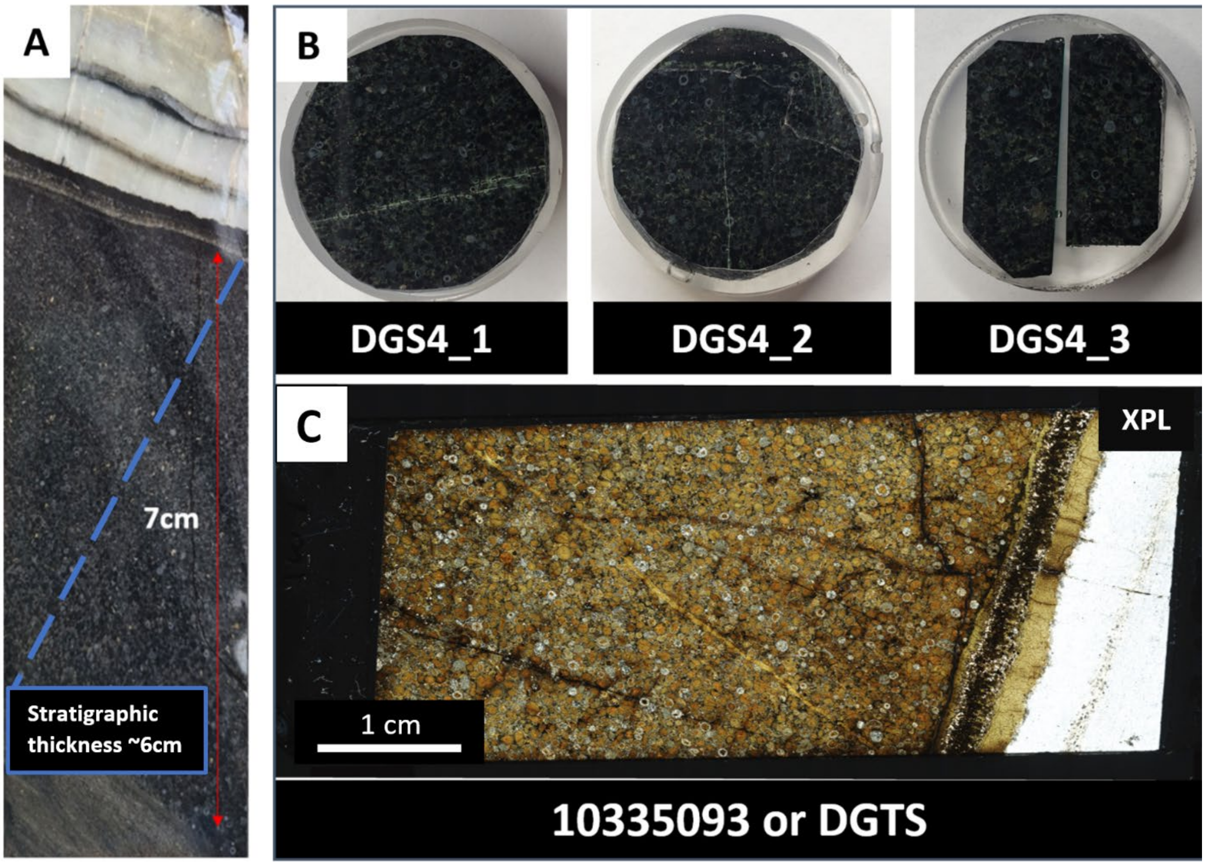

Figure 2.1: Images of the Dales Gorge spherule layer analysed in this study. (A) Section of polished rock from core DD15TPSR0001 showing the DGSL. The core thickness of the spherule layer is about 7 cm thick (red arrow); the stratigraphic thickness is approximately 6 cm thick (dashed blue line). (B) Epoxy mounts DGS4-1, DGS4-2, and DGS4-3. They are each approximately 2.54 cm across. (C) Thin section 10335093 (also referred to as DGTS) under crossed-polarised light (XPL). The bright region on the right side of the section corresponds to the top of the core image in (A).

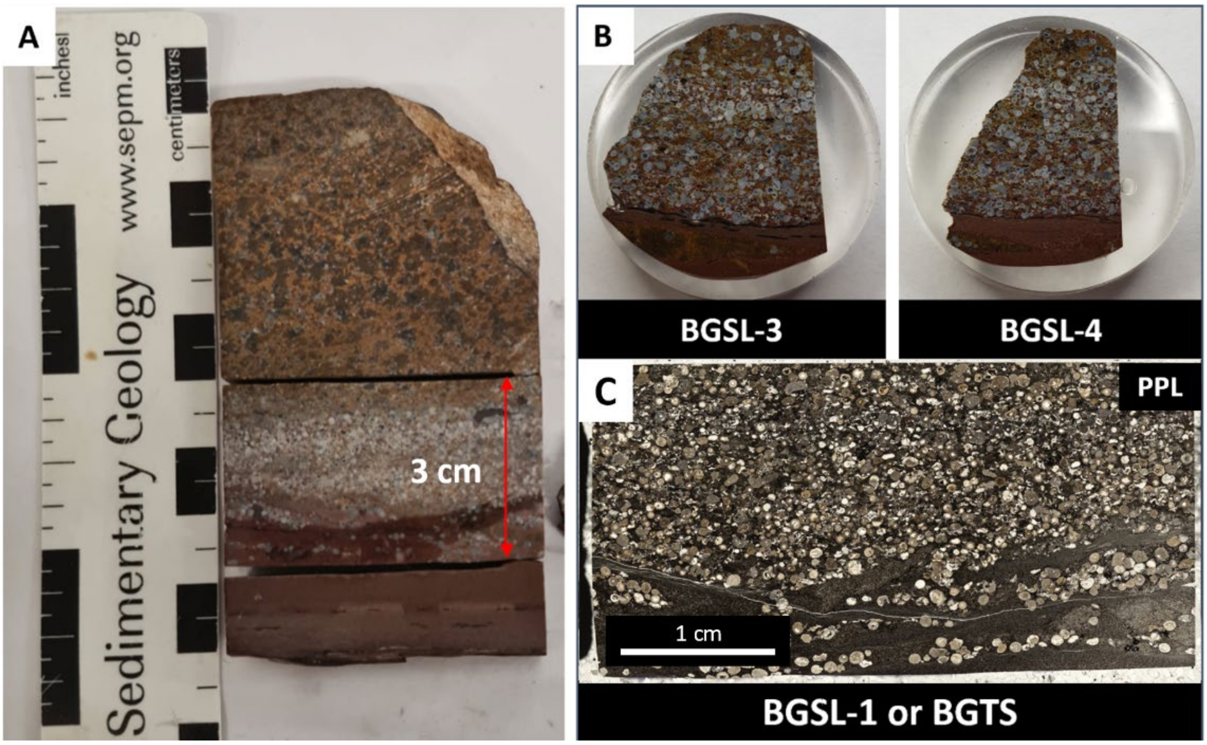

Figure 2.2: Images of the Bee Gorge spherule layer (BGSL) analysed in this study. (A) Polished slab of the Bee Gorge spherule horizon. The studied thin section block is indicated, which is about 3 cm thick (red arrow). (B) Epoxy mounts BGSL-3 and BGSL-4. They are each approximately 2.54 cm in diameter. (C) Thin section BGSL-1 (also referred to as BGTS) under plane-polarised light (PPL). The thin horizontal white line near the top is a crack produced during sample preparation.

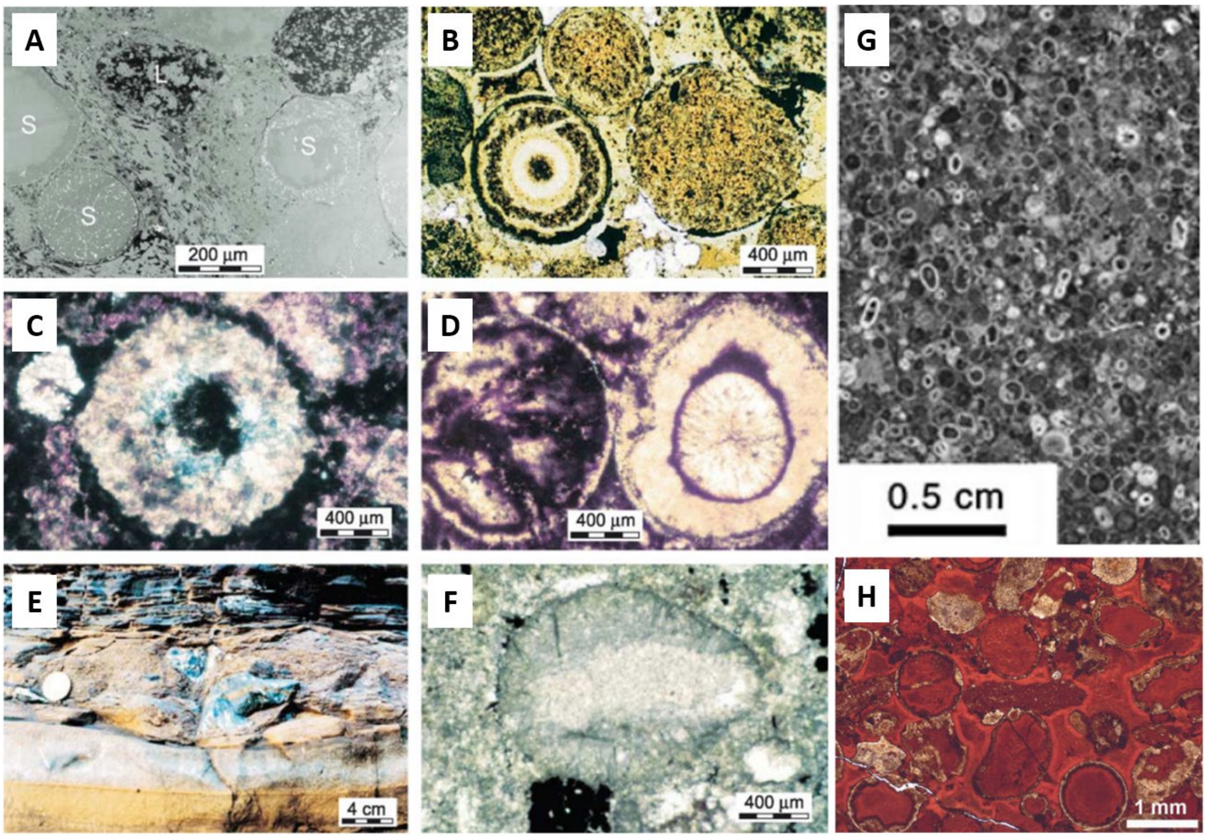

Figure 3.1: Published images of Dales Gorge spherule layer (DGSL) spherules (Modified after Pickard et al., 2004; Glass and Simonson, 2013; Sweeney and Simonson, 2008). (A) Backscattered electron image (BSE) of spherules from DDH42, Paraburdoo; S=spherules, L=lithic clasts. (B) Spherules from lower conglomerate of DDHS96-03, Tom Price. (C) Spherules from conglomerate of Wittenoom Gorge. (D) Spherules from the upper bed of DDHS96-03, Tom Price. (E) Surface exposure of unit DGS7 from the Dales Gorge site, showing polymict conglomerate with poorly rounded chert. (F) Individual spherule particle from the DGS7 unit of Dales Gorge, which lacks in overall internal features as compared to the typical spherules structures from DGSL. (G) Polished slab of unoxidised DGSL; light-coloured rims are alkali feldspar; the darker groundmass is stilpnomelane. (H) Plane polarised light image of DGSL from surface outcrop at Yampire Gorge. The reddish-brown coloured is weathered and oxidised stilpnomelane; the clear-grey coloured areas are alkali feldspar.

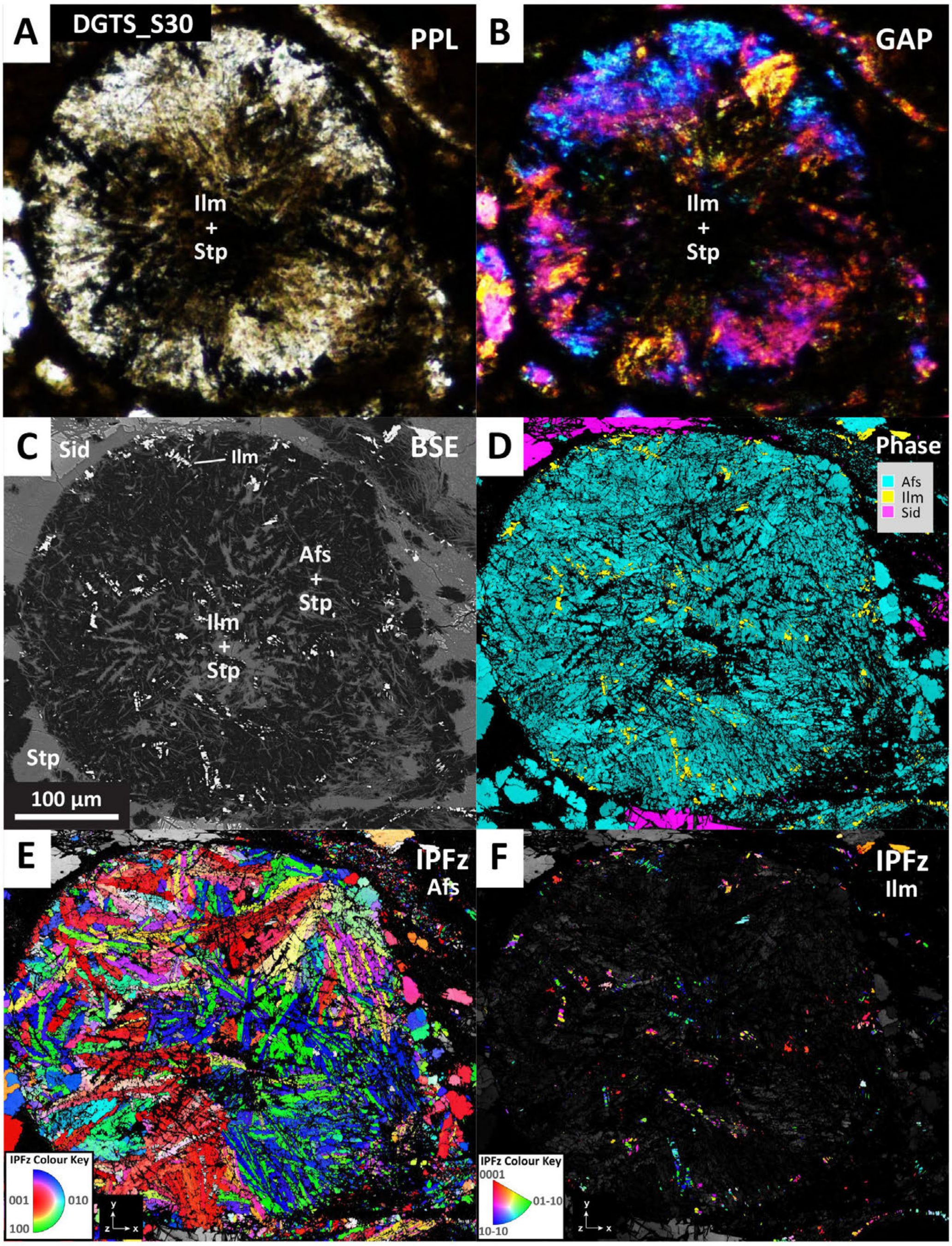

Figure 3.2: Images of DGSL spherule DGTS-S30. (A) Plane polarised light image (PPL). (B) Gypsum accessory plate image (GAP). (C) Backscattered electron image (BSE). The bright fine-grained phase is ilmenite. (D) Phase map, showing distribution of alkali feldspar (Afs), ilmenite (Ilm), and siderite (Sid). (E) Orientation map in an inverse pole figure colour scheme, showing distribution of alkali feldspar relative to the z-direction of the map reference frame (IPFz-Afs). This spherule is the most crystalline DGSL spherule analysed, as alkali feldspar comprised 60.4% of the spherule. (F) Orientation map (IPFz) showing the distribution of ilmenite. Stp = stilpnomelane.

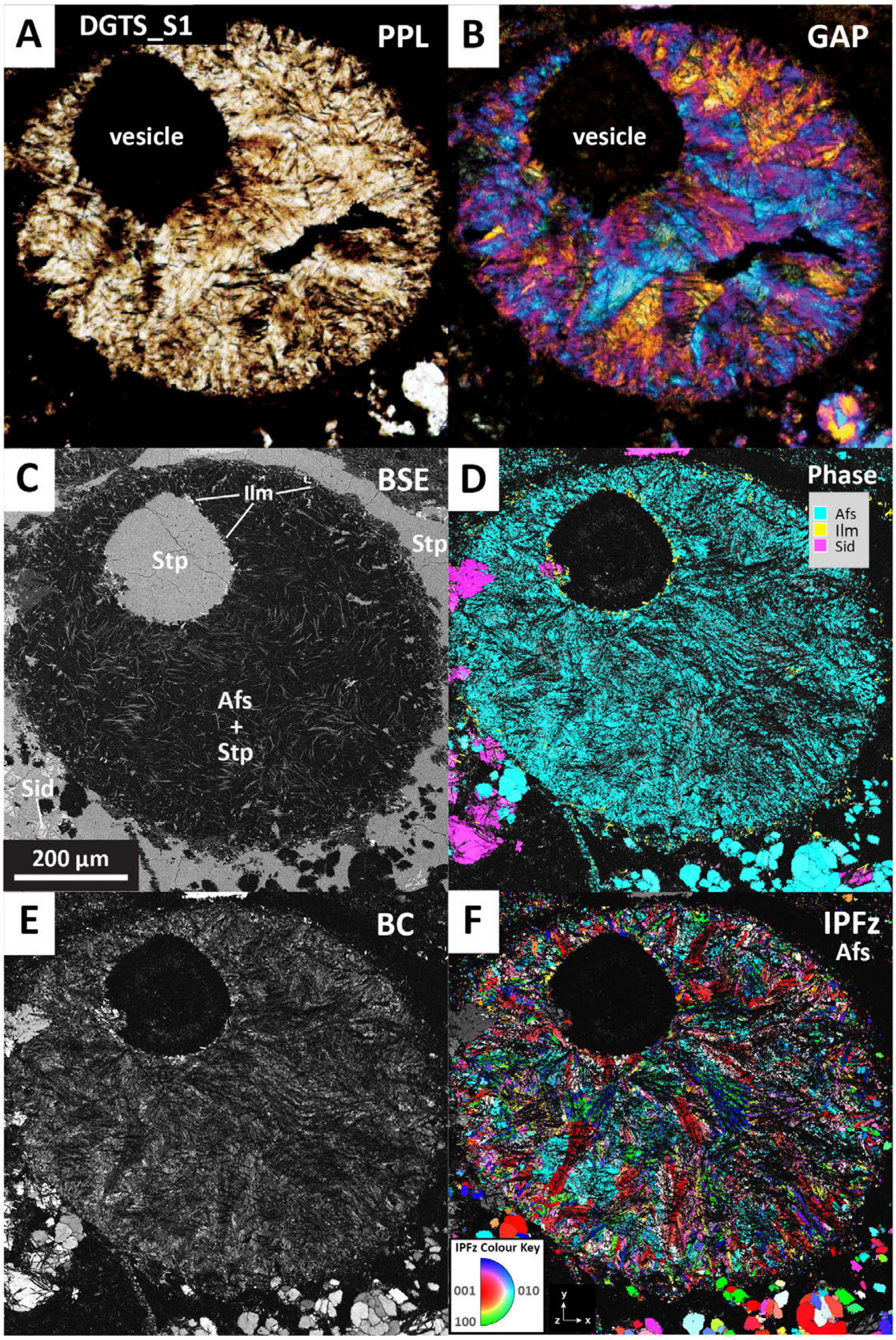

Figure 3.3: Images of radial-type DGSL spherule DGTS-S1. (A) Plane polarised light image (PPL). (B) Gypsum accessory plate image (GAP). (C) Backscattered electron image (BSE). The bright fine-grained phase is ilmenite. (D) Phase map, showing distribution of alkali feldspar (Afs), ilmenite (Ilm), and siderite (Sid). Note the difference in the habit of orthoclase (Afs) between the spherule and the matrix. Ilmenite grains line the margin of the spherule and the vesicle wall. (E) Band contrast map (BC). (F) Orientation map in an inverse pole figure colour scheme, showing distribution of alkali feldspar relative to the z-direction of the map reference frame (IPFz-Afs). Radial alkali feldspar microlites radiating inwards from spherule edge are visible. Acicular stilpnomelane crystals overprint the entire spherule. Stp = stilpnomelane.

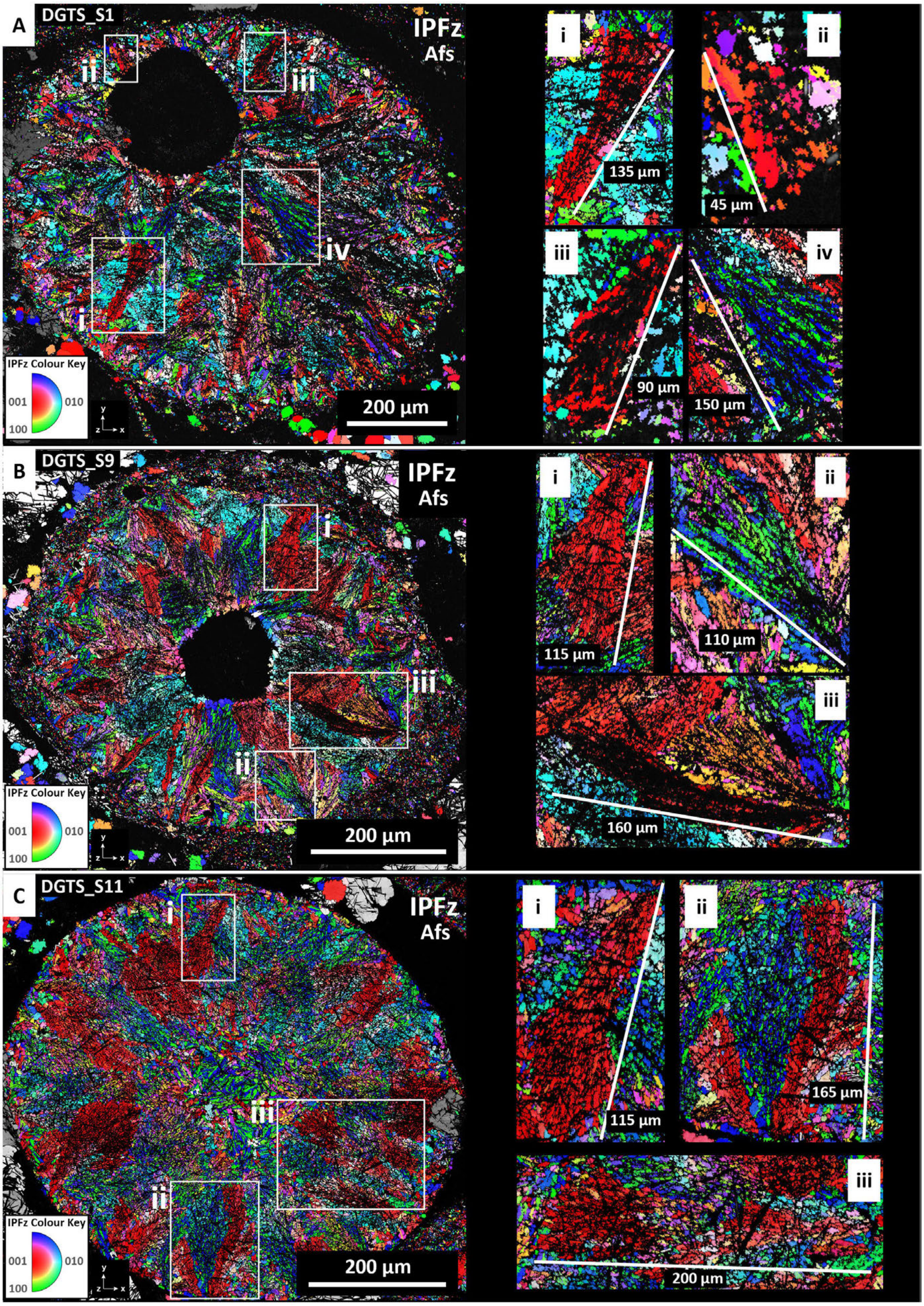

Figure 3.4: Orientation maps of alkali feldspar in radial-type Dales Gorge spherules. (A) spherule DGTS-S1, with a rounded off-centre vesicle filled with stilpnomelane. Inset boxes show (i) bowtie and (ii-iv) fan-like spherulite microstructures. (B) Spherule DGTS-S9, with a dust rim and central vesicle filled with stilpnomelane. Inset boxes (i-iii) show fan-like spherulite structures. (C) Spherule DGTS-S11, a fully crystallised spherule. Inset boxes (i-iii) show fan-like spherulite structures. Note the ubiquitous presence of cross-cutting acicular crystals of stilpnomelane (black) in the inset boxes, which divide the acicular orthoclase crystals into shorter grain lengths

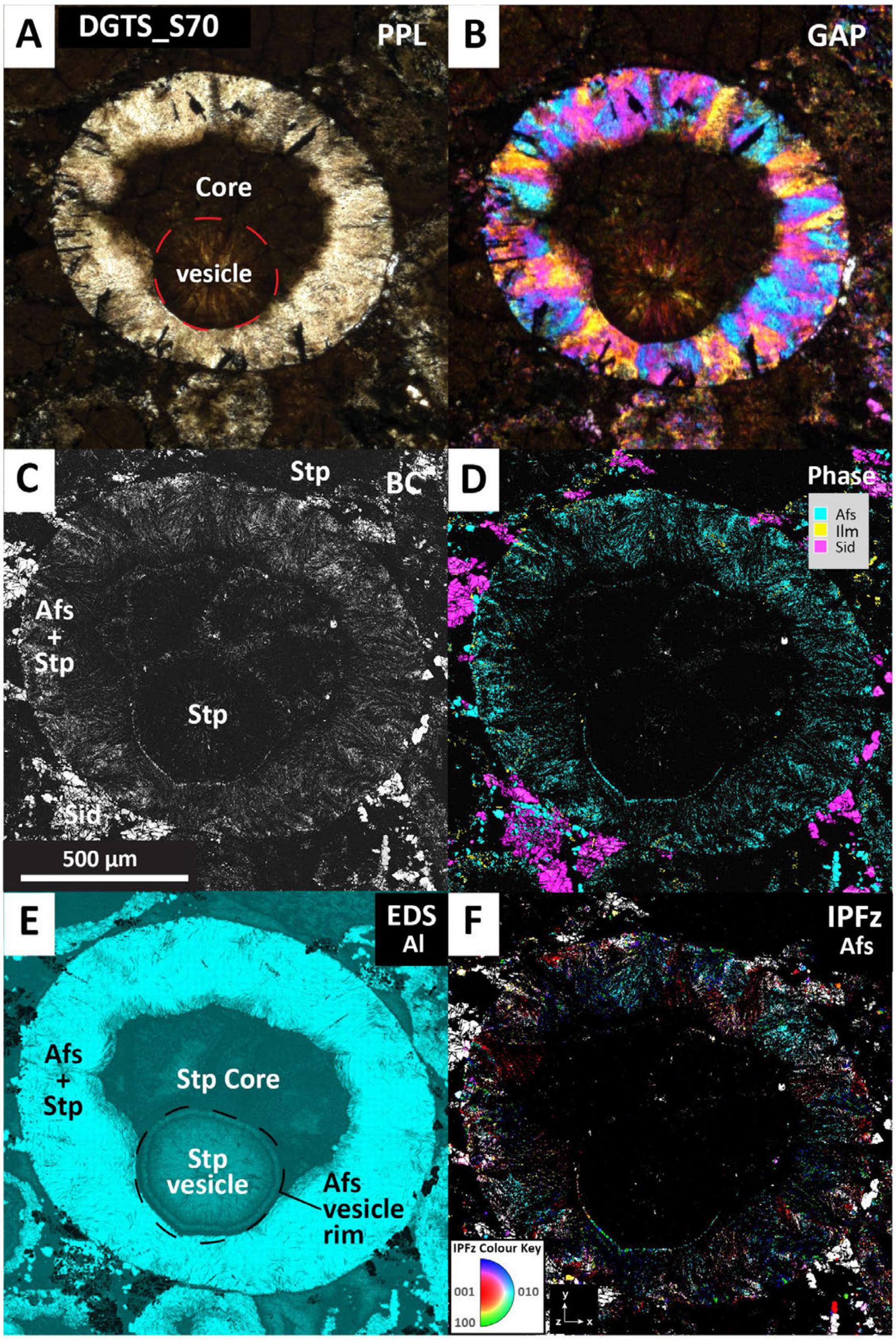

Figure 3.5: Images of radial-type DGSL spherule DGTS-S70, with a formerly glass core. (A) Plane polarised light image (PPL). Radial alkali feldspar microlites, intergrown with an opaque mineral, are visible growing inward from the spherule margin. (B) Gypsum accessory plate image (GAP). (C) Band contrast map (BC). (D) Phase map showing alkali feldspar (Afs), ilmenite (Ilm), and siderite (Sid). The incomplete crystallisation of feldspar is visible, as the crystals form a boundary with the central core, originally consisting of quenched glass. (E) Energy dispersive spectroscopy map of aluminium. A distinctive botryoidal boundary between the feldspar rim and formerly glassy core is evident. A round vesicle filled with radiating stilpnomelane crystals is also visible. (F) Orientation map in an inverse pole figure colour scheme, showing distribution of alkali feldspar relative to the z-direction of the map reference frame (IPFz-Afs).

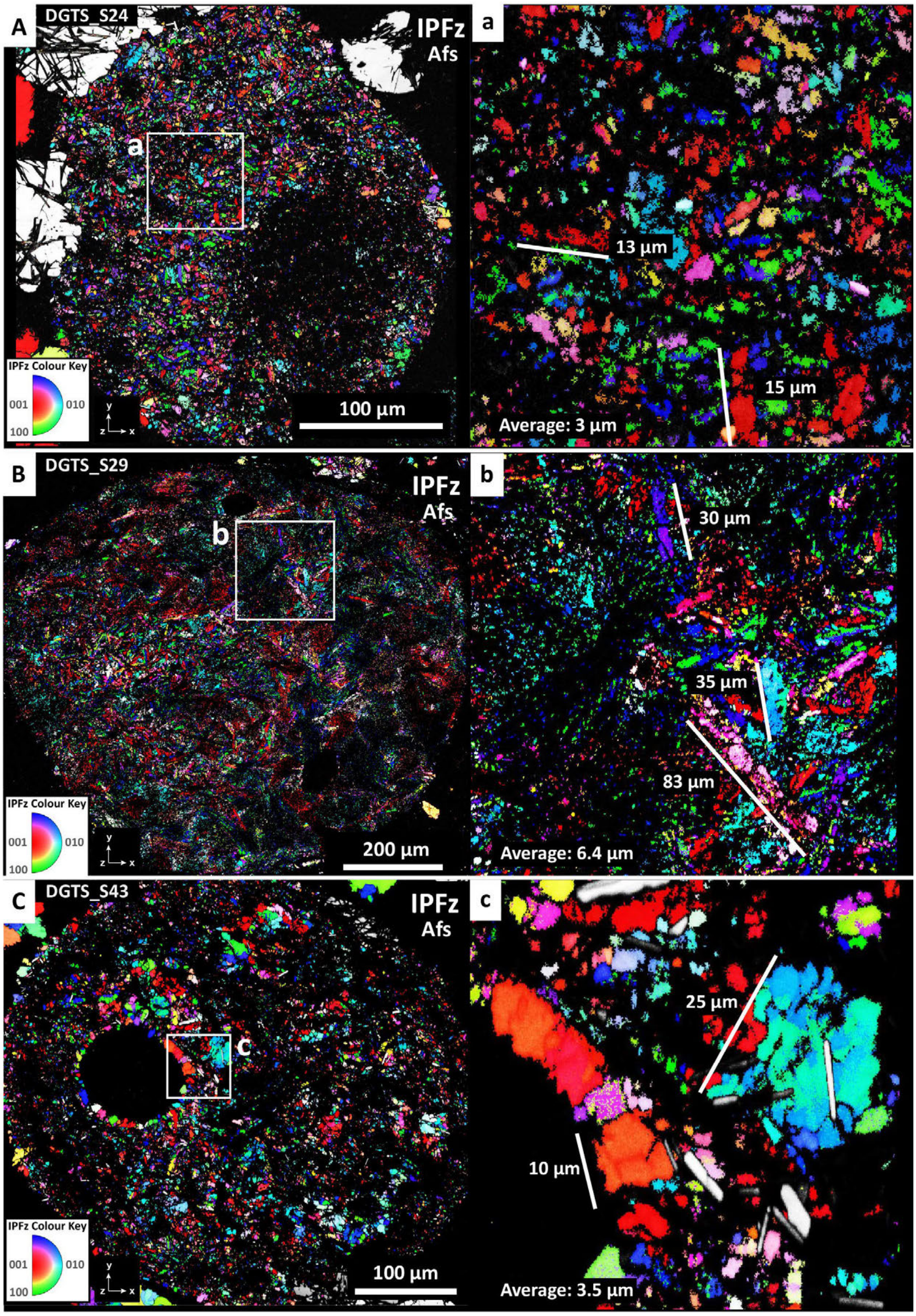

Figure 3.6: Orientation maps of alkali feldspar in random-type Dales Gorge spherules. (A) Spherule DGTS-S24, with randomly oriented alkali feldspar crystals. The bottom right side of the spherule indicates an area with more stilpnomelane, which may represent a former core. Inset box (a) shows very fine-grained alkali feldspar with sub-equant textures. (B) Spherule DGTS-S29, which contains a few small vesicles. Inset box (b) shows prismatic alkali feldspar grains. (C) Spherule DGTS-S43, with an off-centre filled vesicle. Inset (c) shows mostly equant alkali feldspar grains (right) and blocky feldspar grains that line the vesicle wall (left). The blocky feldspar grains likely formed during diagenetic alteration.

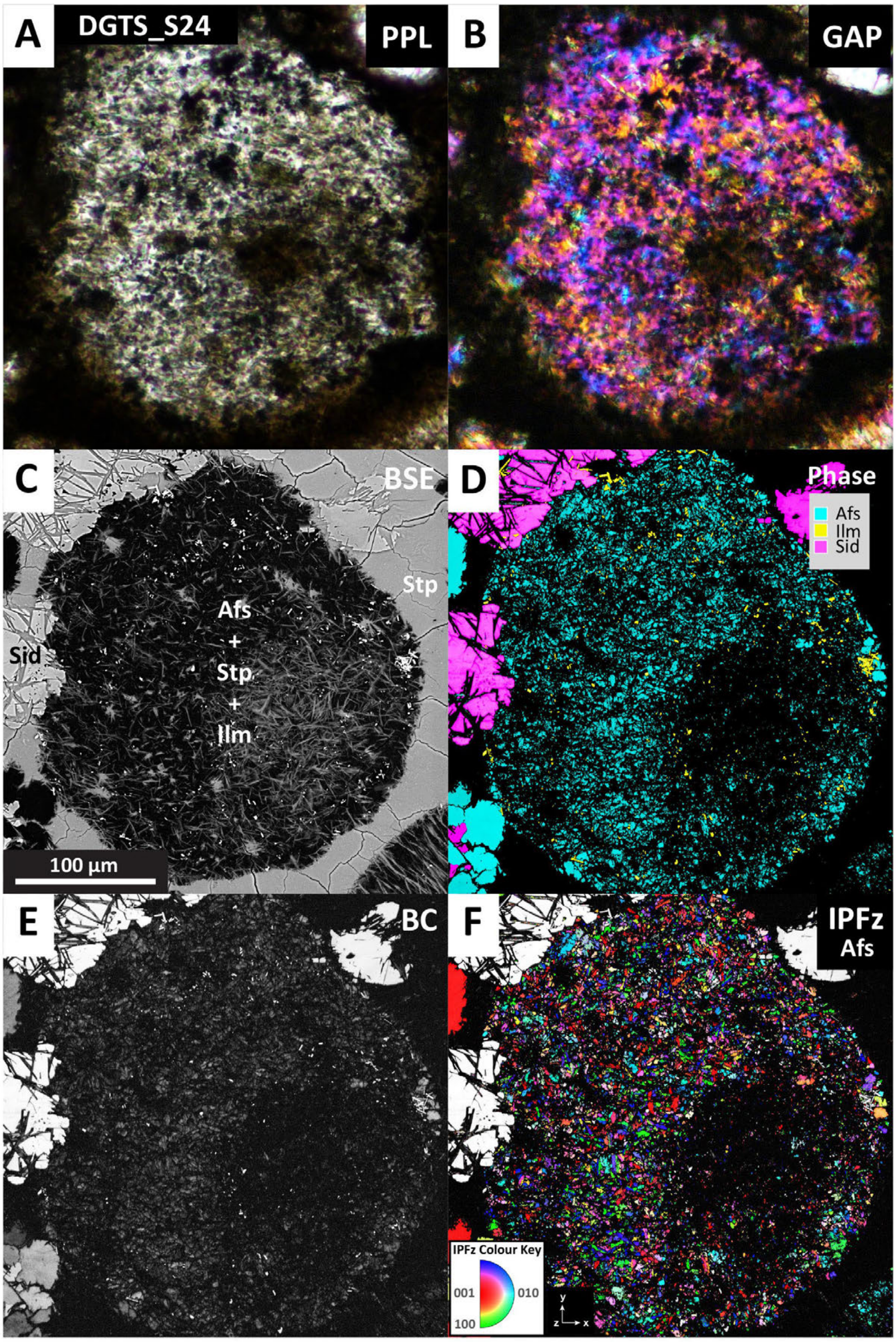

Figure 3.7: Images of random-type DGSL spherule DGTS-S24. (A) Plane polarised light image (PPL). (B) Gypsum accessory plate image (GAP). (C) Backscattered electron image (BSE). (D) Phase map; alkali feldspar (Afs), ilmenite (Ilm), siderite (Sid). Both alkali feldspar and ilmenite are very fine grained and have random orientations. (E) Band contrast map (BC). (F) Orientation map in an inverse pole figure colour scheme, showing distribution of alkali feldspar relative to the z-direction of the map reference frame (IPFz-Afs). Stp = stilpnomelane.

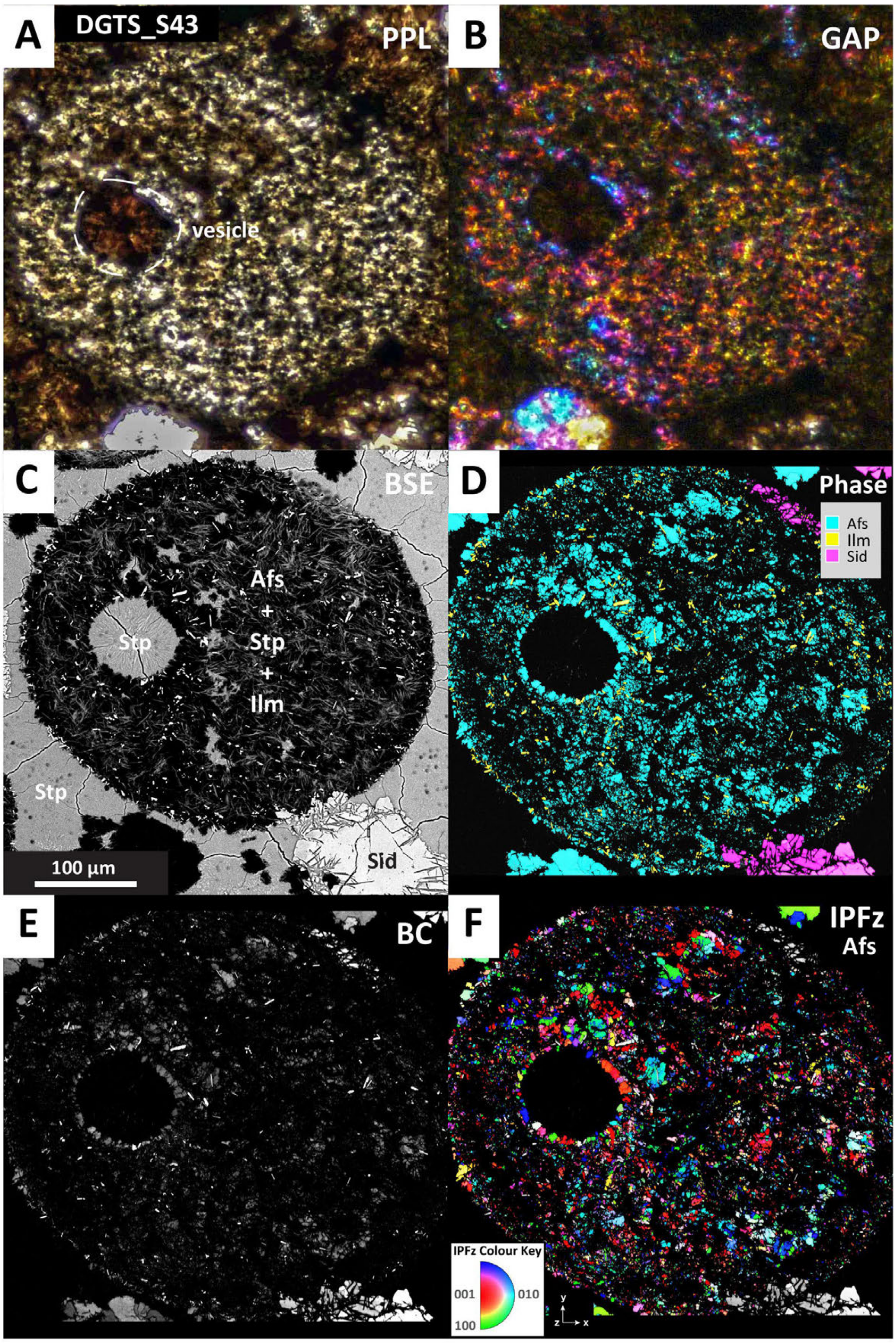

Figure 3.8: Images of random-type DGSL spherule DGTS-S43. (A) Plane polarised light image (PPL). (B) Gypsum accessory plate image (GAP). (C) Backscattered electron image (BSE). An off-centre vesicle filled with Stp is labelled. (D) Phase map; alkali feldspar (Afs), ilmenite (Ilm), siderite (Sid). Both alkali feldspar and ilmenite are very fine grained and have random orientations. (E) Band contrast map (BC). (F) Orientation map in an inverse pole figure colour scheme, showing distribution of alkali feldspar relative to the z-direction of the map reference frame (IPFz-Afs). Stp = stilpnomelane.

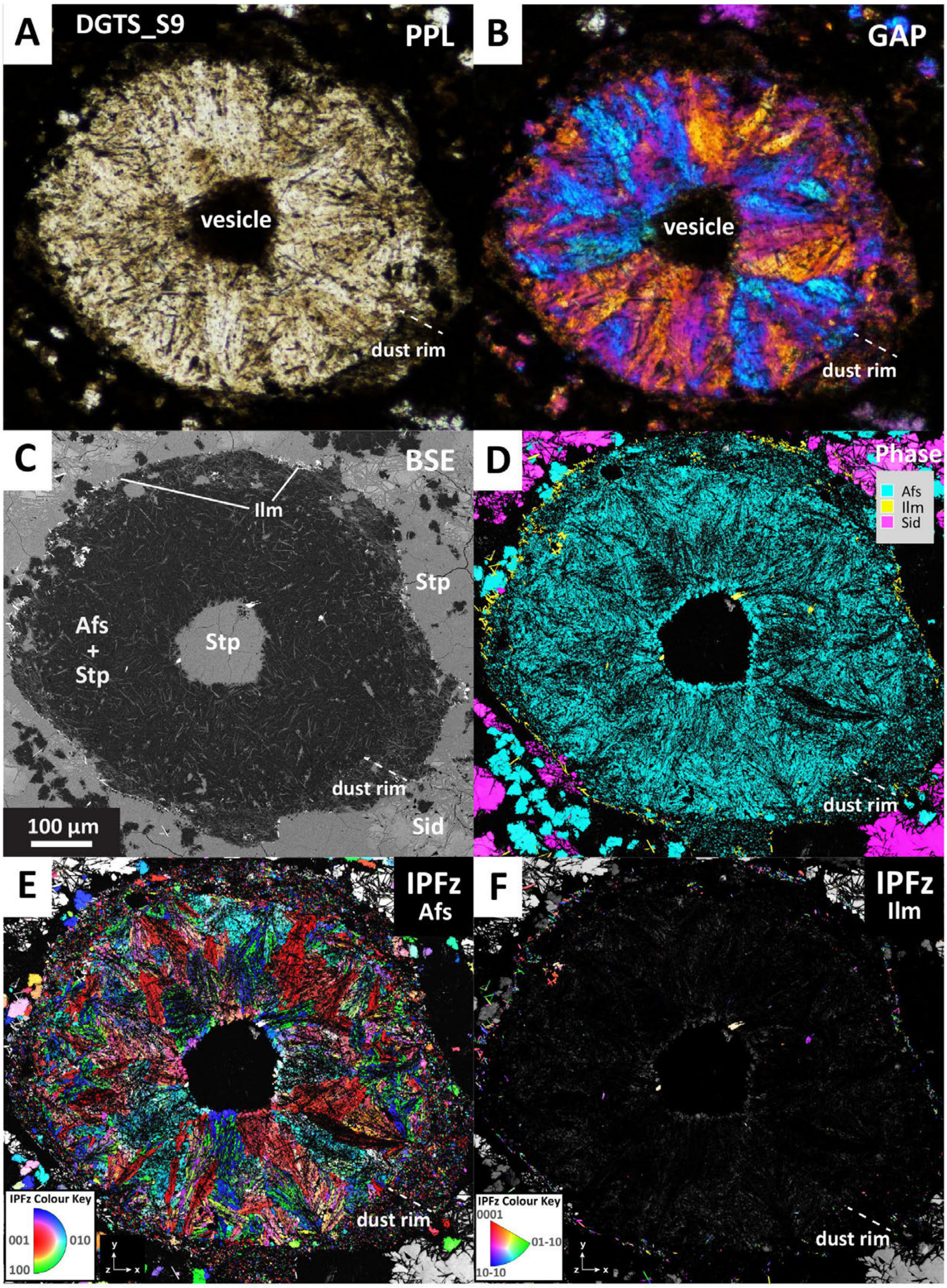

Figure 3.9: Images of radial-type DGSL spherule DGTS-S9, with a dust rim. (A) Plane polarised light image (PPL). The dust rim is not very visible in PPL. (B) Gypsum accessory plate image (GAP). (C) Backscattered electron image (BSE). The dust rim is not very visible in BSE. An off-centre vesicle filled with Stp is labelled. (D) Phase map; alkali feldspar (Afs), ilmenite (Ilm), siderite (Sid). Both alkali feldspar and ilmenite are very fine grained and have random orientations. (E) Orientation map in an inverse pole figure colour scheme, showing distribution of alkali feldspar relative to the z-direction of the map reference frame (IPFz-Afs). Fan-like radial feldspar spherulite structures surround the central filled vesicle. A continuous rim of feldspar dust is visible, which is line with ilmenite grains. (F) Orientation map in an inverse pole figure colour scheme, showing distribution of ilmenite relative to the z-direction of the map reference frame (IPFz-Ilm). Stp = stilpnomelane.

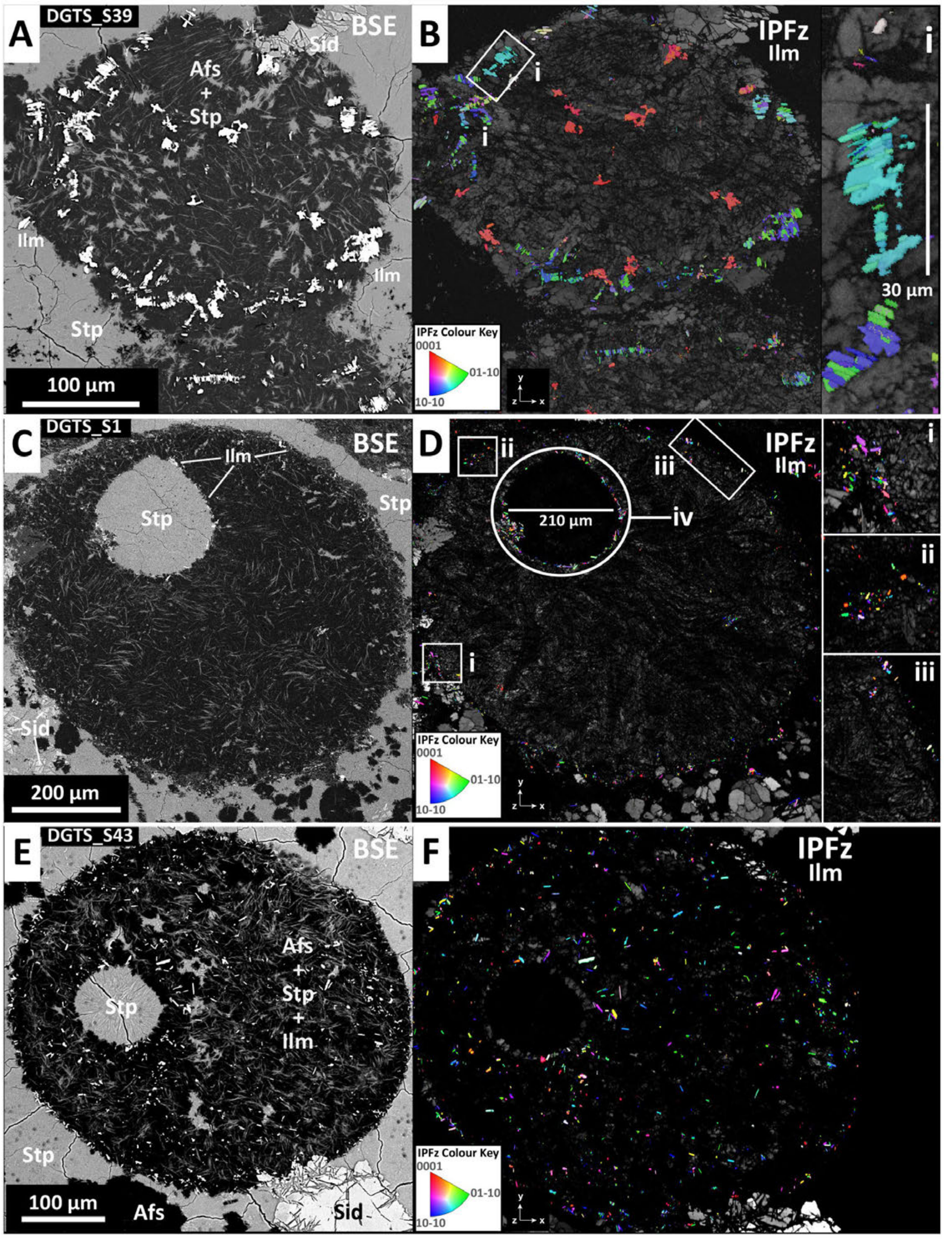

Figure 3.10: Images of different ilmenite occurrences in Dales Gorge feldspathic microkrystites. (A) Backscattered electron image of spherule DGTS-S39 showing a representative ilmenite array. (B) Orientation map of spherule DGTS-S39 in an inverse pole figure colour scheme, showing distribution of ilmenite in the z-plane (IPFz). The ilmenite arrays consist of adjacent, but discontinuous grains. Inset (i) is a close-up view of an ilmenite array that is ~30 µm long. (C) Backscattered electron image of spherule DGTS-S1 showing ilmenite lining the walls of a filled vesicle. (D) Orientation map of spherule DGTS-39 in an inverse pole figure colour scheme, showing distribution of ilmenite relative to the z-direction of the map reference frame (IPFz). Insets (i-iii) show aligned ilmenite grains along the outer margin of the spherule. Inset (iv) shows ilmenite lining the vesicle wall. (E) Backscattered electron image of spherule DGTS-S43 showing disseminated ilmenite within the spherule. (F) Orientation map of spherule DGTS-S43 in an inverse pole figure colour scheme, showing distribution of ilmenite relative to the z-direction of the map reference frame (IPFz). Sid = siderite. Stp = stilpnomelane.

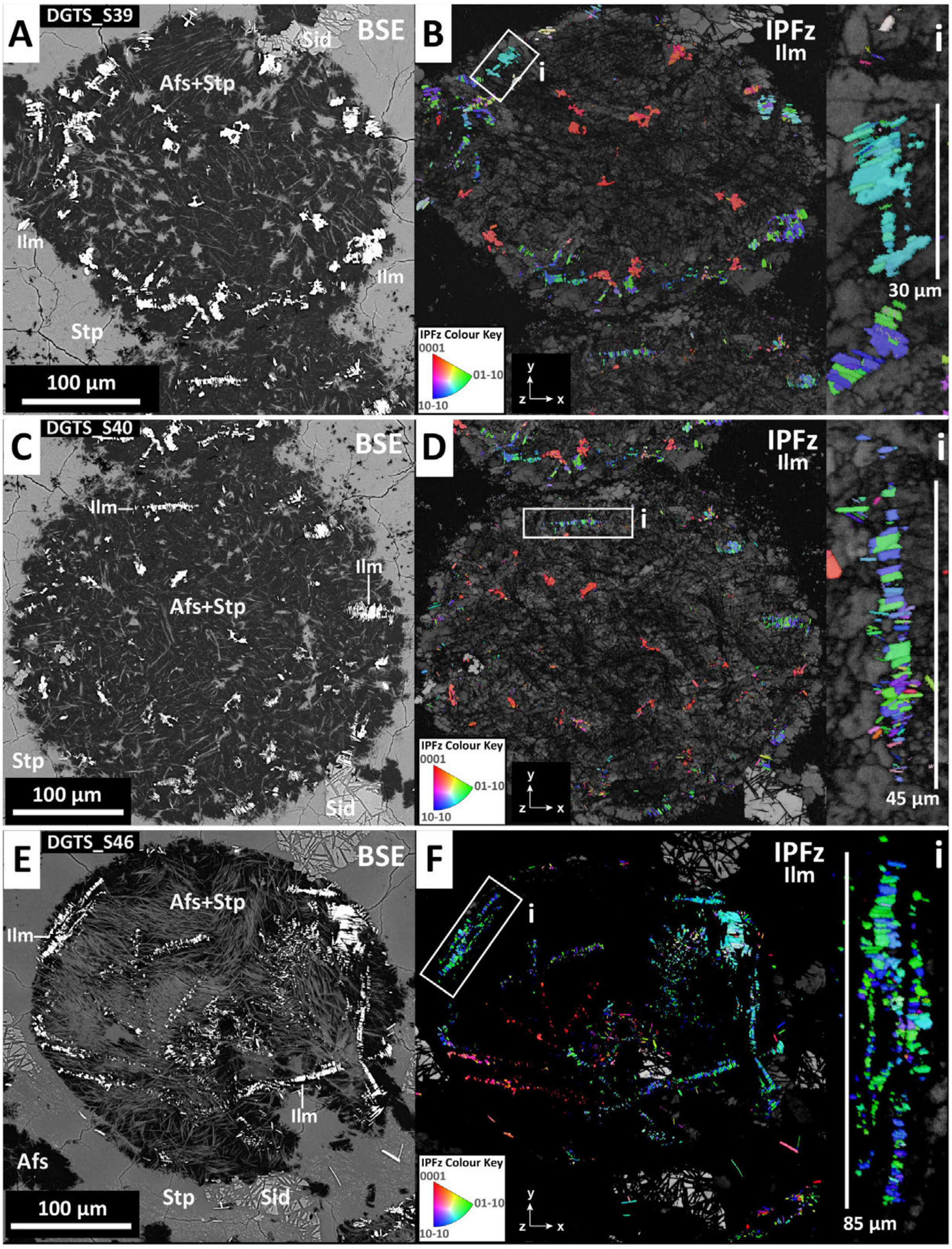

Figure 3.11: Images of ilmenite arrays in Dales Gorge feldspathic microkrystites. (A) Backscattered electron image of spherule DGTS-S39, with ilmenite arrays. (B) Orientation map of spherule DGTS-S39 in an inverse pole figure colour scheme, showing distribution of ilmenite relative to the z-direction of the map reference frame (IPFz). The Inset (i) is a close-up view of two ilmenite arrays. (C) Backscattered electron image of spherule DGTS-S40 showing ilmenite multiple ilmenite arrays. (D) Orientation map of spherule DGTS-40 in an inverse pole figure colour scheme, showing distribution of ilmenite relative to the z-direction of the map reference frame (IPFz). Inset (i) shows a ~45 µm long ilmenite array, consisting of many adjacent crystals. (E) Backscattered electron image of spherule DGTS-S46 showing multiple ilmenite arrays. (F) Orientation map of spherule DGTS-S46 in an inverse pole figure colour scheme, showing distribution of ilmenite relative to the z-direction of the map reference frame (IPFz). In set (i) shows a ~85 µm long, complex ilmenite array, consisting of many adjacent crystals. Sid = siderite. Stp = stilpnomelane.

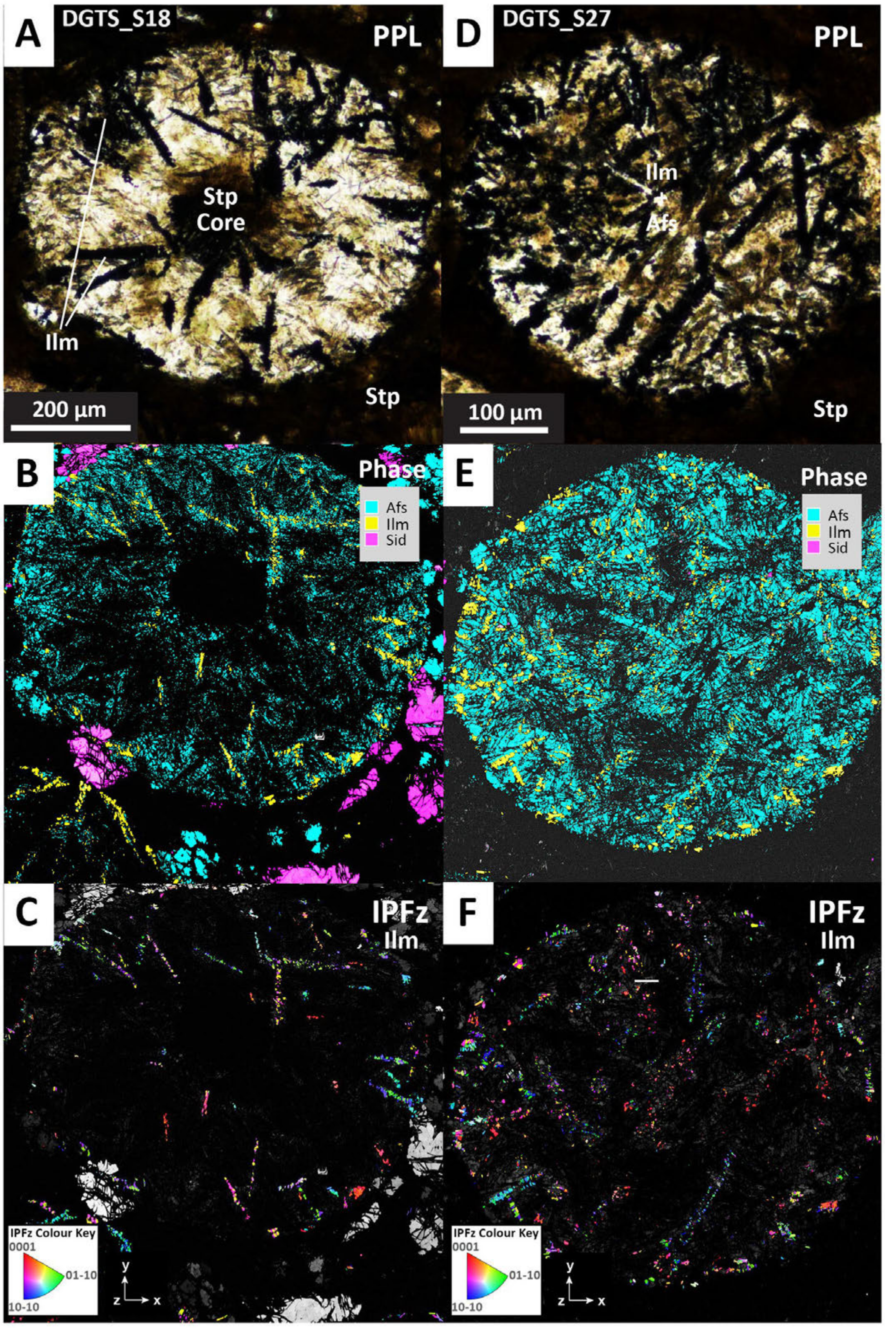

Figure 3.12: Comparative images of ilmenite arrays in Dales Gorge feldspathic microkrystites. (A) Plane polarised light image (PPL) of spherule DGTS-S18. (B) Phase map of spherule DGTS-S18, showing alkali feldspar (Afs), ilmenite (Ilm), siderite (Sid). (C) Orientation map of spherule DGTS-S18 in an inverse pole figure colour scheme, showing distribution of ilmenite relative to the z-direction of the map reference frame (IPFz). (D) Plane polarised light image (PPL) of spherule DGTS-S27. (E) Phase map of spherule DGTS-S27, showing alkali feldspar (Afs), ilmenite (Ilm), siderite (Sid). (F) Orientation map of spherule DGTS-S27 in an inverse pole figure colour scheme, showing distribution of ilmenite relative to the z-direction of the map reference frame (IPFz). In general, ilmenite is often more visible in PPL images, due to the strong contrast with feldspar, and a larger representative sample thickness (~30 µm), as compared to EBSD, which only samples the upper ~10-20 nm of the sample surface. However, EBSD has the ability to quantify the identity of the opaque oxide phase. Stp = stilpnomelane.

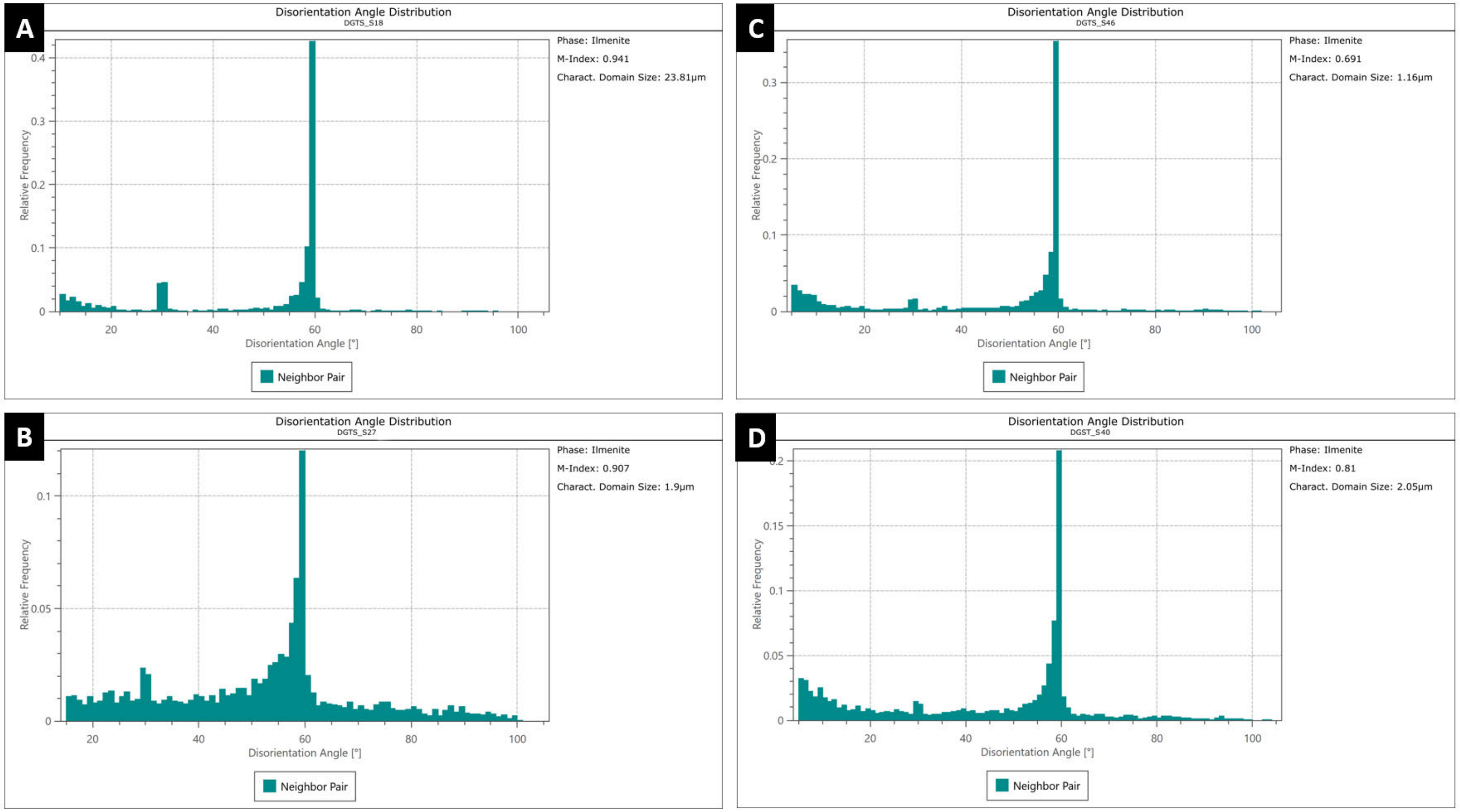

Figure 3.13: Disorientation angle relationships for individual ilmenite arrays from four different Dales Gorge feldspathic microkrystites. (A) Spherule DGTS-S18 (see Fig. 3.10A-C). (B) Spherule DGTS-S27 (see Fig. 312D-F). (C) Spherule DGTS-S46 (see Fig. 3.11E-F). (D) Spherule DGTS-S40 (see Fig. 3.11A-B). Each of the arrays shows a main disorientation peak at 60°. The disorientation results from a systematic twin relation of 60°/<0001>.

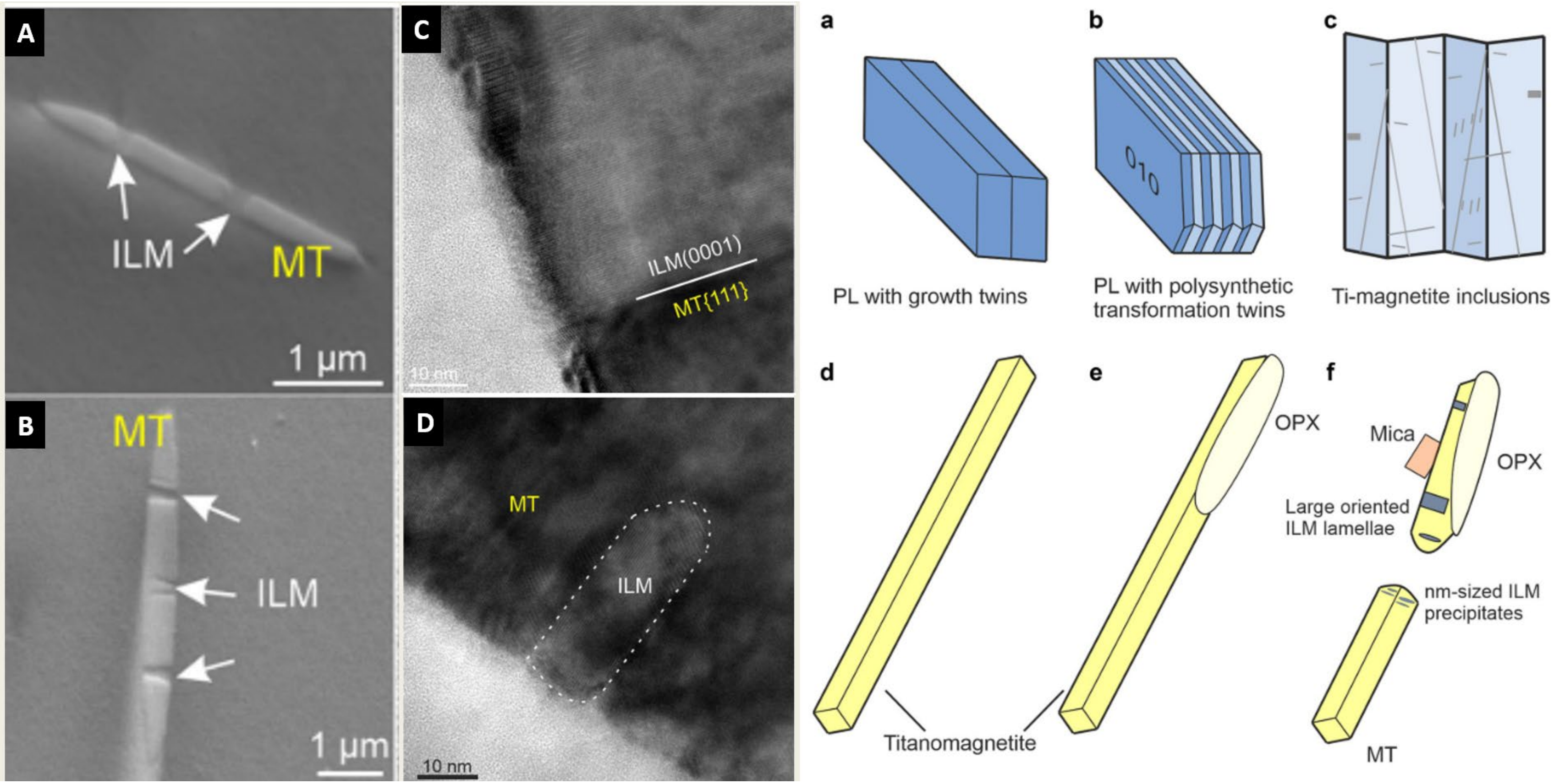

Figure 3.14: Example of ilmenite exsolution from magnetite inclusions in plagioclase (Bian et al., 2021). Left: (A)-(B) secondary electron images at 70° tilt, showing magnetite micro-inclusions hosting ilmenite lamellae. (C)-(D) High-resolution TEM images showing sharp contacts between ultrafine ilmenite lamellae and magnetite host, within plagioclase. Right: (a)-(f) Schematic illustrations showing the genesis of ilmenite inclusions from titanomagnetite plagioclase with Carlsbad twins.

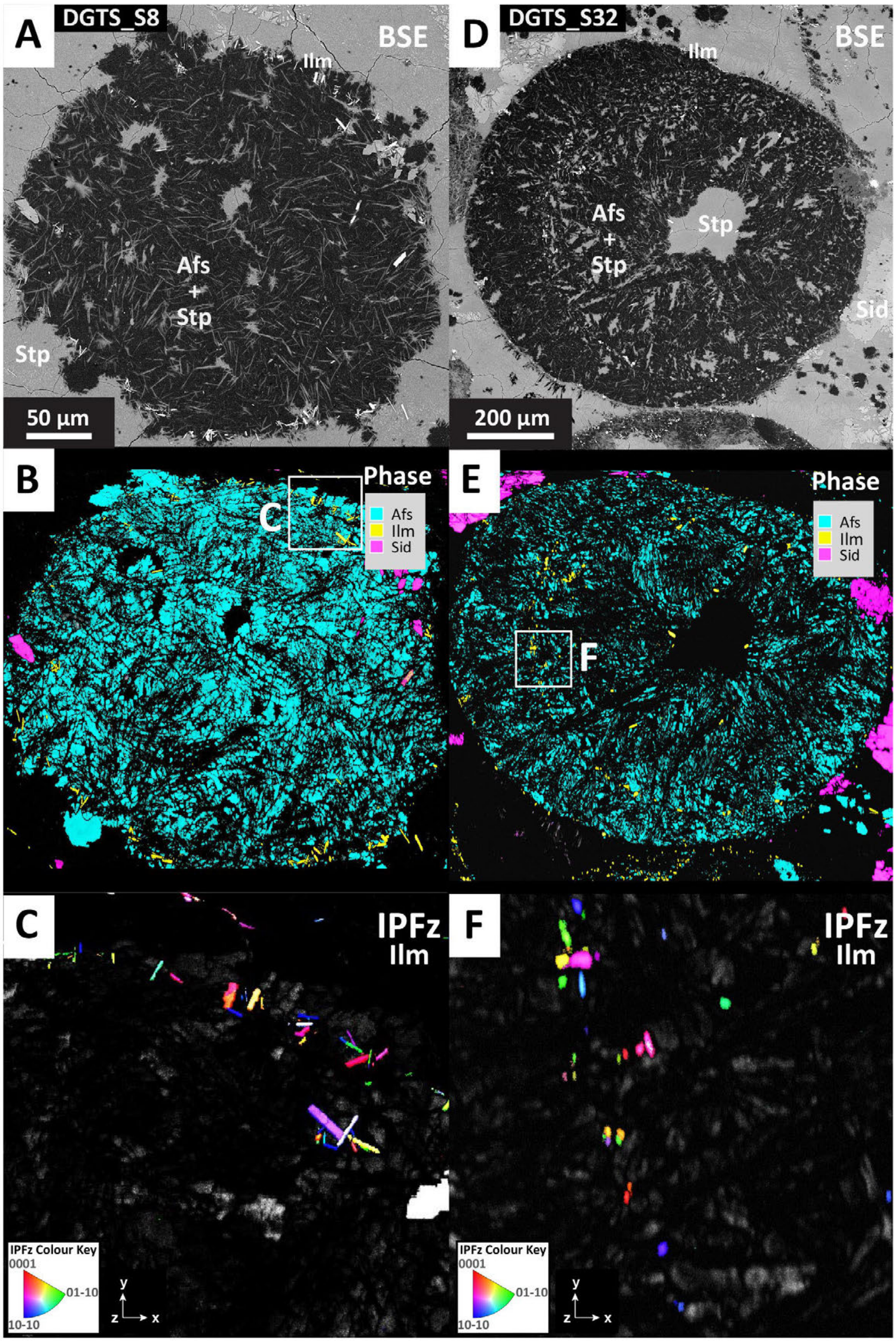

Figure 3.15: Examples of ilmenite lining exterior surfaces of Dales Gorge feldspathic microkrystites. (A) Backscattered electron image (BSE) of spherule DGTS-S8. (B) Phase map of spherule DGTS-S8, showing alkali feldspar (Afs), ilmenite (Ilm), siderite (Sid). (C) Orientation map of spherule DGTS-S8 in an inverse pole figure colour scheme, showing distribution of ilmenite in the z-plane (IPFz) from the inset shown in (B). (D) BSE image of spherule DGTS-S32, a merged spherule. (E) Phase map of spherule DGTS-S32, showing alkali feldspar (Afs), ilmenite (Ilm), siderite (Sid). (F) Orientation map of spherule DGTS-S32 in an inverse pole figure colour scheme, showing distribution of ilmenite relative to the z-direction of the map reference frame (IPFz) from the inset shown in (E). Stp = stilpnomelane.

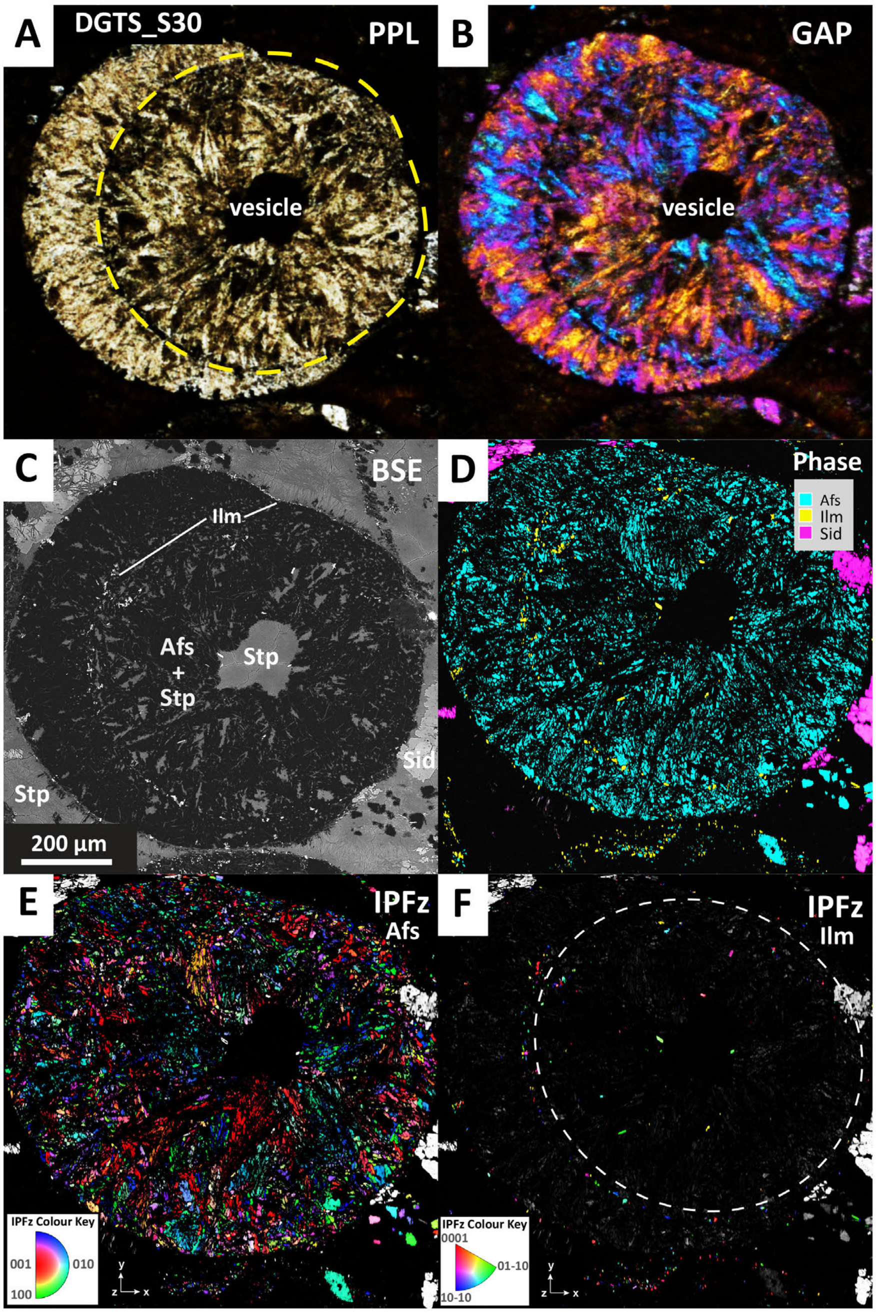

Figure 3.16: Images of radial-type DGSL spherule DGTS-S32, a merged spherule. (A) Plane polarised light image (PPL), showing a ring of ilmenite crystals lining the inner spherule (yellow dashed line). (B) Gypsum accessory plate image (GAP). Ilmenite grains are visible as black (opaque) grains lining the inner spherule. (C) Backscatter electron image (BSE). Ilmenite grains lining the inner spherule are visible as a bright phase. (D) Phase map; alkali feldspar (Afs), ilmenite (Ilm), siderite (Sid). (E) Orientation map in an inverse pole figure colour scheme, showing distribution of alkali feldspar relative to the z-direction of the map reference frame (IPFz). (F) Orientation map in an inverse pole figure colour scheme, showing distribution of ilmenite relative to the z-direction of the map reference frame (IPFz). Ilmenite forms a circular ring (white dashed line) around the inner spherule. Stp = stilpnomelane. The encapsulation of ilmenite around the internal margin of a merged spherule provides direct evidence that it is likely to be a primary (pre-depositional) igneous mineral.

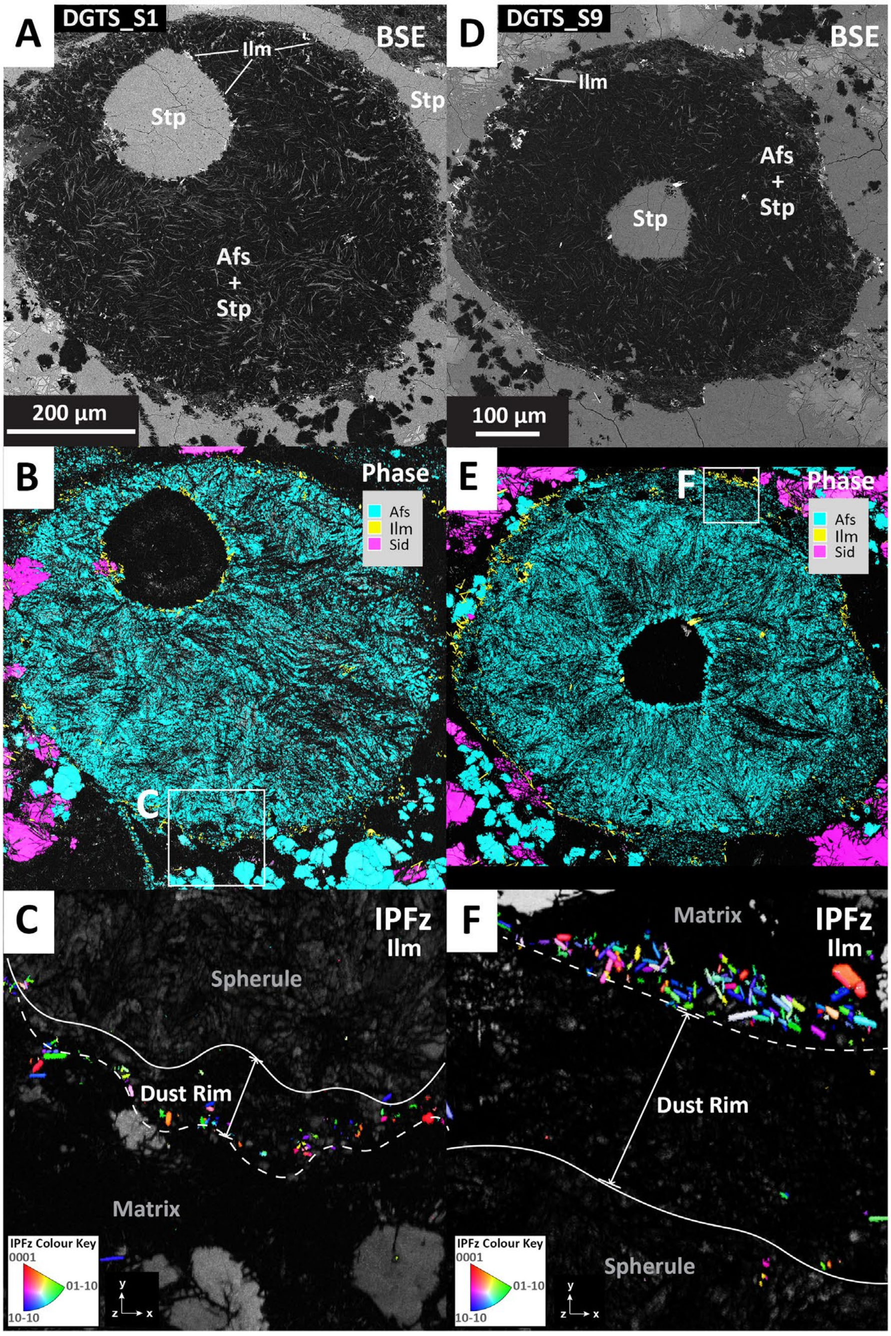

Figure 3.17: Examples of ilmenite lining the exterior surfaces of Dales Gorge feldspathic microkrystites with dust rims. (A) Backscattered electron image (BSE) of spherule DGTS-S1, a radial-type feldspathic microkrystite with a dust rim. (B) Phase map of spherule DGTS-S1, showing alkali feldspar (Afs), ilmenite (Ilm), siderite (Sid). (C) Orientation map of spherule DGTS-S1 in an inverse pole figure colour scheme, showing distribution of ilmenite relative to the z-direction of the map reference frame (IPFz) from the inset shown in (B). Ilmenite is visible lining the dust rim on the exterior surface of the spherule. Thickest dust rim width measured = 30 µm. (D) BSE image of spherule DGTS-S9, a radial-type feldspathic microkrystite with a dust rim. (E) Phase map of spherule DGTS-S9, showing alkali feldspar (Afs), ilmenite (Ilm), siderite (Sid). (F) Orientation map of spherule DGTS-S9 in an inverse pole figure colour scheme, showing distribution of ilmenite relative to the z-direction of the map reference frame (IPFz) from the inset shown in (E). Ilmenite is visible lining the dust rim on the exterior surface of the spherule. Thickest dust rim width measured = 50 µm.

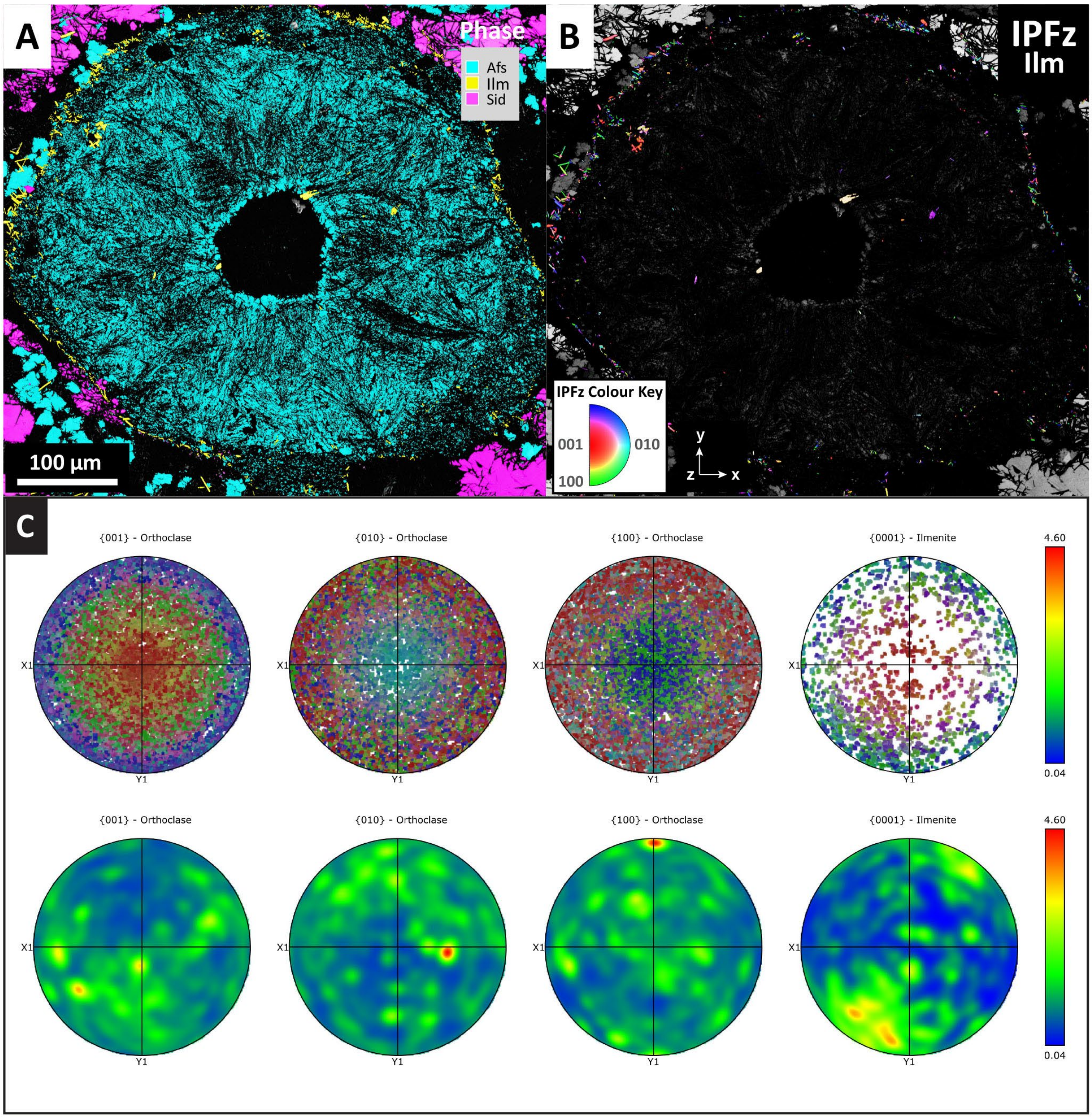

Figure 3.18: Comparison of crystal orientations of orthoclase and ilmenite in Dales Gorge feldspathic microkrystite DGTS-S9. (A) Phase map showing alkali feldspar (Afs), ilmenite (Ilm), siderite (Sid). (B) Orientation map in an inverse pole figure colour scheme, showing distribution of ilmenite relative to the z-direction of the map reference frame (IPFz). Both (A) and (B) shows ilmenite lining the dust rim, rather than the radial alkali feldspar grains on the spherule interior. (C) Pole figures for both alkali feldspar (orthoclase) and ilmenite from the outer dust rim. Ilmenite does not appear to share any crystallographic preferred orientation (CPO) or shape preferred orientation (SPO) with the dust-sized alkali feldspar grains.

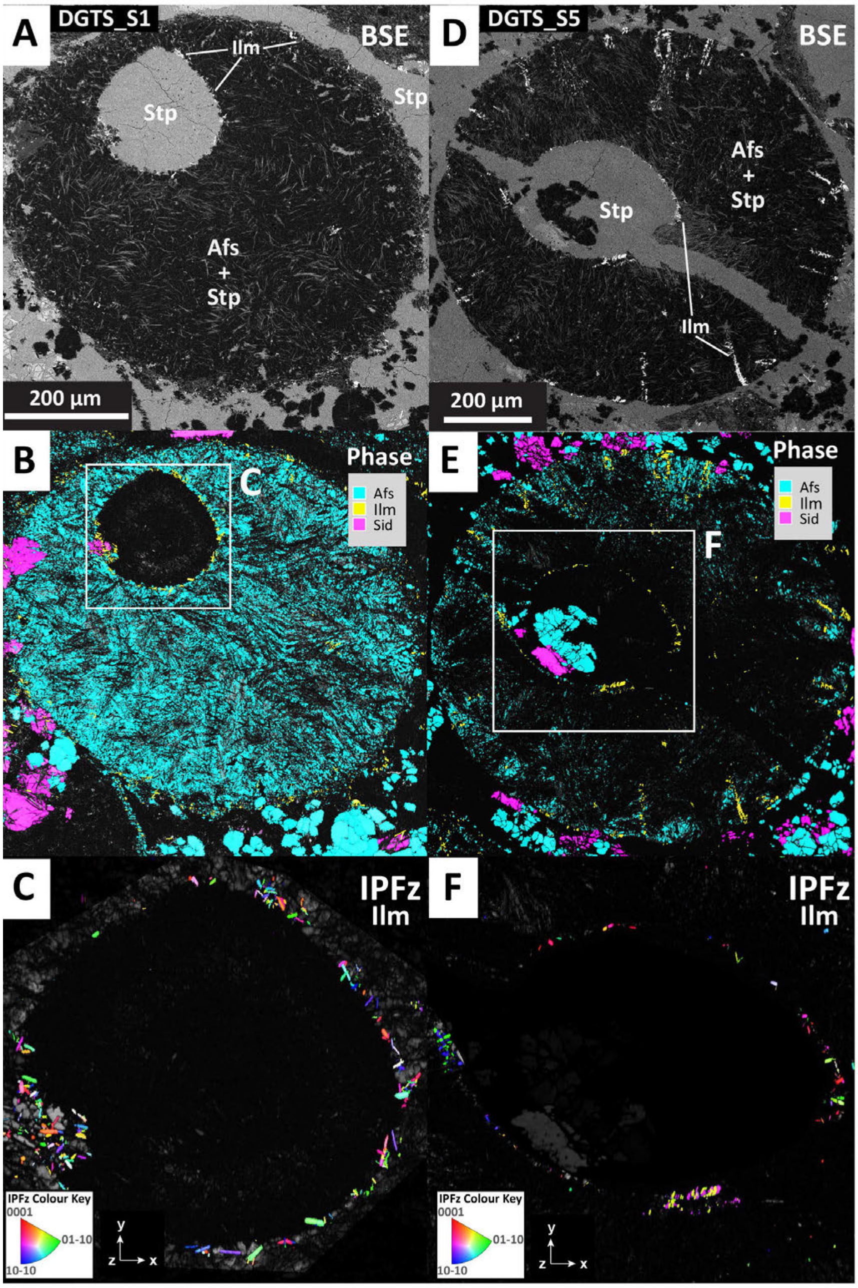

Figure 3.19: Examples of ilmenite lining walls of vesicles in Dales Gorge feldspathic microkrystites. (A) Backscattered electron image (BSE) of spherule DGTS-S1, a radial-type feldspathic microkrystite with an off-centre filled vesicle. (B) Phase map of spherule DGTS-S1, showing alkali feldspar (Afs), ilmenite (Ilm), siderite (Sid). (C) Orientation map of spherule DGTS-S1 in an inverse pole figure colour scheme, showing distribution of ilmenite relative to the z-direction of the map reference frame (IPFz) from the inset shown in (B). Ilmenite is visible lining vesicle wall. (D) BSE image of spherule DGTS-S5, a radial-type feldspathic microkrystite with a central filled vesicle that has been breached by a younger Stp vein. (E) Phase map of spherule DGTS-S5, showing alkali feldspar (Afs), ilmenite (Ilm), siderite (Sid). (F) Orientation map of spherule DGTS-S5 in an inverse pole figure colour scheme, showing ilmenite relative to the z-direction of the map reference frame (IPFz) from the inset shown in (E). Ilmenite is visible lining the wall of the filled vesicle. Note that ilmenite does not occur along the cross-cutting Stp vein. Stp = stilpnomelane.

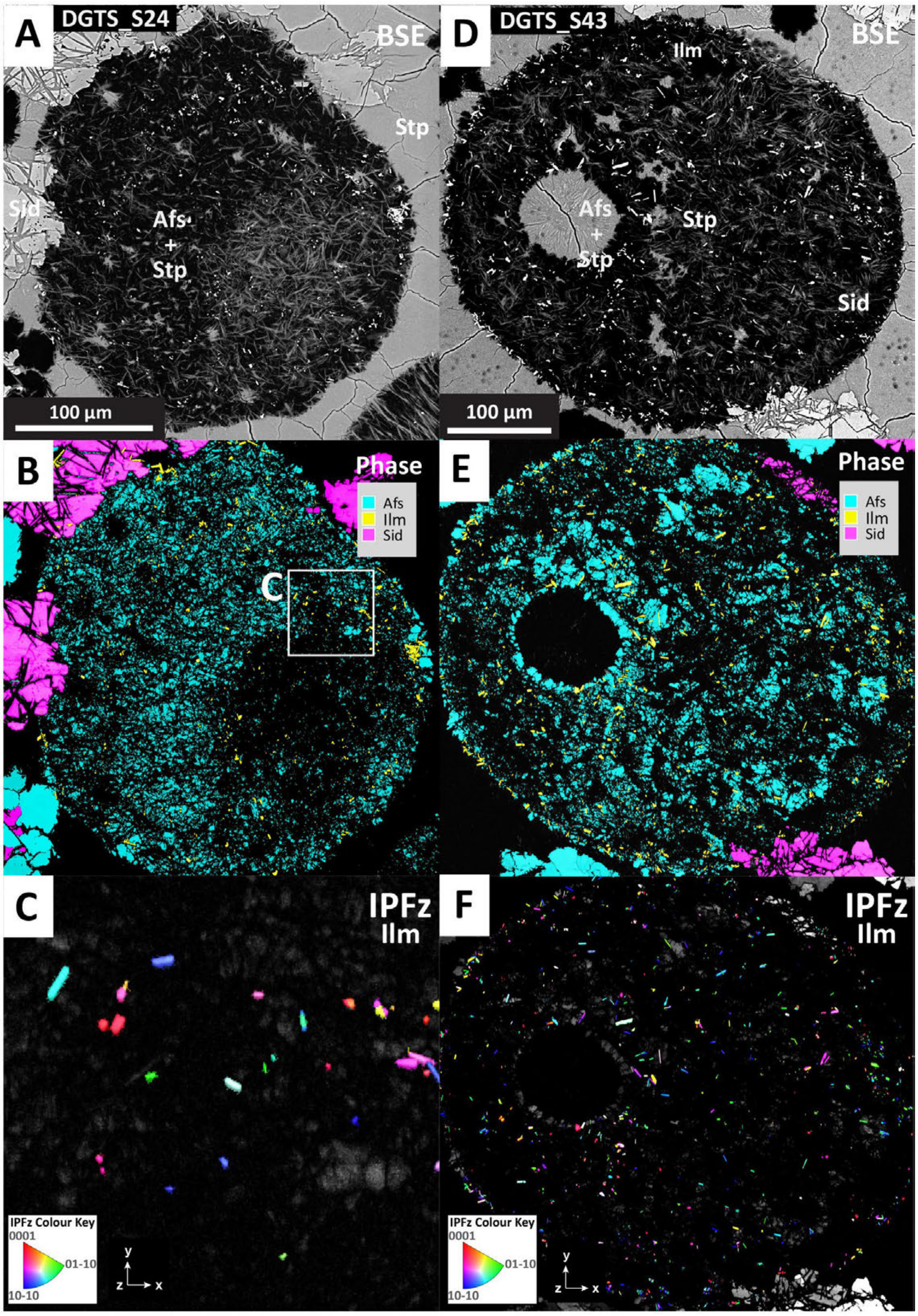

Figure 3.20: Examples of disseminated ilmenite in Dales Gorge feldspathic microkrystites. (A) Backscattered electron image (BSE) of spherule DGTS-S24, a random-type feldspathic microkrystite. (B) Phase map of spherule DGTS-S24, showing alkali feldspar (Afs), ilmenite (Ilm), siderite (Sid). (C) Orientation map of spherule DGTS-S24 in an inverse pole figure colour scheme, showing distribution of ilmenite relative to the z-direction of the map reference frame (IPFz) from the inset shown in (B). (D) BSE image of spherule DGTS-S43, a random-type feldspathic microkrystite with an off-central filled vesicle. (E) Phase map of spherule DGTS-S43, showing alkali feldspar (Afs), ilmenite (Ilm), siderite (Sid). (F) Orientation map of spherule DGTS-S43 in an inverse pole figure colour scheme, showing ilmenite relative to the z-direction of the map reference frame (IPFz) from the inset shown in (E). Stp = stilpnomelane.

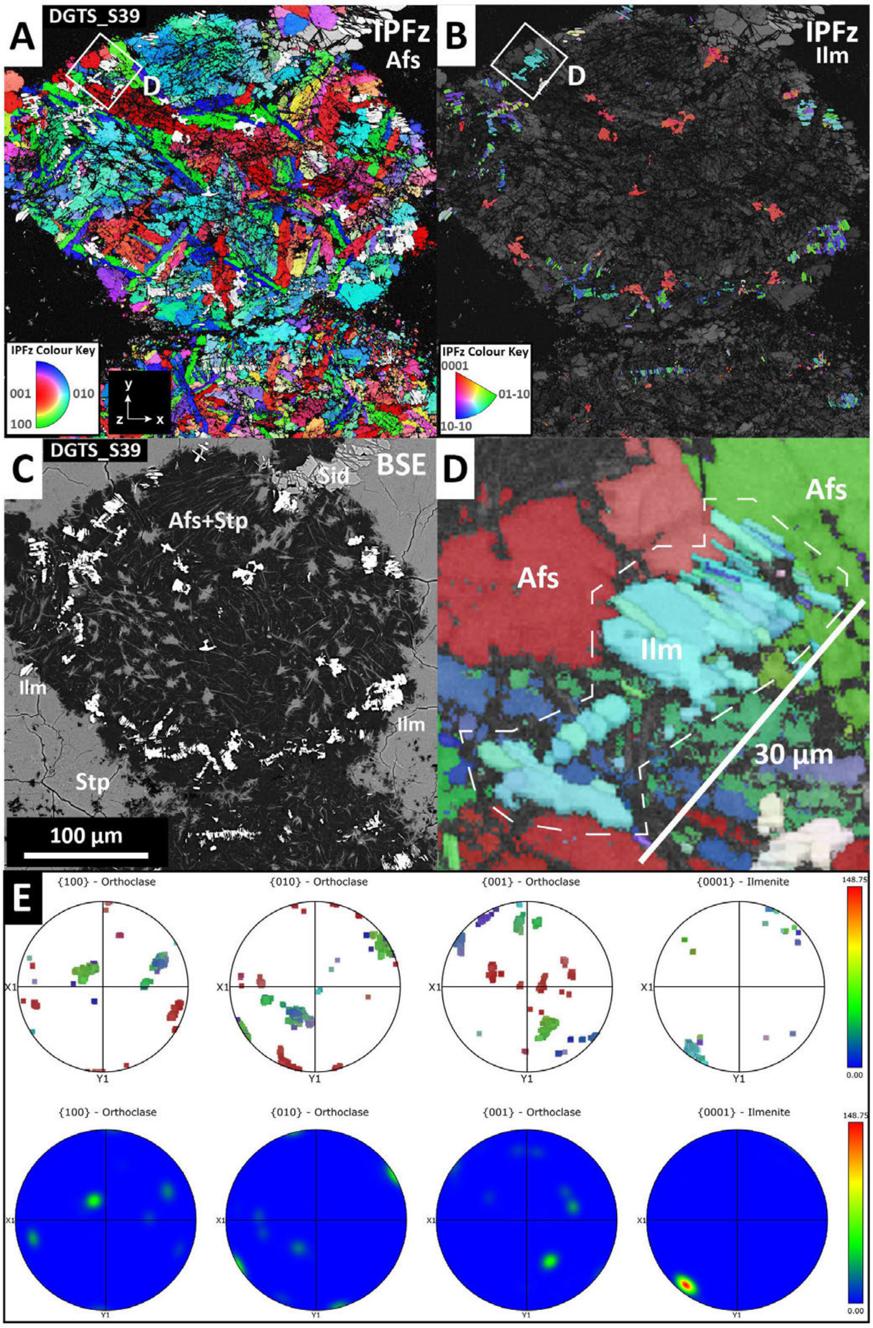

Figure 3.21: Comparison of crystal orientations of orthoclase and ilmenite in Dales Gorge feldspathic microkrystite DGTS-S39. (A) Orientation map in an inverse pole figure colour scheme, showing distribution of alkali feldspar relative to the z-direction of the map reference frame (IPFz). (B) Orientation map in an inverse pole figure colour scheme, showing distribution of ilmenite relative to the z-direction of the map reference frame (IPFz). (C) Backscattered electron image (BSE). (D) IPFz map showing both orthoclase and ilmenite from the insets in (A) and (B) to show the textural and orientation variation between alkali feldspar and an ilmenite array. (E) Pole figures for both alkali feldspar (orthoclase) and ilmenite from the outer dust rim. Ilmenite does not appear to share any crystallographic preferred orientation (CPO) or shape preferred orientation (SPO) with the surrounding alkali feldspar grains. The {0001} axis of ilmenite does not coincident with the low index poles in any surrounding alkali feldspar domains.

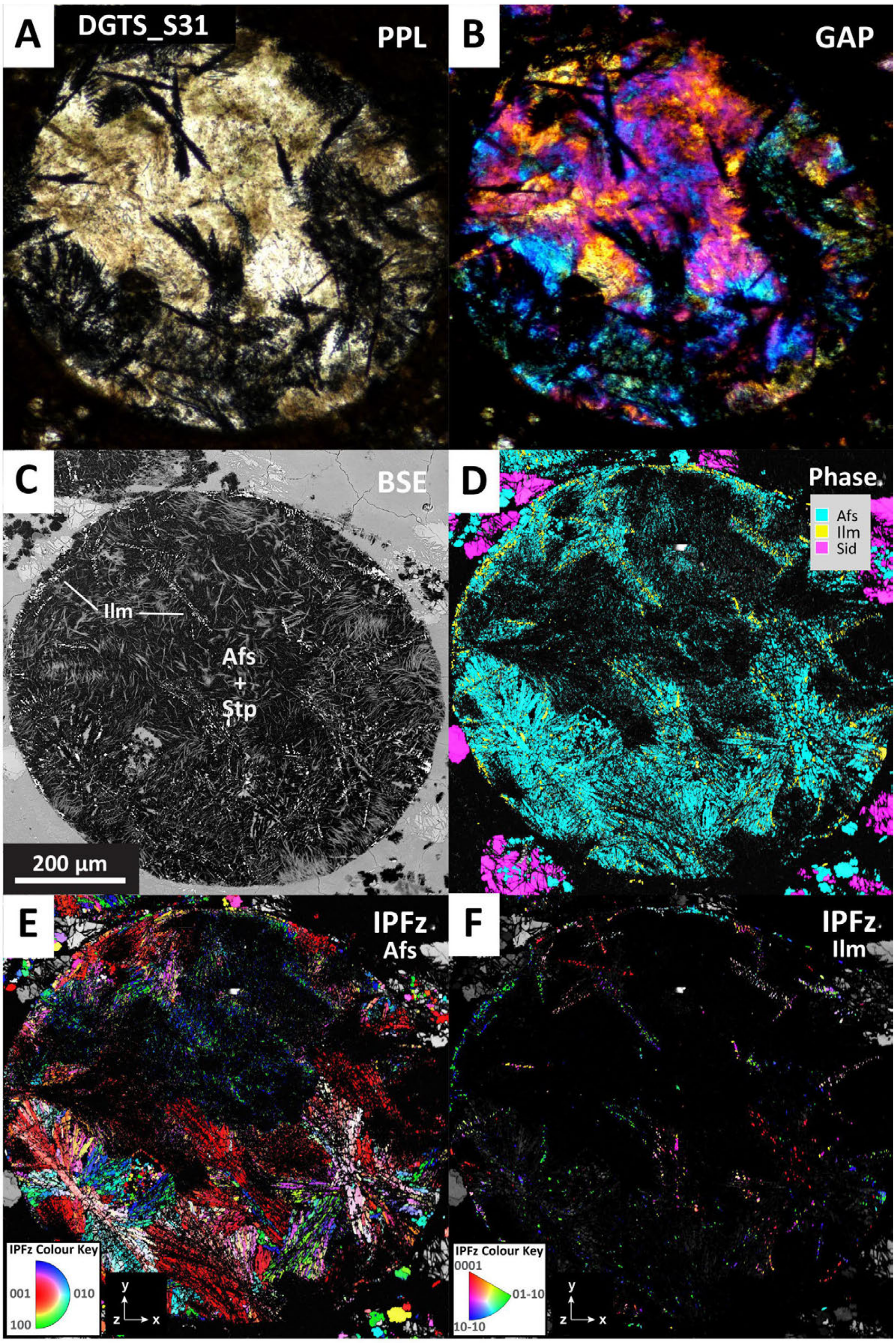

Figure 3.22: Images of radial-type DGSL spherule DGTS-S31, with fasciculate texture. (A) Plane polarised light image (PPL). Similarly bright regions in other feldspathic spherules typically indexed as alkali feldspar. Ilmenite grains are visible as black (opaque) arrays. (B) Gypsum accessory plate image (GAP). (C) Backscatter electron image (BSE). Ilmenite grains are visible as a bright phase. (D) Phase map; alkali feldspar (Afs), ilmenite (Ilm), siderite (Sid). Alkali feldspar only indexed where it is intergrown with ilmenite. (E) Orientation map in an inverse pole figure colour scheme, showing distribution of alkali feldspar relative to the z-direction of the map reference frame (IPFz). The fasciculate texture is visible in the lower left of the image. (F) Orientation map in an inverse pole figure colour scheme, showing distribution of ilmenite relative to the z-direction of the map reference frame (IPFz). Stp = stilpnomelane.

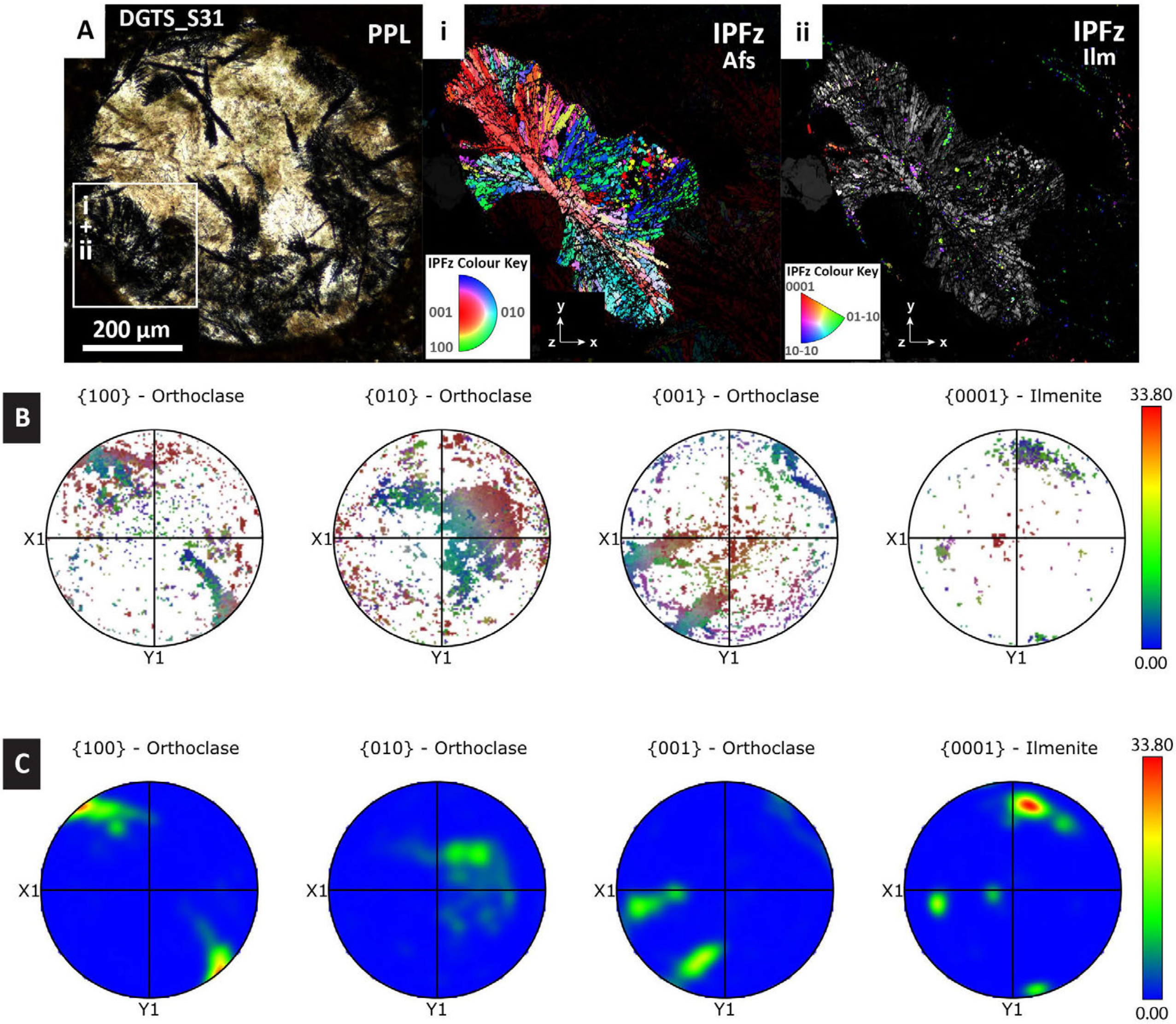

Figure 3.23: Comparison of crystal orientations of orthoclase and ilmenite in a fasciculate microstructure from Dales Gorge feldspathic microkrystite DGTS-S31. (A) Plane polarised light image. Insets show orientation maps in an inverse pole figure colour scheme, showing distribution of (i) alkali feldspar relative to the z-direction of the map reference frame (IPFz) and (ii) ilmenite (IPFz). Ilmenite locally shows a shape preferred orientation (SPO) with the surrounding alkali feldspar grains, as some ilmenite arrays are sub-parallel and appear to be intergrown with alkali feldspar. (B) Pole figures for both alkali feldspar (orthoclase) and {0001} ilmenite. Ilmenite does not appear to share a crystallographic preferred orientation (CPO) with alkali feldspar. The {0001} direction of ilmenite is not coincident with the low index poles in any surrounding alkali feldspar domains.

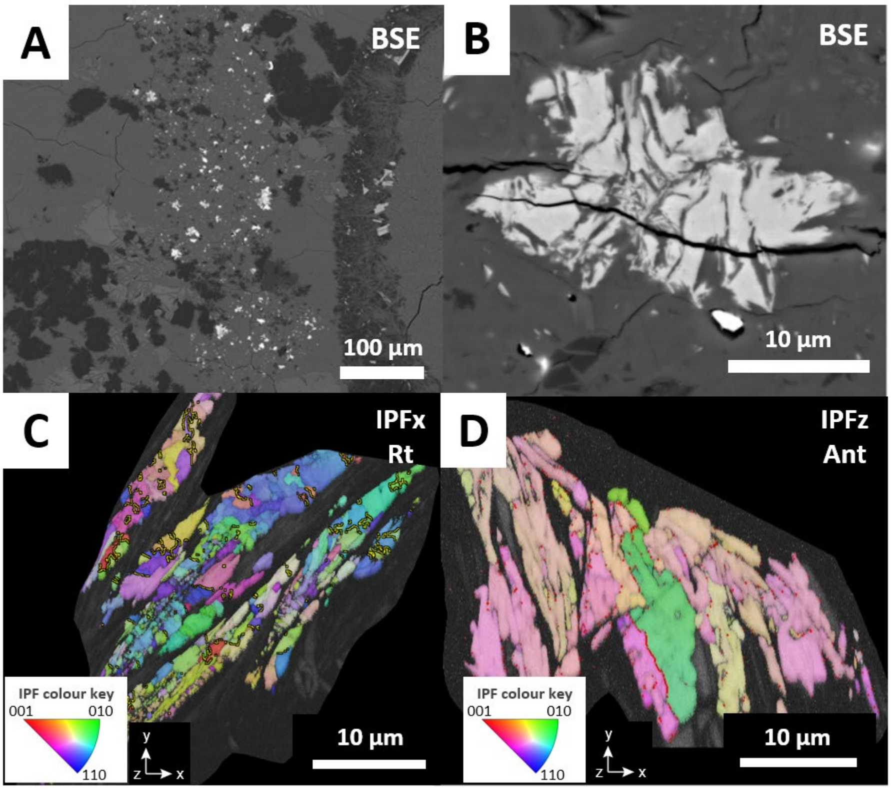

Figure 3.24: Examples of accessory minerals in Dales Gorge spherule layer (DGTS). (A) Backscattered electron image (BSE) of scattered zircon fragments in the Stp matrix. No zircons were observed within spherules. (B) BSE image of a typical zircon grain. All are anhedral fragments that appear to be metamict, as they yielded poor quality diffraction patterns during EBSD analysis. (C) Orientation map of polycrystalline rutile grain in an inverse pole figure colour scheme relative to the x-direction of the map reference frame (IPFx). (D) Orientation map of polycrystalline anatase grain in an inverse pole figure colour scheme relative to the z-direction of the map reference frame (IPFz).

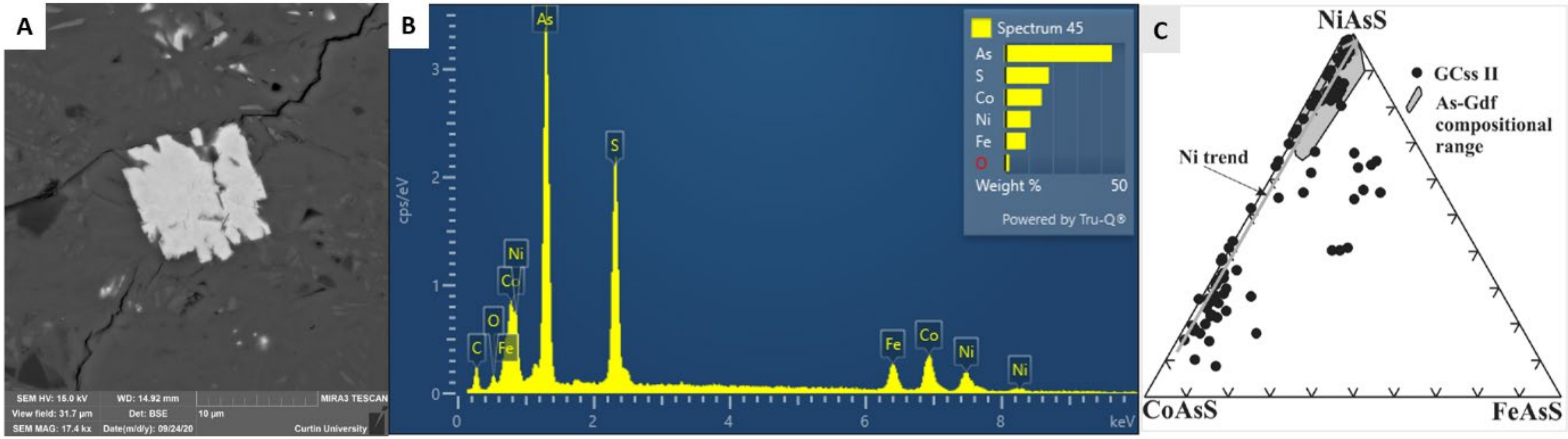

Figure 3.25: Examples of sulphide-sulfarsenides in Dales Gorge spherule layer (DGTS). (A) Backscattered electron image (BSE) of sulphide found within a zircon cluster. (B) Energy dispersive spectroscopy spectrum showing elements in the sulphide from (A). Note the prominent peaks for As, Ni and Co. (C) Possible composition of As-Co-Ni rich sulphides within Dale Gorge spherule layer (Fanlo et al., 2004).

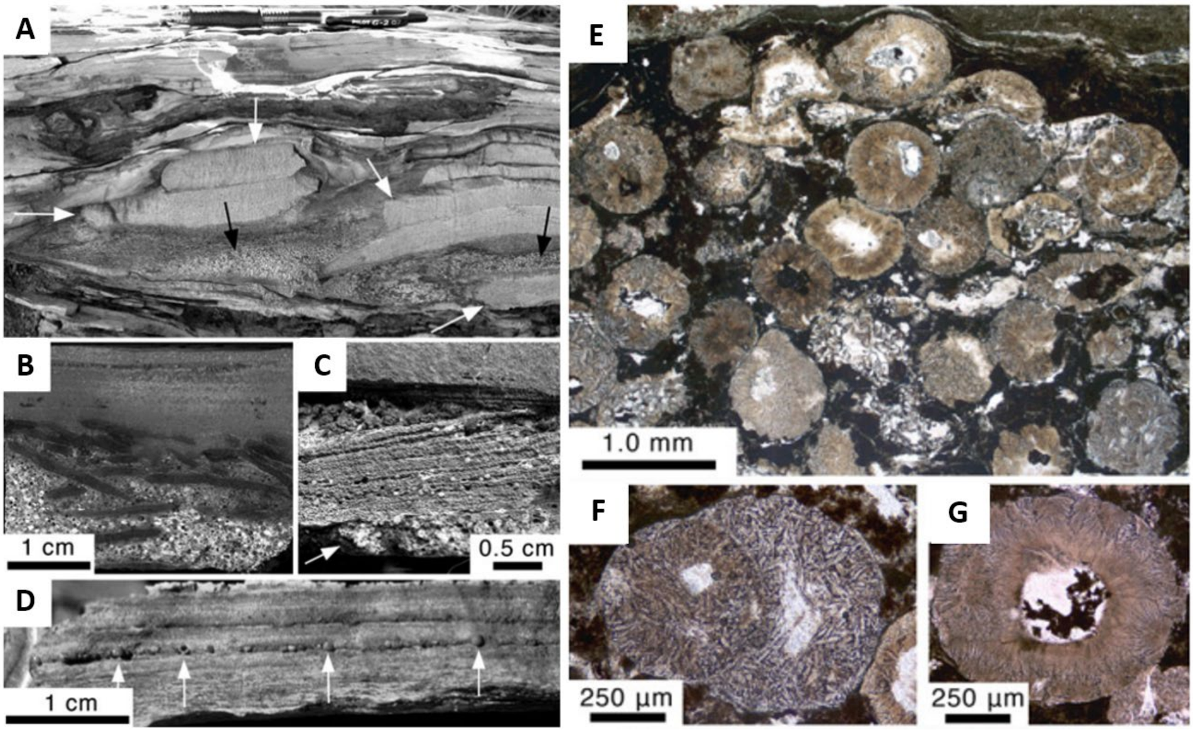

Figure 4.1: Published images of Bee Gorge spherule layer (BGSL) spherules. (A)-(D) Outcrop images of the Bee Gorge spherule layer. Black arrow in (A) and white arrows in (C) and (D) indicate layers with high concentrations of spherules. (E) Transmitted light image of Bee Gorge spherules. Note the high abundance of spherules, and shapes modified by compaction. Many spherules are in contact with other spherules, and some are sutured along contacts due to pressure solution and ductile deformation. The dark areas are groundmass, made up of oxidised ferroan carbonate and shale. (F) Example of an agglutinated (merged) spherule, suggested to form due to collision in flight. Both spherules having inwards-radiating alkali feldspar rims (brown acicular crystals) and quartz in the core. (G) Spherule with a circular cross-section, mineralogically and texturally similar to (F), with coarse quartz core (clear) and oxidised carbonate (dark) replacing the central vesicle (after Glass and Simonson, 2013).

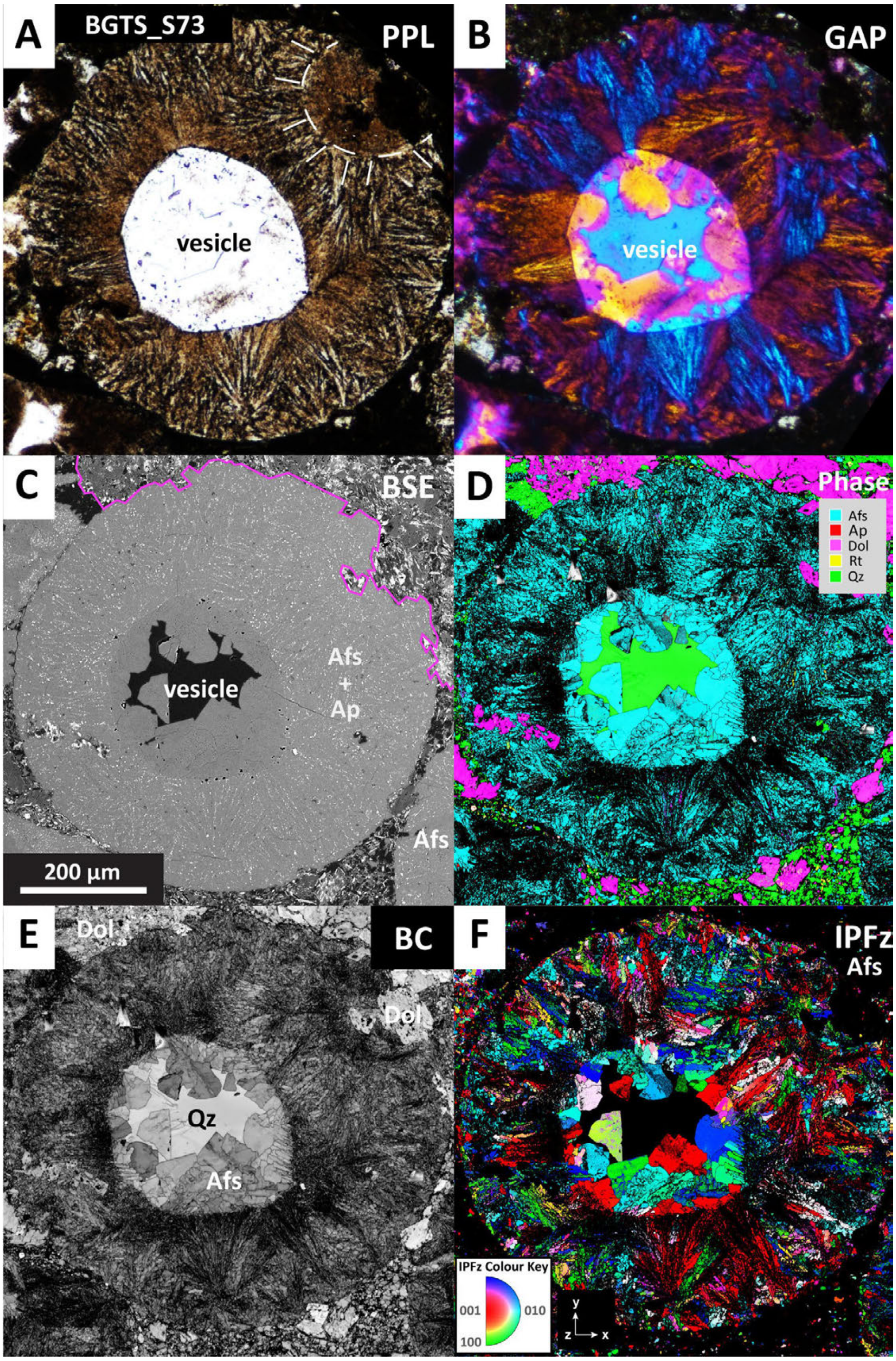

Figure 4.2: Images of radial-type BGSL spherule BGTS-S73. (A) Plane polarised light image (PPL), showing inward radiating alkali feldspar and a central filled vesicle. A large alkali feldspar spherulite is located in the upper right side of the spherule. (B) Gypsum accessory plate image (GAP). (C) Backscatter electron image (BSE). Apatite is visible as a bright phase within the spherule. (D) Phase map showing alkali feldspar (Afs), apatite (Ap), dolomite (Dol), Rutile (Rt) and Quartz (Qz). (E) Band contrast (BC) map. (F) Orientation map in an inverse pole figure colour scheme, showing distribution of alkali feldspar relative to the z-direction of the map reference frame (IPFz). Note the grain size and morphological difference between radial acicular alkali feldspar within the spherule, and the massive, polycrystalline alkali feldspar grains partially filling the central vesicle.

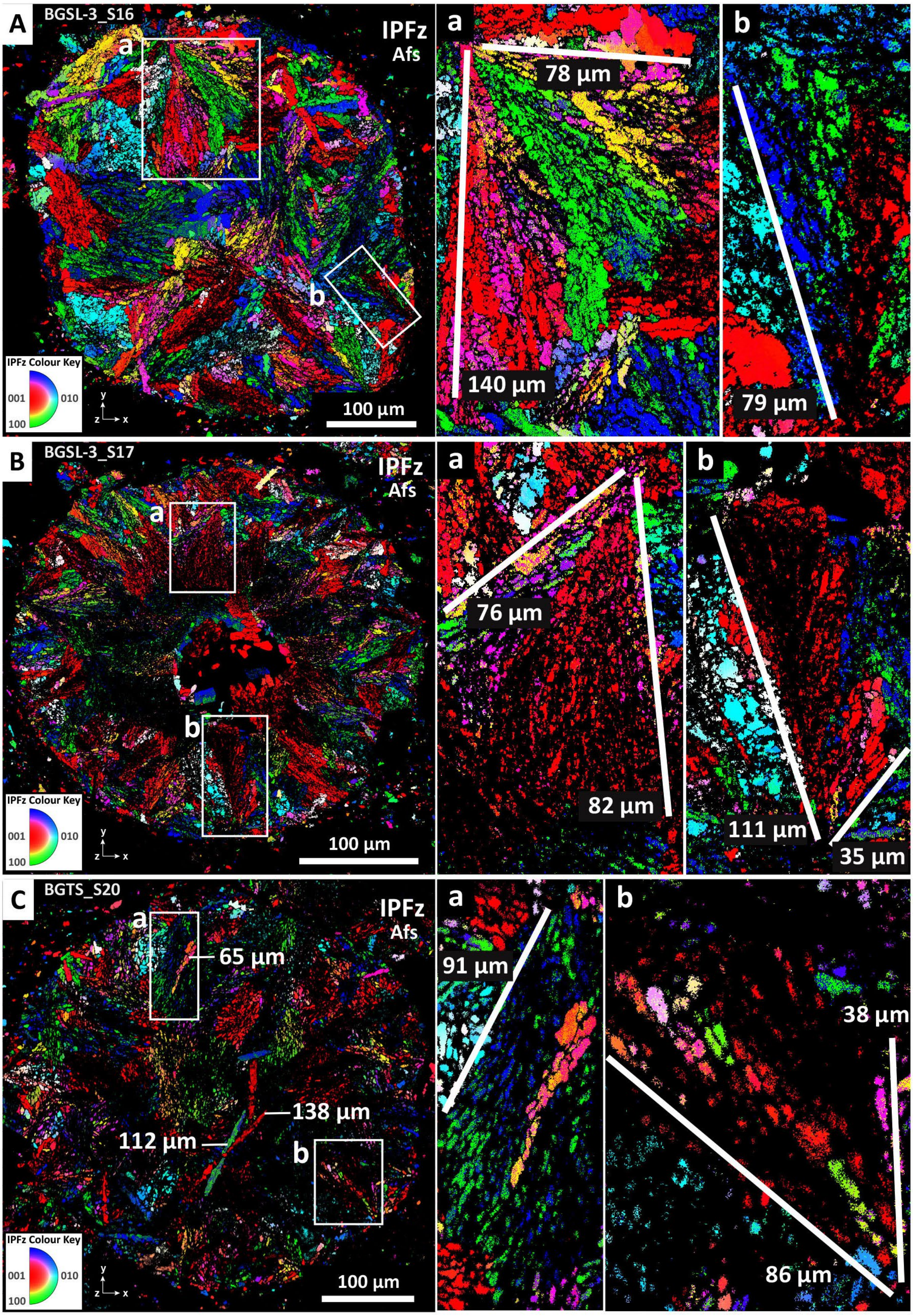

Figure 4.3: Orientation maps of alkali feldspar in radial-type Bee Gorge feldspathic microkrystites. (A) spherule BGSL-3_S16, a nearly fully crystalline spherule with fan-like spherulite microstructures. Inset boxes (a) and (b) show the lengths of spherulites. (B) Spherule BGSL-3_S17, with fan-like spherulite microstructures. Inset boxes (a) and (b) show the lengths of spherulites. (C) Spherule BGTS_S20. Inset boxes (a) and (b) show the lengths of spherulites. Note the segmented nature of alkali feldspar grains. All of the images are orientation maps in an inverse pole figure colour scheme, showing the distribution of alkali feldspar relative to the z-direction of the map reference frame (IPFz).

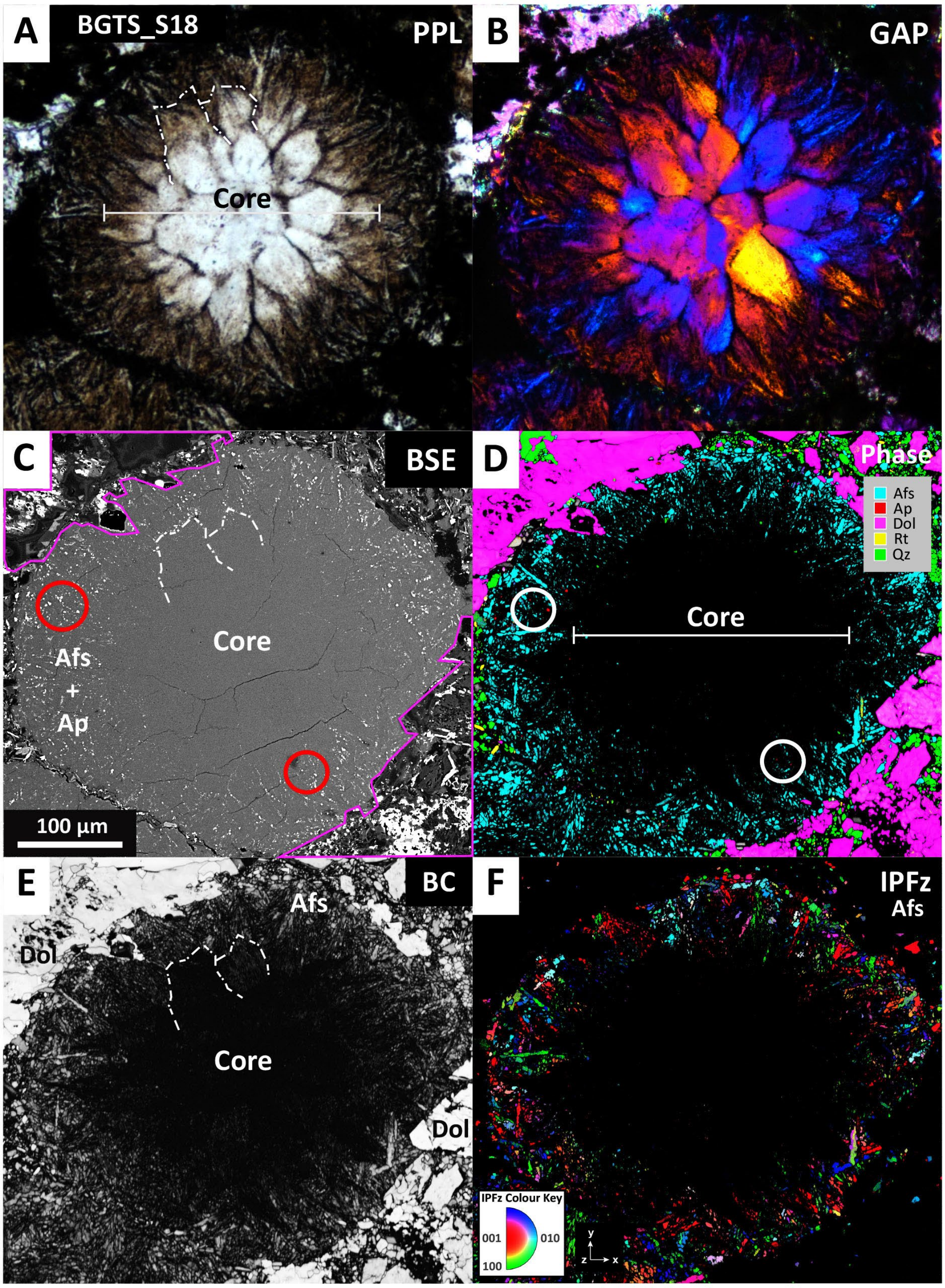

Figure 4.4: Images of radial-type BGSL spherule BGTS-S18, with a polygonal microstructure in the core. (A) Plane polarised light image (PPL), showing inward radiating alkali feldspar and a formerly glassy core. The core preserves a conspicuous polygonal microstructure. (B) Gypsum accessory plate image (GAP), showing the core is not isotropic. (C) Backscattered electron image (BSE). Apatite is visible as a bright phase within the spherule (red circles). (D) Phase map showing alkali feldspar (Afs), apatite (Ap), dolomite (Dol), Rutile (Rt) and Quartz (Qz). The core region is indicated, where no diffraction was detected. (E) Band contrast (BC) map, showing a dark core. (F) Orientation map in an inverse pole figure colour scheme, showing distribution of alkali feldspar relative to the z-direction of the map reference frame (IPFz).

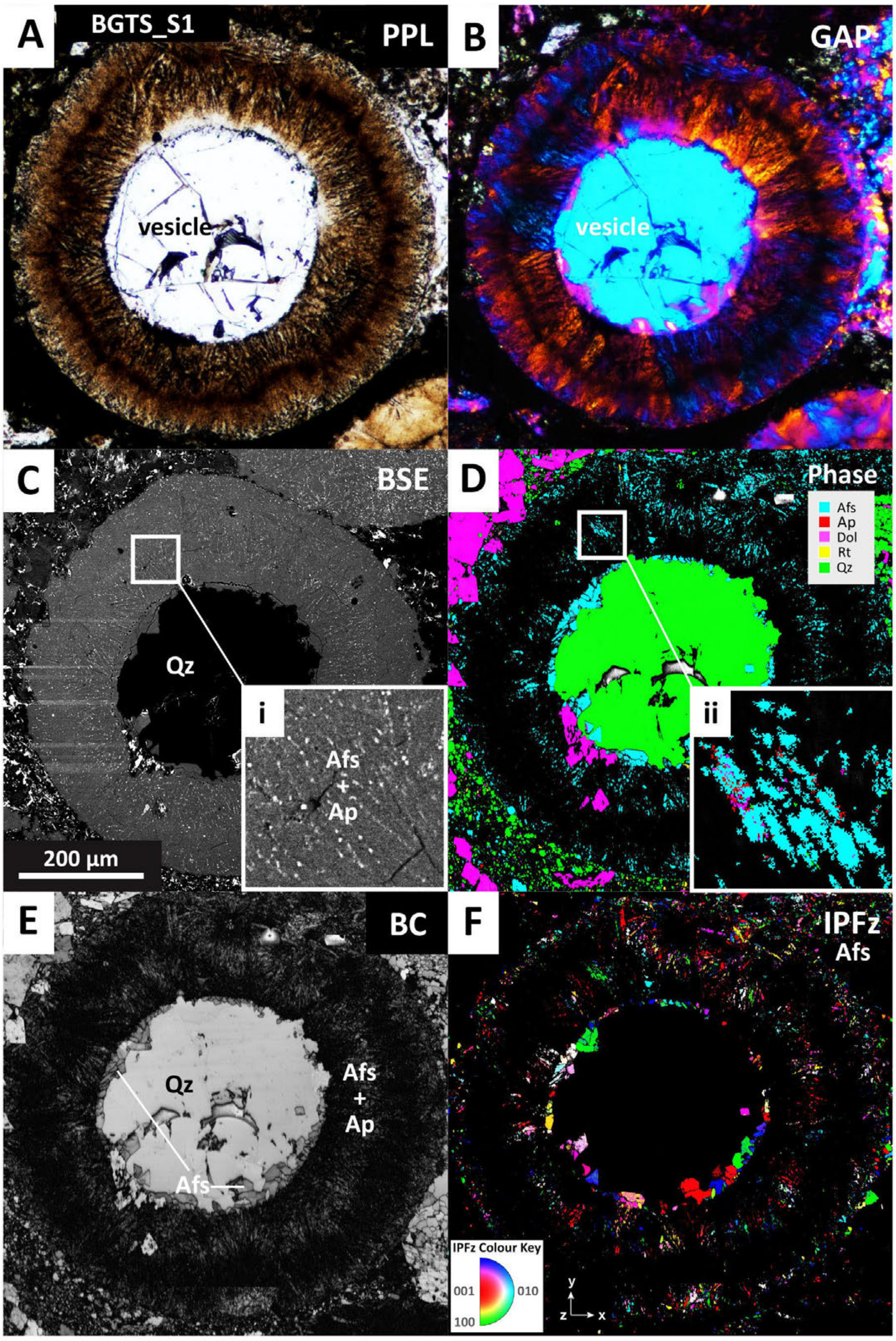

Figure 4.5: Images of radial-type BGSL spherule BGTS-S1, with a 'double rim' microstructure. (A) Plane polarised light image (PPL), showing two inward radiating alkali feldspar rims around the central filled vesicle, separated by a dark circular band. (B) Gypsum accessory plate image (GAP), showing the core is not isotropic. (C) Backscattered electron image (BSE). Apatite is visible as a bright phase within the spherule (see inset). Horizontal lines on the left side of the image are scan artifacts, and not part of the sample. (D) Phase map showing alkali feldspar (Afs), apatite (Ap), dolomite (Dol), Rutile (Rt) and Quartz (Qz). The core region is indicated, where no diffraction was detected. (E) Band contrast (BC) map, showing a dark core. (F) Orientation map in an inverse pole figure colour scheme, showing distribution of alkali feldspar relative to the z-direction of the map reference frame (IPFz). Two concentric and separated rings of radial acicular alkali feldspar grains are visible surrounding the central filled vesicle. A third ring of blocky alkali feldspar grains lines the wall of the filled vesicle.

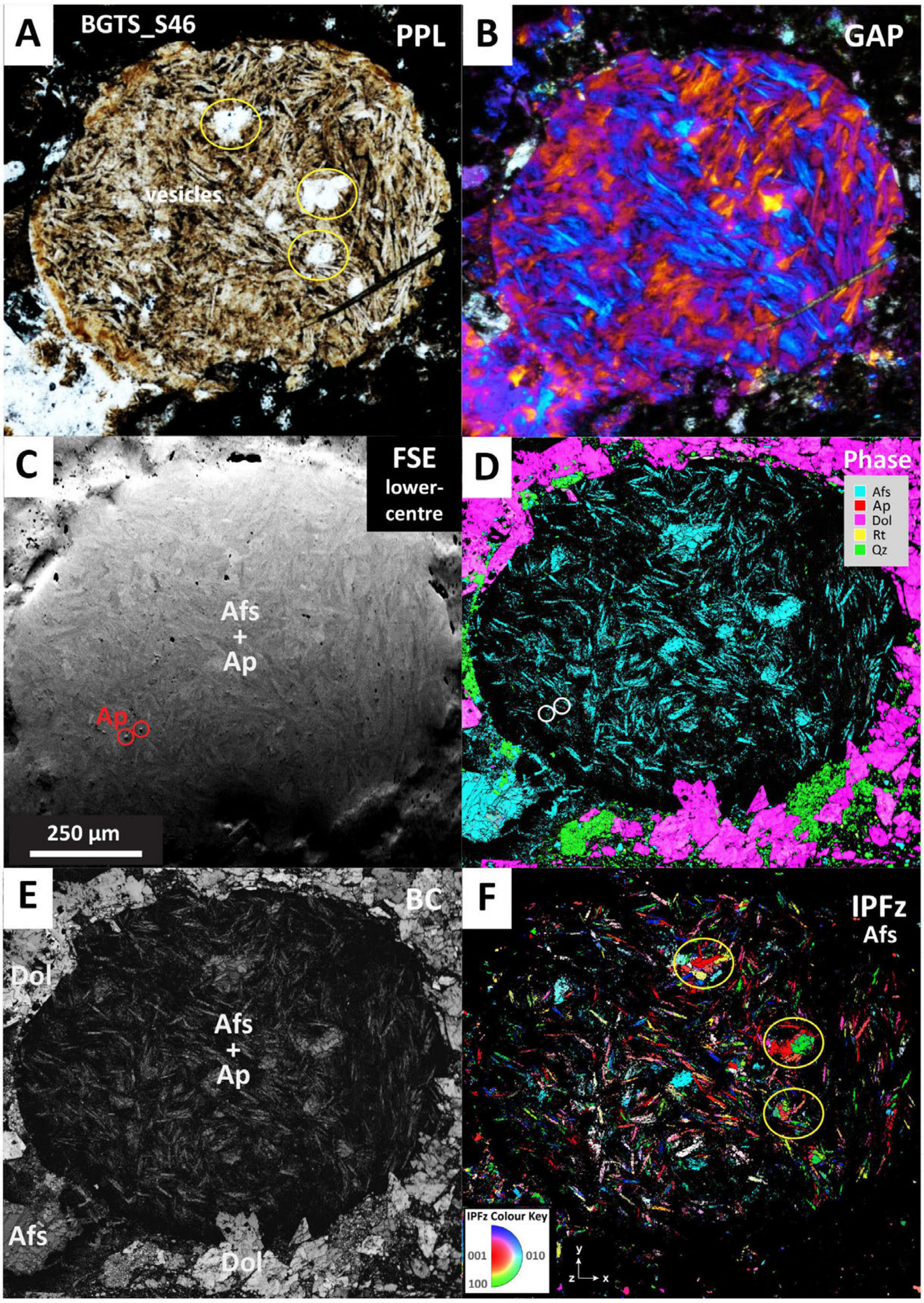

Figure 4.6: Images of random-type BGSL spherule BGTS-S46. (A) Plane polarised light image (PPL), showing prismatic alkali feldspar crystals, and several vesicles. (B) Gypsum accessory plate image (GAP). (C) Forescattered electron image (FSE). Apatite is visible as a bright phase within the spherule (see red circles). (D) Phase map showing alkali feldspar (Afs), apatite (Ap), dolomite (Dol), Rutile (Rt) and Quartz (Qz). Note the incursion of dolomite into the spherule margin. Note also the difference in grain size between feldspar within the spherule, and blocky feldspar in the matrix. (E) Band contrast (BC) map. (F) Orientation map in an inverse pole figure colour scheme, showing distribution of alkali feldspar relative to the z-direction of the map reference frame (IPFz). Note the difference in grain size of prismatic feldspar that makes up the majority of the spherule, and the block feldspar (circled) that occupies filled vesicles.

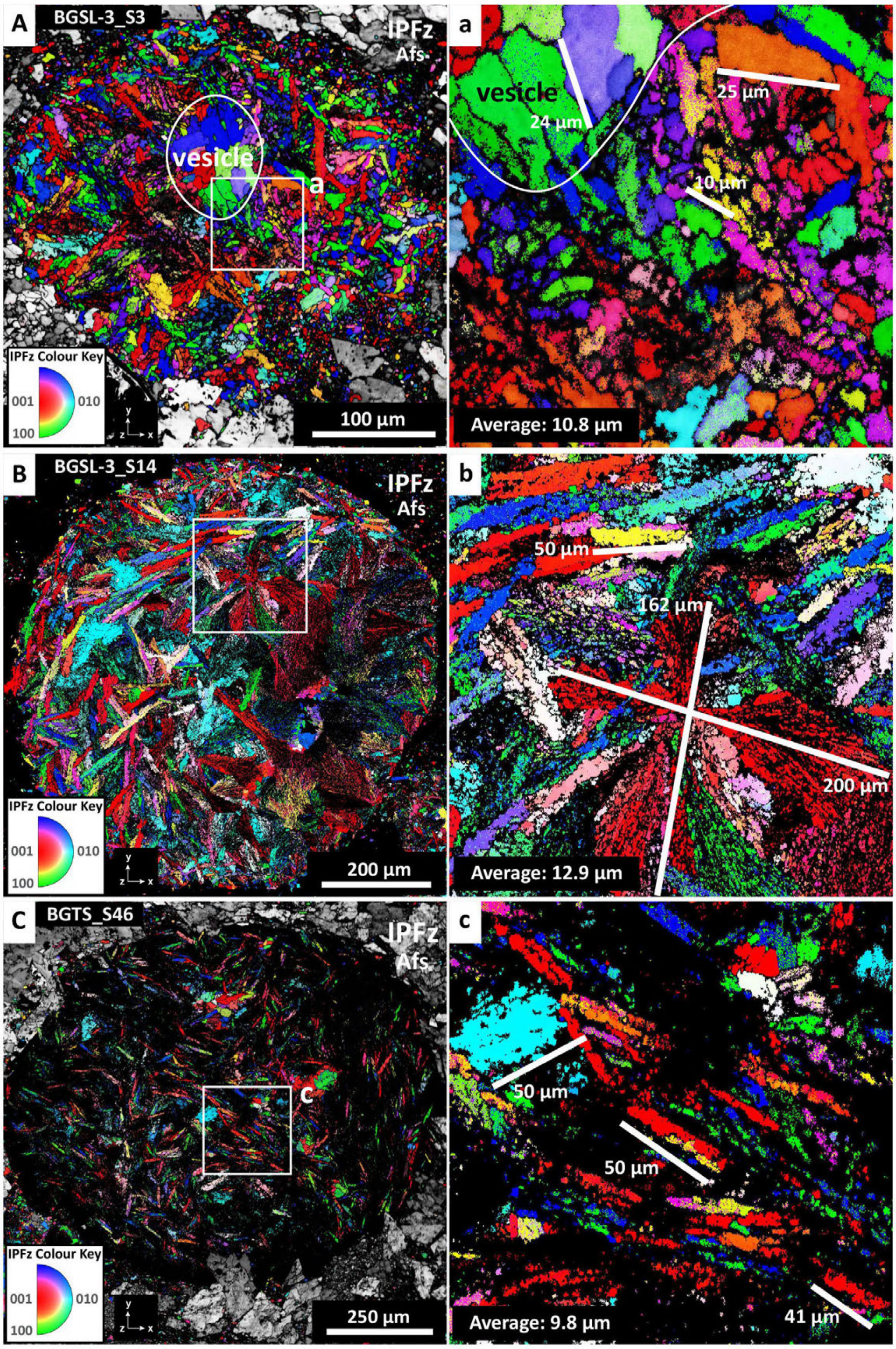

Figure 4.7: Orientation maps of alkali feldspar in random-type Bee Gorge feldspathic microkrystites. (A) spherule BGSL-3_S3, containing equant to prismatic feldspar crystals. Inset box (a) shows the textural variation between the prismatic feldspar grains that comprise the majority of the spherule, and the blocky, polycrystalline grains in the filled vesicle. (B) Spherule BGSL-3_S14, with prismatic feldspar crystals. The inset box (b) shows what appears to be a large spherulite. (C) Spherule BGTS_S46. Inset box (c) shows the lengths of prismatic feldspar crystals. All of the images are orientation maps in an inverse pole figure colour scheme, showing the distribution of alkali feldspar relative to the z-direction of the map reference frame (IPFz).

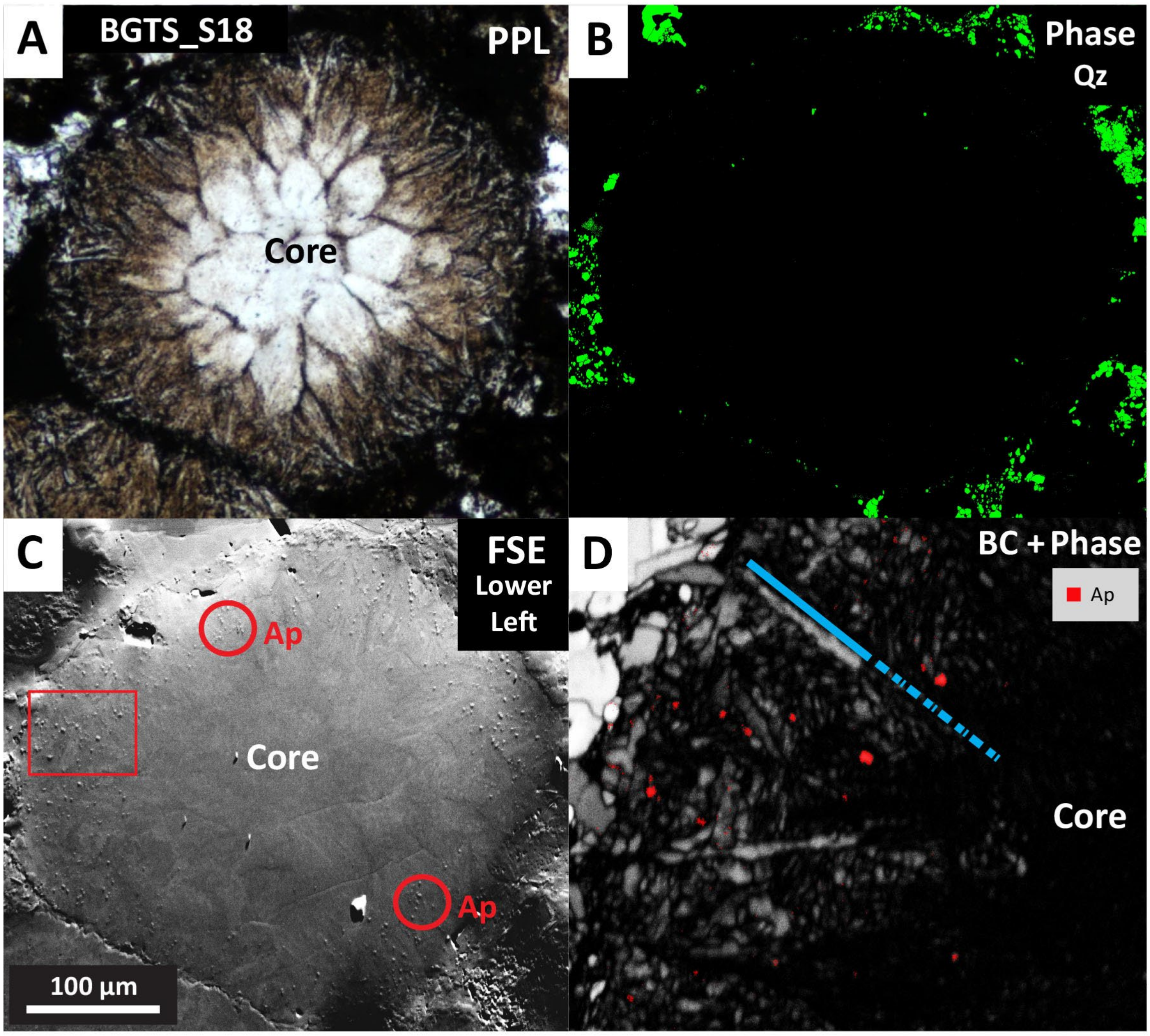

Figure 4.8: Images of radial-type BGSL spherule BGTS-S18, showing the textural relationship between various phases. (A) Plane polarised light image (PPL). (B) Phase map showing the distribution of Quartz (Qz), which defines the outline of the spherule. (C) Forescattered electron (FSE) image, which shows the location of apatite inclusions. Apatite is visible as a bright phase within the spherule (red circles). (D) Band contrast (BC) and phase map showing the location of Apatite (Ap) from the inset in (C) (see red square). Note how apatite only occurs where feldspar crystallised, and does not occur in the formerly glassy core.

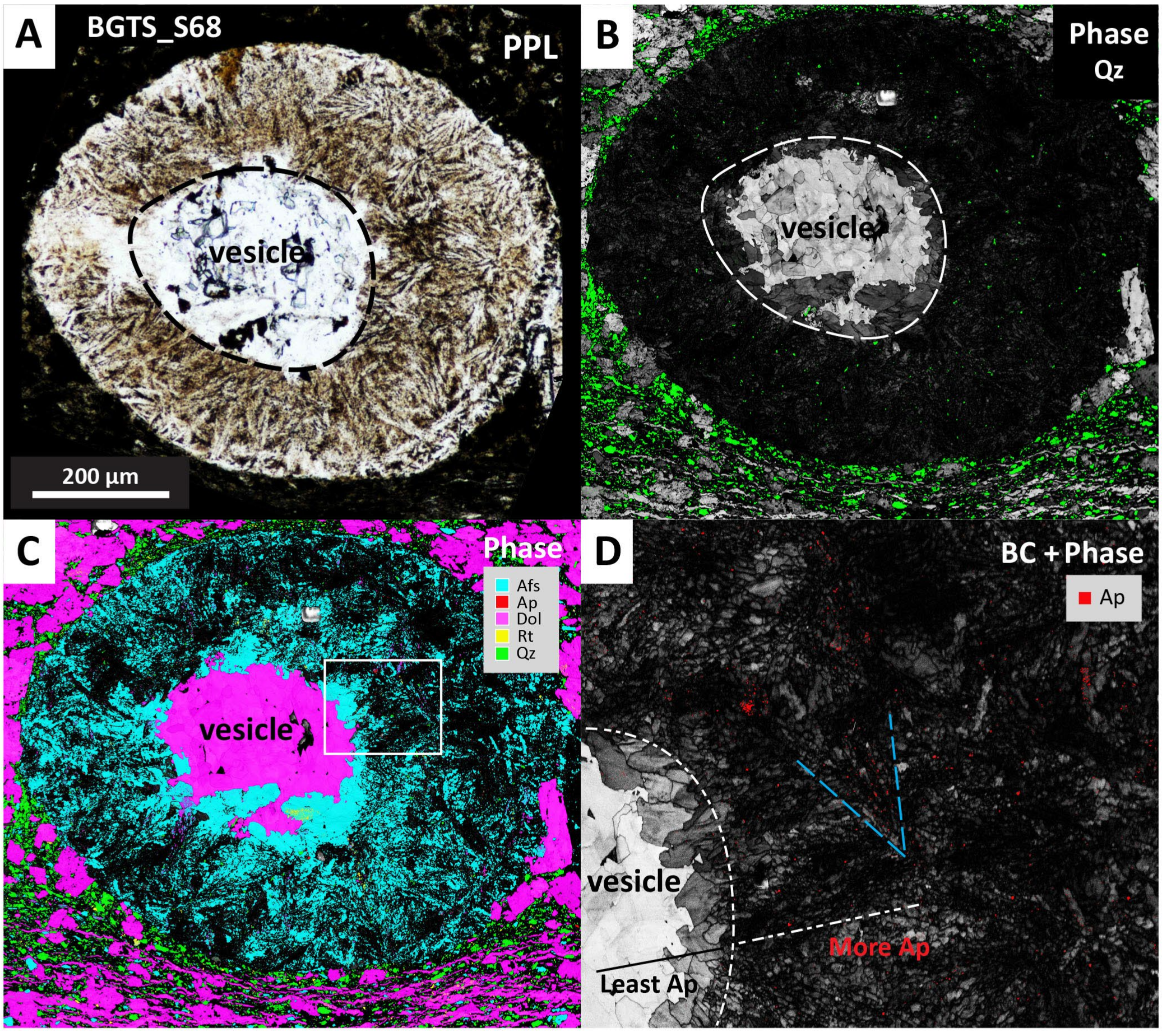

Figure 4.9: Images of radial-type BGSL spherule BGTS-S68, showing the textural relationship between various phases. (A) Plane polarised light image (PPL), showing radial acicular feldspar grains surrounding a central filled vesicle. (B) Combined Band contrast (BC) and phase map showing the distribution of Quartz (Qz), which defines the outline of the spherule, and reveals layering in the matrix. (C) Phase map showing alkali feldspar (Afs), apatite (Ap), dolomite (Dol), Rutile (Rt) and Quartz (Qz). The filled vesicle contains a rim of blocky alkali feldspar that later in-filled with dolomite. Note the presence of layering in the matrix is also defined by dolomite. (D) Band contrast (BC) and phase map showing the location of Apatite (Ap) from the inset in (C) (see white square). Note how apatite only occurs where feldspar crystallised, and does not occur in the filled vesicle.

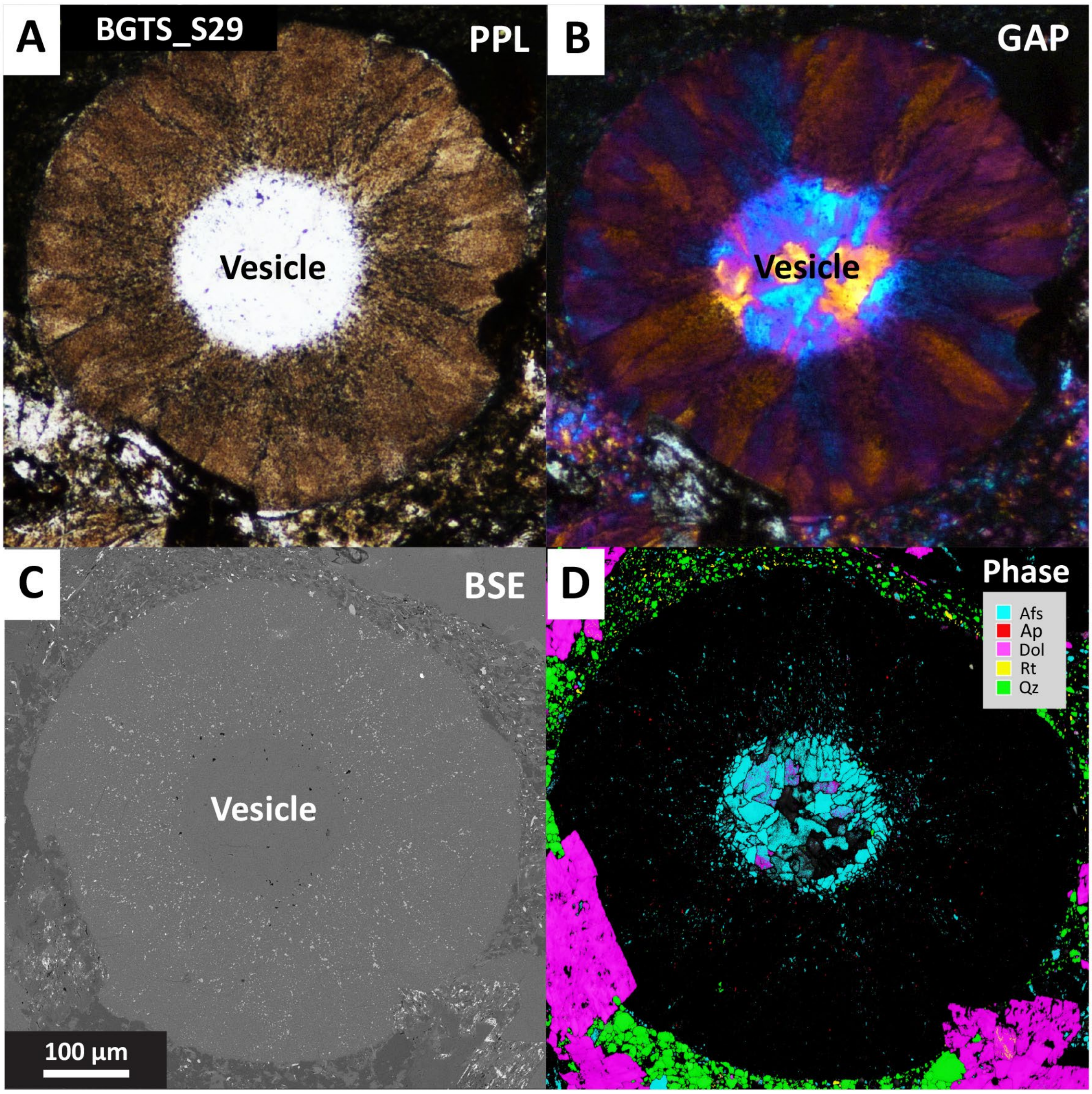

Figure 4.10: Images of radial-type BGSL spherule BGTS-S29, with a central filled vesicle. (A) Plane polarised light image (PPL), showing radial blocky feldspar grains surrounding the central filled vesicle. (B) Gypsum accessory plate (GAP) image showing the spherule is not isotropic. (C) Backscattered electron image (BSE). (D) Phase map showing alkali feldspar (Afs), apatite (Ap), dolomite (Dol), Rutile (Rt) and Quartz (Qz). Most of the radial blocky feldspar grains did not yield sufficient diffraction patterns to index during EBSD analysis. The filled vesicle consists of polycrystalline feldspar. Note the incursion of dolomite rhombs into the margin of the spherule.

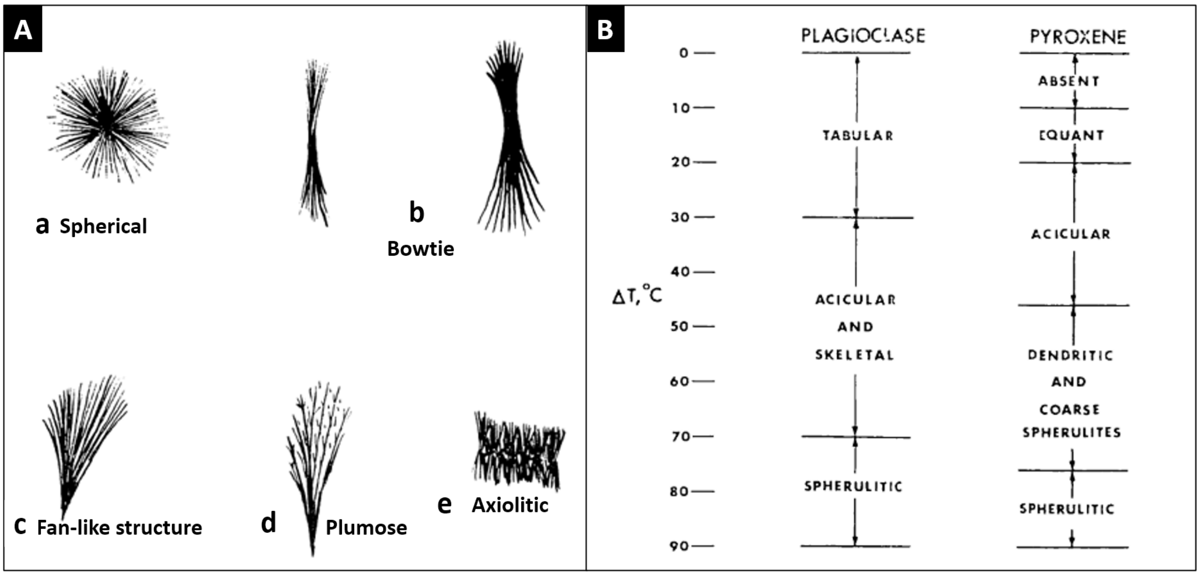

Figure 5.1: Morphologies of experimentally quenched plagioclase grains in basalt (Lofgren, 1974). (A) Basic spherulitic textural developments formed by plagioclase during isothermal crystallisation of basaltic melts. (B) Schematic diagram representing plagioclase and pyroxene crystal morphologies associated with degree of supercooling (ΔT).

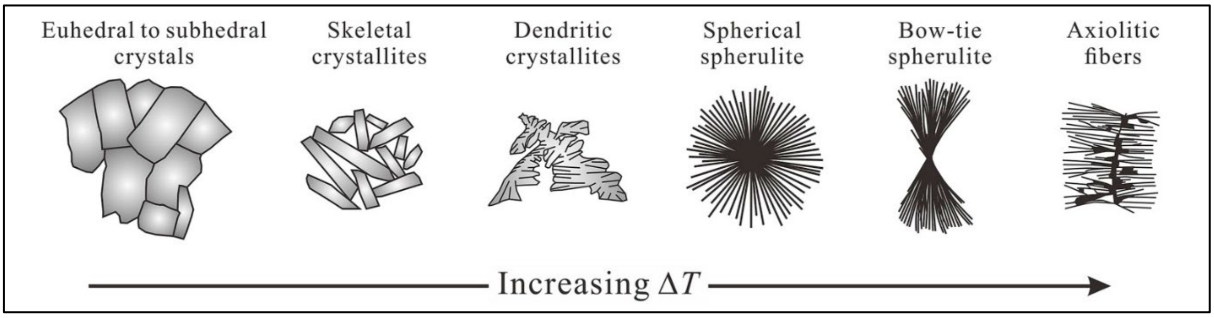

Figure 5.2: Morphologies of experimentally quenched plagioclase grains as a function of supercooling (ΔT). The diagram shows the evolution of crystal morphology with increasing ΔT to the right (Zheng et al., 2018).

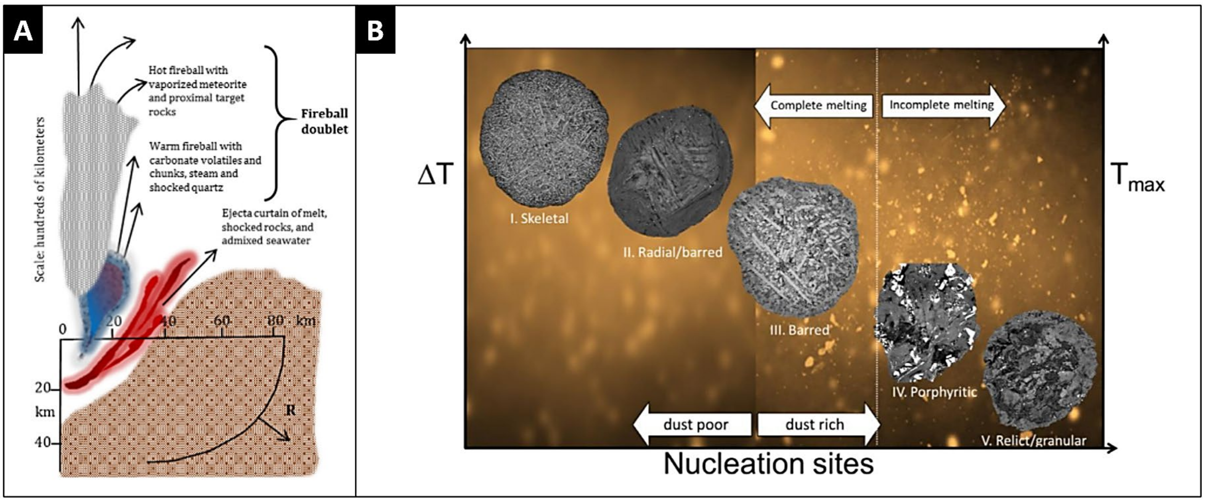

Figure 5.3: Models for the formation of distal spherules from the K–Pg boundary formed by the Chicxulub impact (Belza et al., 2017). (A) Vapor plume model that illustrate processes occurring in the early stage of the Chicxulub vapor plume. The vapor plume is made up of a 'fireball doublet', which is comprised of a hot fireball with vaporised target rock and meteorite (grey) and a warm fireball, with volatiles and shocked materials (blue). (B) Schematic diagram relating the density of nucleation sites in spherules with the abundance of dust and degree of supercooling (ΔT).

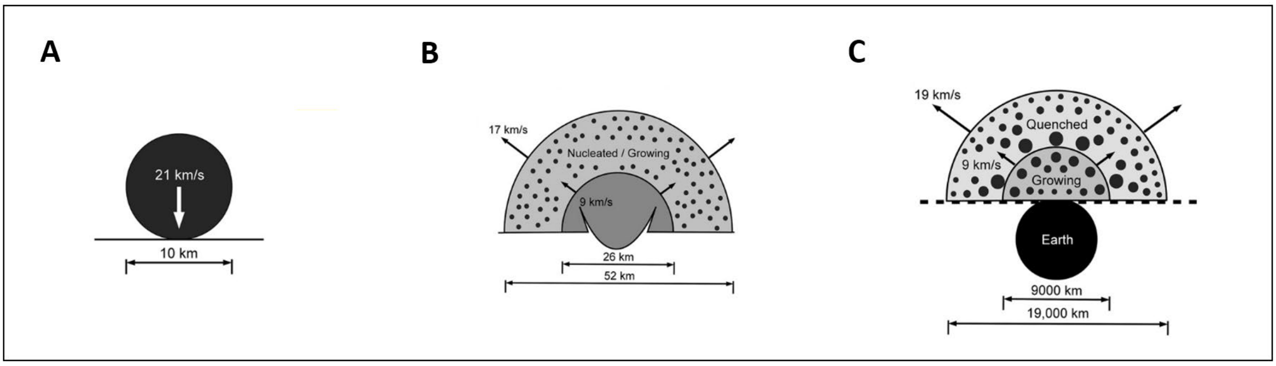

Figure 5.4: Numerical model results of vapor plume formation (Johnson and Melosh, 2012). (A) Illustration of a 10 km diameter impactor hitting with a velocity of 21 km/s. (B) Rapid growth of the initial vapor cloud and expansion over time. Regions of nucleation and growth of spherules are indicated. (C) The vapor plume now contains zones where spherules have quenched (outer) and zones where spherules are still growing (inner). Note the size of the vapor plume relative to Earth in (C).

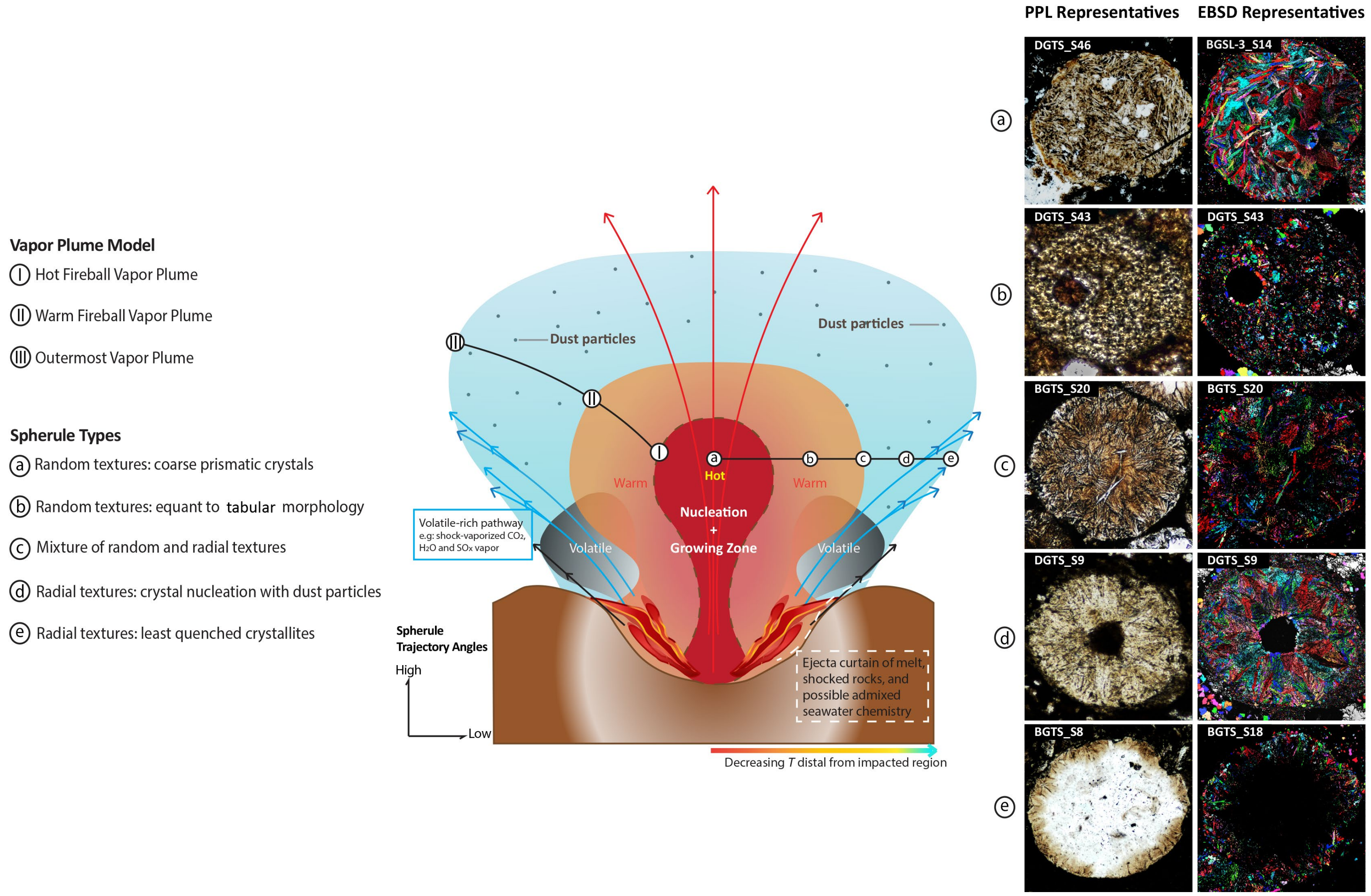

Figure 5.5: Proposed vapor plume model to explain the formation of feldspathic microkrystites analysed in this study. The vapor plume is featured as containing three regions: (i) the hot fireball, containing vaporised target rock and projectile, (ii) the warm fireball, containing volatiles, and (iii) the outermost region, where temperature decreases rapidly. Dust particles are featured to be present between the two outermost regions, (ii) and (iii). Representative plane polarised light images and orientation images of five spherule types are shown that are interpreted to characterise spherule formation at progressively distal distances from the centre of the hot fireball. These include: (a) Proximal spherules with random-type textures consisting of coarse prismatic feldspar crystals formed in the hot fireball; (b) Proximal spherules with random-type textures consisting of equant to tabular feldspar crystals formed in the warm fireball; (c) Intermediate spherules with a mixture of random-type and radial-type textures consisting of tabular feldspar and spherulitic feldspar formed near the boundary of the warm fireball and the outermost region; (d) Distal spherules with radial-type textures whose nucleation was triggered by impinging dust particles in the outermost regions; (e) Distal spherules with radial-type textures formed at the edge of the vapor plume that preserve quenched (formerly) glassy cores due to incomplete crystallisation.

List of Tables

Table 1: Summary of Radiometric ages of studied Archean spherule suites.

Spherule Layer	Radiometric Age (Ma)	Summary of Description	Reference
DGSL	2479	Tuff zicon U-PB result (SHRIMP)	Trendall et al. (1998); Thorne and Trendall (2001)
	2490	Assumption between closest dates from the U-Pb SHRIMP results	Trendall et al. (2004); Glikson and Allen (2004); Sweeney and Simonson (2008)
	2495 ± 16	Tuff zircon U-Pb result (SHRIMP), ~10m below DGSL, older tuff in DS2 macroband	Trendall et al. (2004)
	2504 ± 5	Tuff zircon U-Pb result (SHRIMP), ~60m below DGSL, older tuff in Mt. McRae Shale	Rasmussen et al. (2005)
	2481 ± 4	Tuff zircon U-Pb result (SHRIMP), ~30m above DGSL,younger tuff in DS9 macroband	Trendall et al. (2004)
	2461 ± 6	Tuff zircon U-Pb result (SHRIMP), ~65m above DGSL,younger tuff in DS13 macroband	Trendall et al. (2004)
	2463 ± 5	Tuff zircon U-Pb result (SHRIMP), ~110m above DGSL,younger tuff in Whaleback Shale Member	Trendall et al. (2004)
BGSL	2561 ± 8	Tuff zircon U-Pb result (SHRIMP), ~70m below BGSL	Simonson et al. (1993); Trendall et al. (1998)
	2504±5	Tuff zircon U-Pb result (SHRIMP), ~135m above BGSL	Rasmussen et al. (2005)
	2541 +18/-15	Direct dating on carbonate host (Pb-Pb)	Woodhead et al. (1998)
	2565 ± 9	Possibly reworked zircon crystals, extracted from BGSL	Trendall et al. (2004)
	2540	Assumption between two closest dates from the U-Pb SHRIMP results	Glass and Simonson (2013)

List of Tables (cont.)

Table 10: EBSD analytical conditions for Dales Gorge spherules based on spherule size

Spherule Number	Spherule Diameter (µm)	Step Size Resolution (nm)	Exposure Time (ms)	Aquisition Time (hours)
DGTS_S28	243	200	10	26
DGTS_S24	280	200	7.5	6
DGTS_S8	300	180	10	11.5
DGTS_S46	300	170	10	12.1
DGTS_S72	320	150	10	15.2
DGTS_S39	325	180	10	21.8
DGTS_S22	360	180	10	automated
DGTS_S40	360	180	10	21.8
DGTS_S68	360	180	10	15.1
DGTS_S49	368	200	10	14.2
DGTS_S30	390	150	10	25.6
DGTS_S6	393	215	10	11.5
DGTS_S43	430	140	8	20
DGTS_S27	445	200	10	26
DGTS_S18	510	170	5.5	15.8
DGTS_S9	550	230	8	17.5
DGTS_S32	600	250	10	48.1
DGTS_S2	610	180	10	41
DGTS_S11	650	200	8	24.5
DGTS_S21	700	180	10	automated
DGTS_S1	745	300	10	21
DGTS_S31	776	220	10	38.6
DGTS_S29	911	240	10	39
DGTS_S5	932	250	5	23.3
DGTS_S70	1070	230	5	automated

Table 19: Summary of existing classification schemes for Archean spherule horizons that involved DGSL description.

Sweeney and Simonson (2008) Classification Scheme		**Krull-Davatzes et al. (2015) Classification Scheme**	
Spherule Category	**Description**	**Spherule Composition**	**Description**
Radial	Contains acicular to laths of alkali feldspar, occurred entirely in spherules, radiating inwards from spherule boundaries	**Radial alkali feldspar**	Comprised of nearly pure alkali feldspar, showing quench textures (spherulitic features)
Random	Randomly-oriented/weakly aligned alkali feldspar laths	**Randomly oriented alkali feldspar**	Contained almost fully of random alkali feldspar crystallites;near-perfect preservation of alkali feldspar quench textures and occurrence of NiS and ilmenite within crystallites (Glikson and Allen, 2004)
Rimmed	Consists stilpnomelane core; alkali feldspar in rim performs random-radial textures	**Mixed Composition**	An incomplete mix of compositional types within spherule (differential alteration), including botryoidal rims
Massive	Spherule lacks alkali feldspar; contains entirely stilpnomelane; some have vesicles	**Al-rich Massive**	Phyllosilicate mineral=stilpnomelane in DGSL
		Non-Al Massive	Spherules are replaced with quartz or calcite, interpreted as altered from a glassy composition; absent in DGSL
Miscellaneous	Contains largely of stilpnomelane without spherule rim, might preserve random alkali feldspar laths, showing internal pattern (swirling or flow banding features)	**Miscellaneous**	Not easily classified into any of the other categories
Indeterminate	Internal textures are found largely obscured by fine opaque inclusions, difficult identifying primary features of spherules	no equivalent categoy involved	
no equivalent category involved		**Compositional Layering**	Spherules with interior cavities that have been replaced by quartz or calcite; cement or that have multiple concentric layers or differing composition, often ringed with Fe- or Ti-oxide along interior division
		Barred	Pseudomorphs of barred olivine, absent in DGSL

Table 28: Summary of Dales Gorge spherules categorisation under transmitted light observation based on Sweeney and Simonson (2008) and Krull-Davatzes et al. (2015) classification schemes.

Spherule Category	***Descriptions***	**Characteristics**							
		Alkali Feldspar Crystal Shapes			**Other Interior Features**			**Botryoidal Rim**	**Merged Spherules**
		Fibrous-Acicular (Fans)	***Prismatic Laths (Non-Fan)***	***Equant-Tabular (Non-Fan)***	**Quench Texture/ Spherulitic Growth**	**Vesicle Shapes**			
						Oval-Rounded-Perfect Circular	***Concave***		
Radial n=(42/80)	Spherules with alkali feldspar fans, radiating inwards from spherule boundaries	42	-	-	8	10	4	-	2
Glass core n=(16/80)	Spherule interior with partial to un-crystalline core; alkali feldspar can perform random-radial textures internally	13	-	3	-	4	2	3	3
Random n=(19/80)	Spherules preserved alkali feldspar laths with random orientations	-	7	15	-	5	2	-	3
Miscellaneous n=(3/80)	Unable to be classified into any of the other categories	-	-	-	-	-	-	-	-

Table 37: Summary of Dales Gorge spherule composition with crystallinity in percentage.

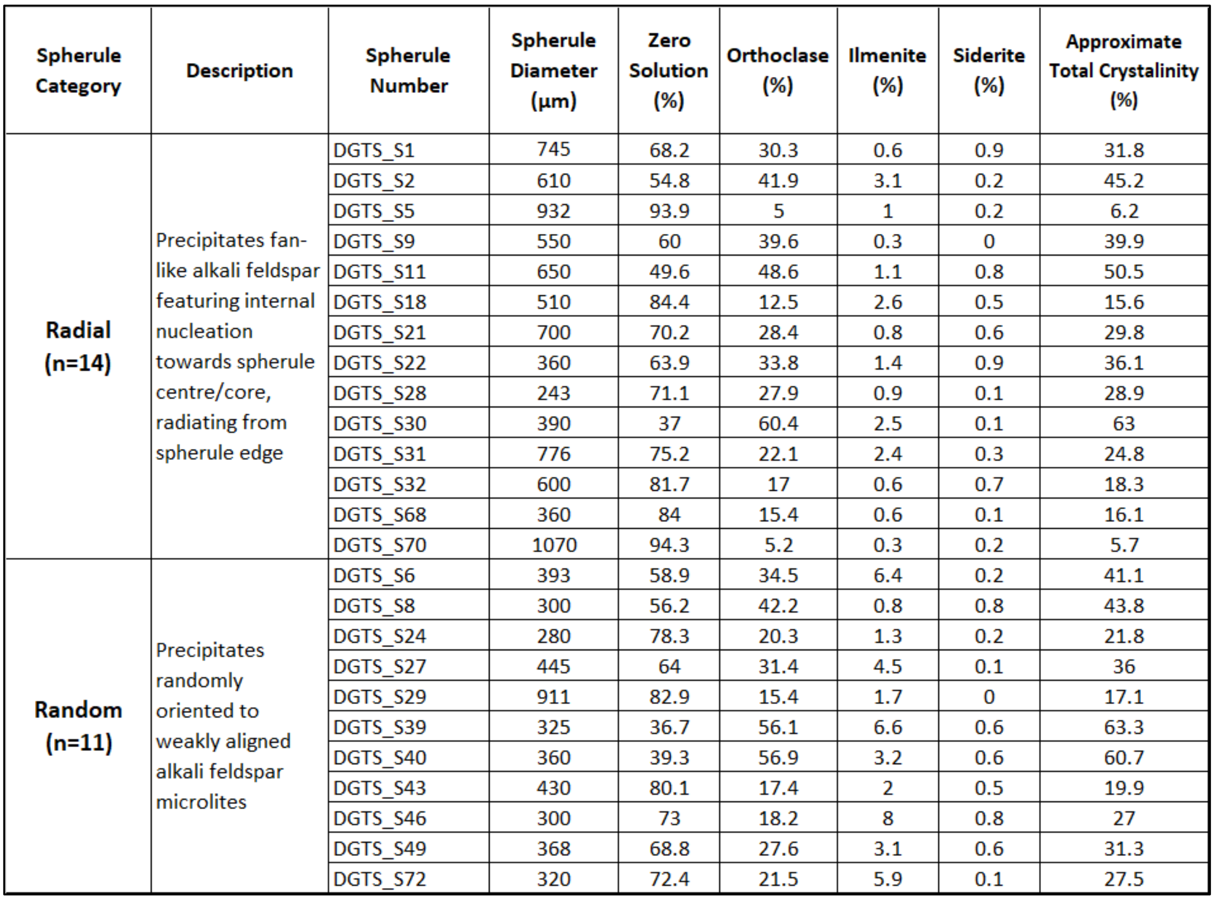

Spherule Category	Description	Spherule Number	Spherule Diameter (µm)	Zero Solution (%)	Orthoclase (%)	Ilmenite (%)	Siderite (%)	Approximate Total Crystalinity (%)
Radial (n=14)	Precipitates fan-like alkali feldspar featuring internal nucleation towards spherule centre/core, radiating from spherule edge	DGTS_S1	745	68.2	30.3	0.6	0.9	31.8
		DGTS_S2	610	54.8	41.9	3.1	0.2	45.2
		DGTS_S5	932	93.9	5	1	0.2	6.2
		DGTS_S9	550	60	39.6	0.3	0	39.9
		DGTS_S11	650	49.6	48.6	1.1	0.8	50.5
		DGTS_S18	510	84.4	12.5	2.6	0.5	15.6
		DGTS_S21	700	70.2	28.4	0.8	0.6	29.8
		DGTS_S22	360	63.9	33.8	1.4	0.9	36.1
		DGTS_S28	243	71.1	27.9	0.9	0.1	28.9
		DGTS_S30	390	37	60.4	2.5	0.1	63
		DGTS_S31	776	75.2	22.1	2.4	0.3	24.8
		DGTS_S32	600	81.7	17	0.6	0.7	18.3
		DGTS_S68	360	84	15.4	0.6	0.1	16.1
		DGTS_S70	1070	94.3	5.2	0.3	0.2	5.7
Random (n=11)	Precipitates randomly oriented to weakly aligned alkali feldspar microlites	DGTS_S6	393	58.9	34.5	6.4	0.2	41.1
		DGTS_S8	300	56.2	42.2	0.8	0.8	43.8
		DGTS_S24	280	78.3	20.3	1.3	0.2	21.8
		DGTS_S27	445	64	31.4	4.5	0.1	36
		DGTS_S29	911	82.9	15.4	1.7	0	17.1
		DGTS_S39	325	36.7	56.1	6.6	0.6	63.3
		DGTS_S40	360	39.3	56.9	3.2	0.6	60.7
		DGTS_S43	430	80.1	17.4	2	0.5	19.9
		DGTS_S46	300	73	18.2	8	0.8	27
		DGTS_S49	368	68.8	27.6	3.1	0.6	31.3
		DGTS_S72	320	72.4	21.5	5.9	0.1	27.5

Table 46: Summary of EBSD investigation for Dales Gorge spherule properties.

Spherule Category	**Descriptions**	**Spherule Number**	**Spherule Size (µm)**	**Crystallinity (%)**	**Alkali Feldspar Crystal Shapes**					**Ilmenite Crystal Habits**				**Other Features**		
					Spherulitic Morphologies			***Non-Spherulitic Morphologies***								
					Fan-like structure	***Bowtie***	***Fascicular***	***Prismatic Laths***	***Equant-Tabular***	***Array***	***Vesicle Lining***	***Exterior Lining***	***Disseminate***	***Dust Rim***	***Botyoidal Rim***	***Vesicle(s)***
Radial	Precipitates fan-like alkali feldspar featuring internal nucleation towards spherule centreücore, radiating from spherule edge	DGTS_S1	745	31.8	✓	✓					✓	✓		✓		stp
		DGTS_S2	610	45.2	✓	✓				✓						
		DGTS_S5	932	6.2	✓					✓	✓					stp+afs+dol
		DGTS_S9	550	39.9	✓							✓		✓		stp
		DGTS_S11	650	50.5	✓					✓						
		DGTS_S18	510	15.6	✓					✓						stp
		DGTS_S21	700	29.8	✓					✓	✓					stp
		DGTS_S22	360	36.1	✓	✓				✓	✓					dol
		DGTS_S28	243	28.9	✓			✓		✓			✓			
		DGTS_S30	390	63	✓					✓						
		DGTS_S31	776	24.8	✓	✓	✓			✓						
		DGTS_S32	600	18.3	✓							✓				stp
		DGTS_S68	360	16.1	✓							✓	✓			
		DGTS_S70	1070	5.7	✓					✓						stp
Random	Precipitates randomly oriented to weakly aligned alkali feldspar microlites	DGTS_S6	393	41.1				✓		✓						
		DGTS_S8	300	43.8				✓				✓				stp
		DGTS_S24	280	21.8					✓				✓			
		DGTS_S27	445	36				✓		✓						
		DGTS_S29	911	17.1				✓	✓	✓	✓					stp
		DGTS_S39	325	63.3				✓		✓						
		DGTS_S40	360	60.7				✓		✓						
		DGTS_S43	430	19.9					✓			✓	✓	✓		stp
		DGTS_S46	300	27	✓			✓		✓						
		DGTS_S49	368	31.3				✓	✓	✓						
		DGTS_S72	320	27.5					✓	✓			✓			

Table 55: EBSD analytical conditions for Bee Gorge spherules based on spherule

Spherule Number	Spherule Diameter (µm)	Step Size Resolution (nm)	Exposure Time (ms)	Aquisition Time (hours)
BGSL-3_S4	322	150	10	16.1
BGSL-3_S3	360	150	10	17.6
BGSL-3_S16	370	120	10	51.1
BGTS_S40	376	150	10	20.4
BGSL-3_S13	377	100	10	53
BGTS_S18	435	140	10	27.5
BGSL-3_S17	437	130	10	44.3
BGSL-3_S2	440	230	10	16.9
BGSL-3_S12	460	200	9	15
BGSL-3_S15	470	200	9	14.3
BGTS_S20	523	150	10	39
BGTS_S29	564	200	10	24
BGTS_S1	653	230	10	23.5
BGTS_S73	676	190	10	40
BGSL-3_S14	770	210	10	47.2
BGTS_S68	866	230	10	39.3
BGTS_S46	995	250	10	45
BGSL-3_S1 (rim-region of interest)	not applicable	250	10	2.4

Table 64: List of categories for Bee Gorge and Paraburdoo spherule textures in Wittenoom Formation proposed by Scally and Simonson (2005).

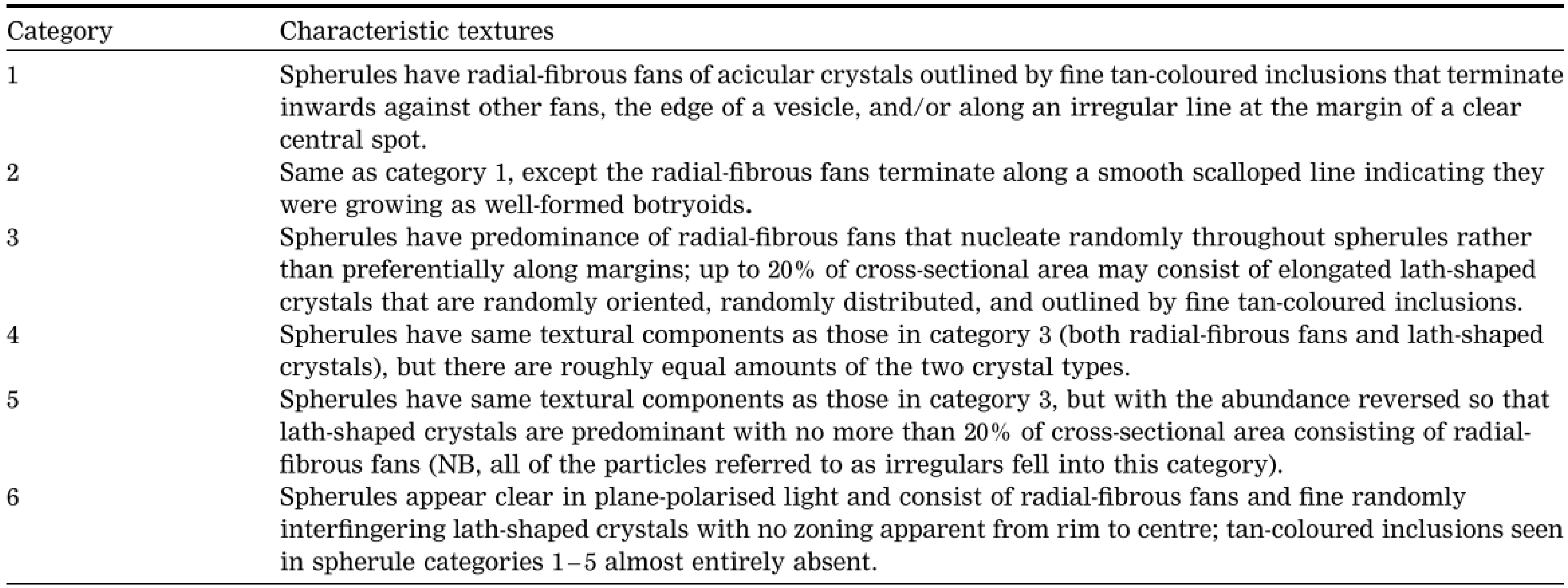

Category	Characteristic textures
1	Spherules have radial-fibrous fans of acicular crystals outlined by fine tan-coloured inclusions that terminate inwards against other fans, the edge of a vesicle, and/or along an irregular line at the margin of a clear central spot.
2	Same as category 1, except the radial-fibrous fans terminate along a smooth scalloped line indicating they were growing as well-formed botryoids.
3	Spherules have predominance of radial-fibrous fans that nucleate randomly throughout spherules rather than preferentially along margins; up to 20% of cross-sectional area may consist of elongated lath-shaped crystals that are randomly oriented, randomly distributed, and outlined by fine tan-coloured inclusions.
4	Spherules have same textural components as those in category 3 (both radial-fibrous fans and lath-shaped crystals), but there are roughly equal amounts of the two crystal types.
5	Spherules have same textural components as those in category 3, but with the abundance reversed so that lath-shaped crystals are predominant with no more than 20% of cross-sectional area consisting of radial-fibrous fans (NB, all of the particles referred to as irregulars fell into this category).
6	Spherules appear clear in plane-polarised light and consist of radial-fibrous fans and fine randomly interfingering lath-shaped crystals with no zoning apparent from rim to centre; tan-coloured inclusions seen in spherule categories 1 – 5 almost entirely absent.

Table 73: Summary of Bee Gorge spherules categorisation based on transmitted light observation, with existing Sweeney and Simonson (2008) and Krull-Davatzes et al. (2015) classification schemes.

Spherule Category	***Descriptions***	**Characteristics**								
		Alkali Feldspar Crystal Shapes			**Other Interior Features**				**Botryoidal Rim**	**Merged Spherules**
		Fibrous-Acicular (Fans)	***Prismatic Laths (Non-Fan)***	***Equant-Tabular (Non-Fan)***	**Quench Texture/ Spherulitic Growth**	**Polygonal Structure**	**Vesicle Shapes**			
							Oval-Rounded-Perfect Circular	***Concave***		
Radial n=(22/80)	Spherules with alkali feldspar fans, radiating inwards from spherule boundaries	22	5	-	8	1	12	1	-	4
Glass core n=(38/80)	Spherule interior with partial to un-crystalline core; alkali feldspar can perform random-radial textures internally	38	2	-	11	11	13	8	23	2
Random n=(12/80)	Spherules preserved alkali feldspar laths with random orientations	-	12	11	-	1	6	-	-	1
Miscellaneous n=(8/80)	Unable to be classified into any of the other categories	-	-	-	-	-	-	-	-	-

Table 82: Summary of Bee Gorge spherule composition with crystallinity in percentage.

Spherule Category	**Description**	**Spherule Number**	**Spherule Diameter (µm)**	**Zero Solution (%)**	**Orthoclase (%)**	**Dolomite (%)**	**Quartz (%)**	**Apatite (%)**	**Rutile (%)**	**Ilmenite (%)**	**Approximate Total Crystalinity (%)**
Radial (n=12)	Precipitates fan-like alkali feldspar featuring internal nucleation towards spherule centre/core, radiating from spherule edge	BGSL-3_S1 (ROI)	Not applicable	16.2	80.6	0.1	0.1	0	0	0	80.8
		BGSL-3_S4	322	97.5	1.3	1.1	0.1	0	0	0	2.5
		BGSL-3_S12	460	89.9	5.8	3.8	0.4	0	0	0	10
		BGSL-3_S15	470	84.6	14.9	0.3	0.1	0	0.1	0	15.4
		BGSL-3_S16	370	42.5	56.2	0.3	0.7	0.2	0.2	0	57.6
		BGSL-3_S17	437	64.5	34.1	0.4	0.5	0.4	0.1	0	35.5
		BGTS_S1	653	92.8	5.9	1	0.2	0.1	0	0	7.2
		BGTS_S18	435	88.6	9.5	1.6	0.1	0.1	0.1	0	11.4
		BGTS_S20	523	80.1	19.2	0.3	0.2	0.1	0.1	0	19.9
		BGTS_S29	564	97.1	1.1	1.7	0.1	0.1	0	0	3
		BGTS_S68	866	66.8	30.8	1.2	0.8	0.3	0.2	0	33.3
		BGTS_S73	676	63	33.5	2.4	0.6	0.3	0.2	0	37
Random (n=6)	Precipitates randomly oriented to weakly aligned alkali feldspar microlites	BGSL-3_S2	440	47.8	51.6	0.3	0.3	0	0	0	52.2
		BGSL-3_S3	360	47.6	51.5	0.4	0.4	0	0	0.1	52.4
		BGSL-3_S13	377	59.3	37.9	0.3	2.1	0.2	0.1	0	40.6
		BGSL-3_S14	770	53	42.7	1.5	0.8	1.8	0.2	0	47
		BGTS_S40	376	89.4	9.7	0.4	0.2	0.3	0.1	0	10.7
		BGTS_S46	995	85.2	13.9	0.4	0.3	0.1	0	0	14.7

Table 89: Summary of EBSD investigation for Bee Gorge spherule properties.

Characteristics													
					Alkali Feldspar Crystal Shapes						Other Features		
					Spherulitic Morphologies				Non-Spherulitic Morphologies				
Spherule Category	Descriptions	Spherule Number	Spherule Size (µm)	Crystallinity (%)	Fan-like structure	Polygonal structure	Bowtie	Spherical	Prismatic Laths	Equant-Tabular	Devitrification	Botyoidal Rim	Vesicle(s)
Radial	Precipitates fan-like alkali feldspar featuring internal nucleation towards spherule centre/core, radiating from spherule edge	BGSL-3_S1 (ROI)	not applicable	83.8	✓								
		BGSL-3_S4	322	2.5	✓			✓					
		BGSL-3_S12	460	10	✓								qz
		BGSL-3_S15	470	15.4	✓								afs
		BGSL-3_S16	370	57.6	✓		✓	✓					
		BGSL-3_S17	437	35.5	✓		✓						qz+afs
		BGTS_S1	653	7.2	✓								qz+afs
		BGTS_S18	435	11.4	✓	✓							
		BGTS_S20	523	19.9	✓				✓				
		BGTS_S29	564	3	✓						✓		afs
		BGTS_S68	866	33.3	✓								dol
		BGTS_S73	676	37	✓			✓					qz+afs
Random	Precipitates randomly oriented to weakly aligned alkali feldspar microlites	BGSL-3_S2	440	52.2					✓				afs
		BGSL-3_S3	360	52.4					✓	✓			afs
		BGSL-3_S13	377	40.6	✓				✓			✓	
		BGSL-3_S14	770	47				✓	✓				
		BGTS_S40	376	10.7	✓				✓				
		BGTS_S46	995	14.7					✓	✓			

Appendices

Appendix A: Images for Electron Microscopy Analytical Results

Dales Gorge spherule layer

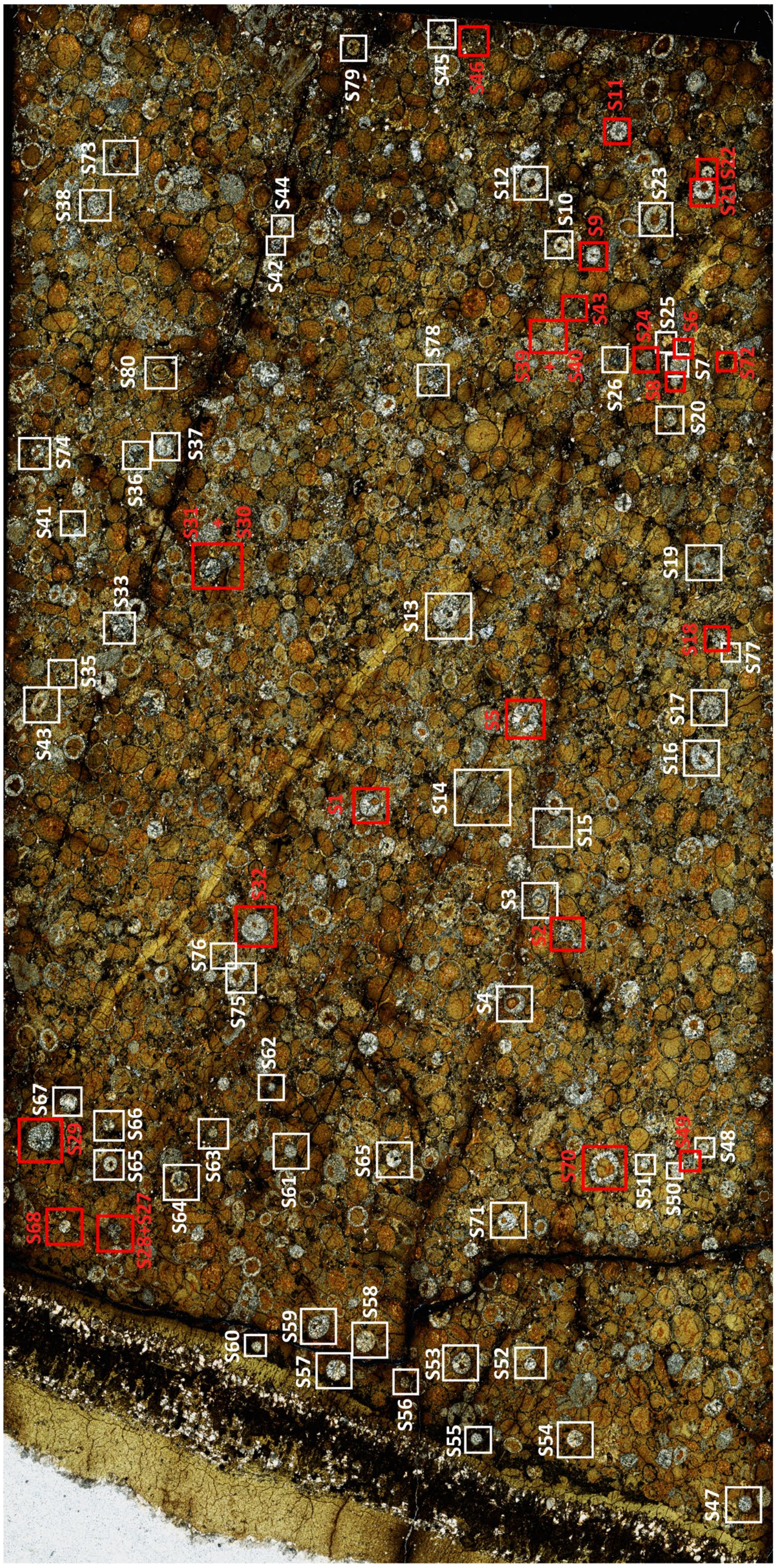

XPL navigation map for thin section 10335093/DGTS for Dales Gorge spherule investigations, red annotations represent EBSD examined spherules (n=25).

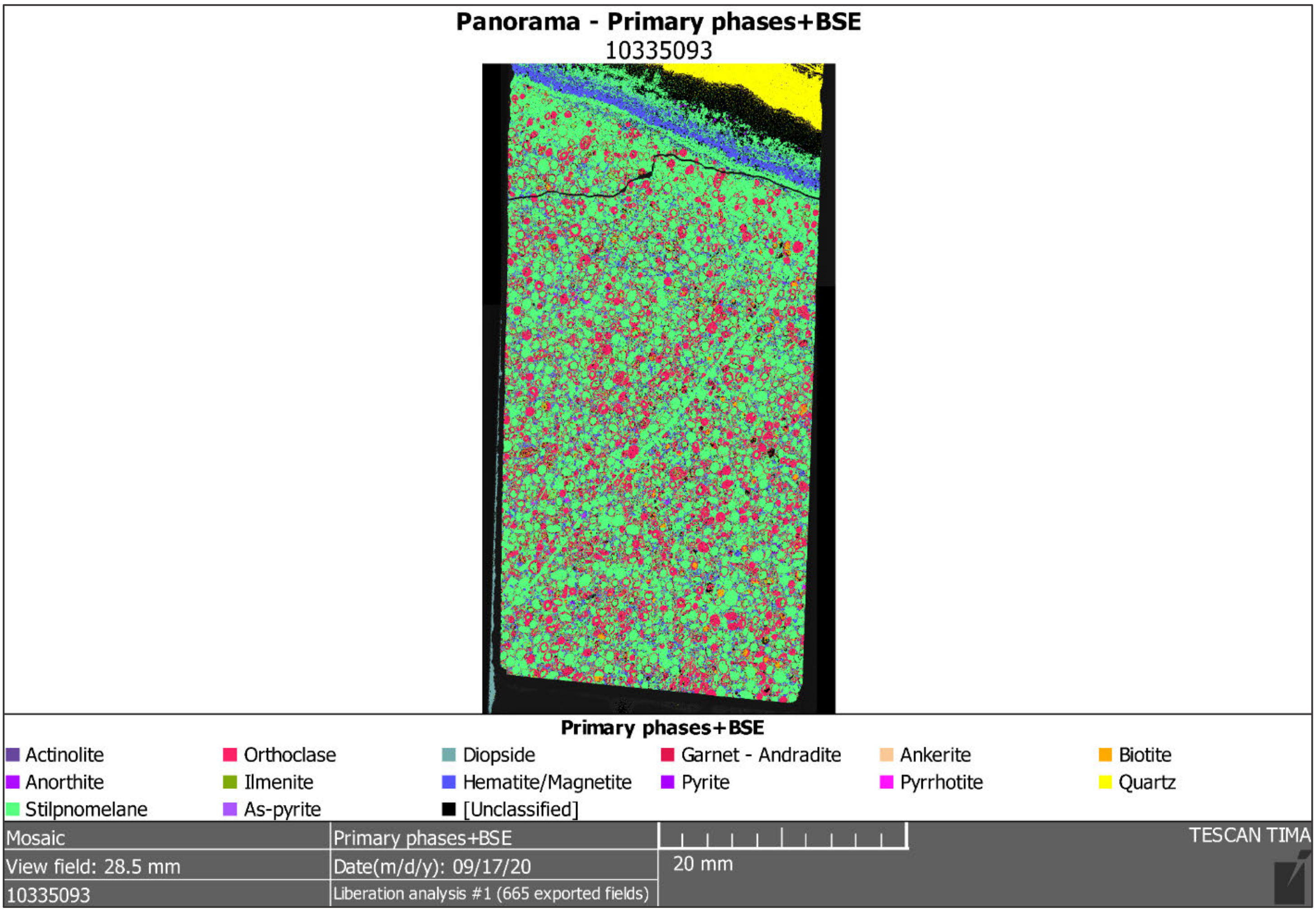

TIMA map for Dales Gorge ejecta horizon (DGTS/thin section 10335093) with well-defined mineral phases.

Appendix A: Images for Electron Microscopy Analytical Results (cont.)

Bee Gorge spherule layer

PPL navigation map for thin section BGSL-1/BGTS for Bee Gorge spherule investigations, red annotations represent EBSD examined spherules (n=18).

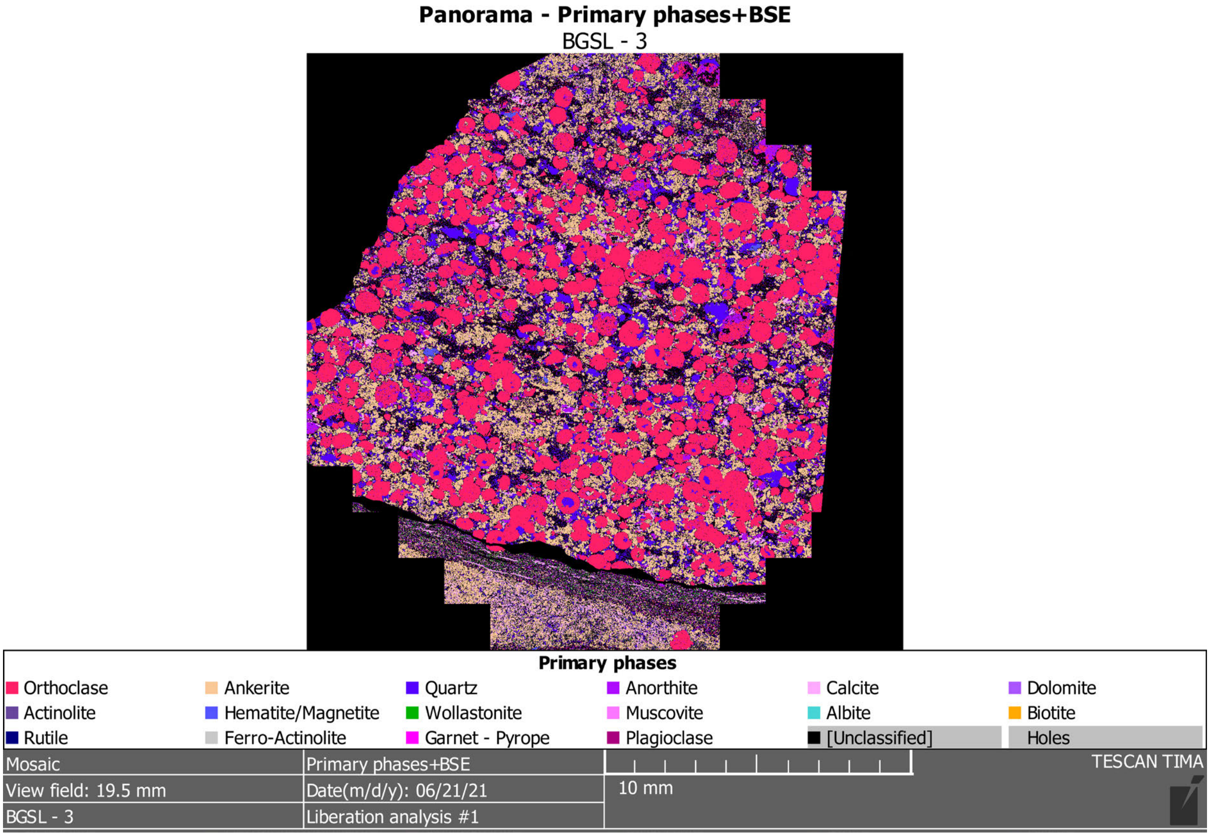

TIMA map for Bee Gorge ejecta horizon, BGSL-3, with well-defined mineral phases.

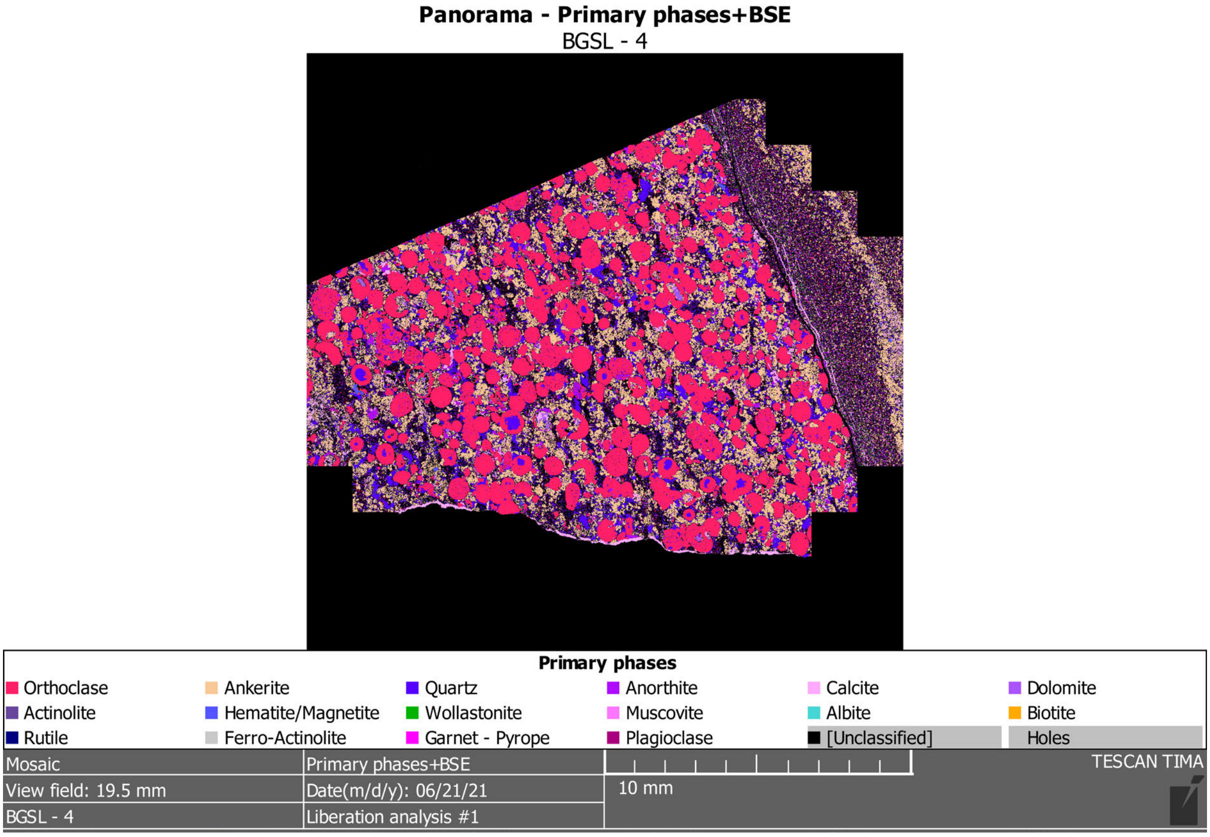

TIMA map for Bee Gorge ejecta horizon, BGSL-4, with well-defined mineral phases.

Appendix B: Tabulation for Electron Microscopy Analytical Records

List of Dales Gorge spherules categorisation in DGTS based on transmitted light observations.

			Characteristics							
			Alkali Feldspar Crystal Shapes			Other Interior Features				
							Vesicle Shapes			
Spherule Category	*Descriptions*	*Spherule Number*	*Fibrous-Acicular (Fans)*	*Prismatic-Laths (Non-Fan)*	*Equant-Tabular (Non-Fan)*	Quench Texture/ Spherulitic Growth	*Oval-Rounded-Perfect Circular*	*Concave*	Botryoidal Rim	Merged Spherules
Radial n=(42/80)	Spherules with alkali feldspar fans, radiating inwards from spherule boundaries	S1, S2, S4, S5, S7, S9, S11, S12, S13, S16, S17, S18, S20, S21, S22, S30, S31, S33, S36, S37, S38, S44, S47, S48, S50, S51, S52, S54, S56, S57, S58, S59, S60, S64, S66, S67, S68, S69, S71, S74, S77, S78	S1, S2, S4, S5, S7, S9, S11, S12, S13, S16, S17, S18, S20, S21, S22, S30, S31, S33, S36, S37, S38, S44, S47, S48, S50, S51, S52, S54, S56, S57, S58, S59, S60, S64, S66, S67, S68, S69, S71, S74, S77, S78	-	-	S1, S13, S17, S30, S31, S37, S38, S47	S1, S4, S5, S13, S18, S21, S22, S70, S73, S74	S9, S12, S16, S71	-	S21-S22
Glass core n=(16/80)	Spherule interior with partial to un-crystalline core; alkali feldspar can perform random-radial textures internally	S3, S10, S23, S28, S32, S34, S41, S53, S63, S65, S70, S73, S75, S76, S79, S80,	S3, S10, S23, S28, S32, S34, S41, S53, S65, S70, S75, S76, S80	-	S63, S73, S79	-	S10, S34, S70, S73	S3, S23	S10, S23, S75	S3, S28, S32
Random n=(19/80)	Spherules preserved alkali feldspar laths with random orientations	S6, S8, S14, S15, S19, S24, S27, S29, S35, S39, S40, S43, S45, S46, S49, S55, S61, S62, S72	-	S6, S8, S27, S29, S39, S40, S45	S14, S15, S19, S24, S27, S29, S35, S43, S46, S49, S55, S61, S62, S72	-	S14, S19, S24, S29, S43	S15, S19	-	S27, S39-S40
Miscellaneous n=(3/80)	Unable to be classified into any of the other categories	S25, S26, S42	-	-	-	-	-	-	-	-

List of Bee Gorge spherules categorisation in BGTS based on transmitted light observations.

Spherule Category	***Descriptions***	***Spherule Number***	**Characteristics**									
			Alkali Feldspar Crystal Shapes			**Other Interior Features**						
								Vesicle Shapes		**Botryoidal Rim**	**Merged Spherules**
			Fibrous-Acicular (Fans)	***Prismatic-Laths (Non-Fan)***	***Equant-Tabular (Non-Fan)***	**Quench Texture/ Spherulitic Growth**	**Polygonal Structure**	***Oval-Rounded-Perfect Circular***	***Concave***		
Radial n=(22/80)	Spherules with alkali feldspar fans, radiating inwards from spherule boundaries	S1, S2, S3, S7, S12, S15, S19, S20, S21, S34, S38, S40, S45, S51, S55, S57, S66, S68, S73, S76, S77, S79	S1, S2, S3, S7, S12, S15, S19, S20, S21, S34, S38, S40, S45, S51, S55, S57, S66, S68, S73, S76, S77, S79	S15, S20, S34, S40, S45	**-**	S2, S7, S12, S19, S21, S34, S57, S73	S34	S1, S15, S21, S38, S45, S51, S57, S68, S73, S76, S77, S79	S21	**-**	S20, S51, S66, S77
Glass core n=(38/80)	Spherule interior with partial to un-crystalline core; alkali feldspar can perform random-radial textures internally	S4, S5, S8, S11, S13, S16, S18, S23, S24, S25, S28, S29, S30, S31, S32, S37, S39, S41, S42, S43, S44, S47, S48, S49, S50, S53, S54, S56, S61, S62, S63, S64, S65, S69, S70, S74, S75, S78	S4, S5, S8, S11, S13, S16, S18, S23, S24, S25, S28, S29, S30, S31, S32, S37, S39, S41, S42, S43, S44, S47, S48, S49, S50, S53, S54, S56, S61, S62, S63, S64, S65, S69, S70, S74, S75, S78	S43, S44	**-**	S23, S32, S37, S43, S47, S49, S50, S56, S61, S62, S74	S5, S18, S28, S29, S41, S48, S49, S50, S56, S63, S64	S4, S23, S25, S28, S29, S42, S43, S47, S49, S53, S54, S56, S74,	S16, S24, S44, S61, S63, S65, S69, S75	S5, S8, S11, S13, S16, S25, S28, S30, S31, S32, S37, S41, S42, S44, S47, S48, S49, S50, S56, S61, S63, S69, S75	S18, S78
Random n=(12/80)	Spherules preserved alkali feldspar laths with random orientations	S6, S10, S14, S17, S46, S52, S58, S59, S60, S67, S71, S72	**-**	S6, S10, S14, S17, S46, S52, S58, S59, S60, S67, S71, S72	S10, S14, S17, S46, S52, S58, S59, S60, S67, S71, S72	**-**	S67	S14, S17, S46, S52, S58, S59	**-**	**-**	S14
Miscellaneous n=(8/80)	Unable to be classified into any of the other categories	S9, S22, S26, S27, S33, S35, S36, S80	**-**	**-**	**-**	**-**	**-**	**-**	**-**	**-**	**-**

Appendix C: Vapor Plume Template